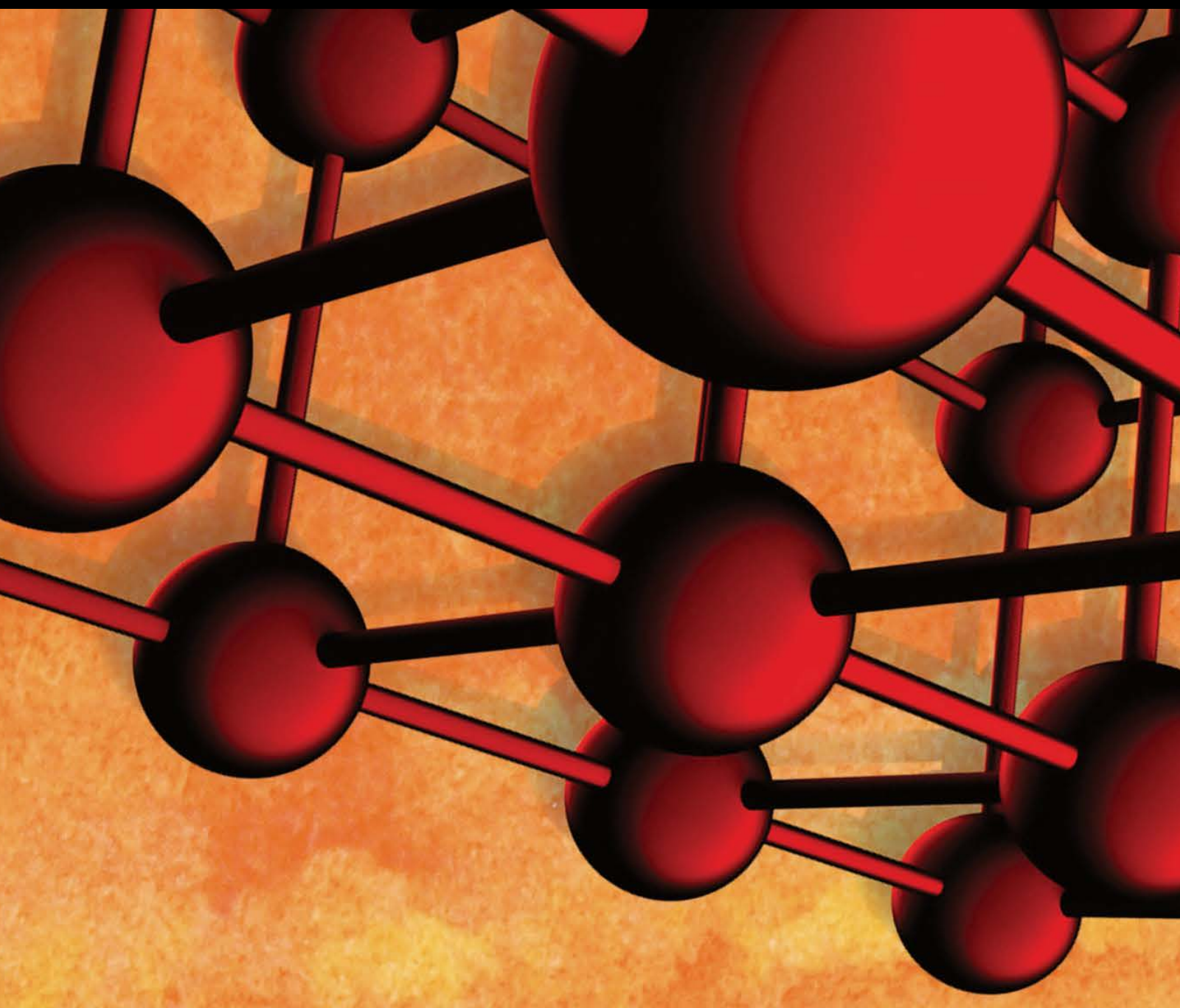


Advances in Materials Science and Engineering

Structural Dynamics and Stability of Composite Structures

Guest Editors: Sung-Cheon Han, Ireneusz Kreja, Guillermo Rus,
and Gilson R. Lomboy





Structural Dynamics and Stability of Composite Structures

Advances in Materials Science and Engineering

Structural Dynamics and Stability of Composite Structures

Guest Editors: Sung-Cheon Han, Ireneusz Kreja,
Guillermo Rus, and Gilson R. Lomboy



Copyright © 2016 Hindawi Publishing Corporation. All rights reserved.

This is a special issue published in “Advances in Materials Science and Engineering.” All articles are open access articles distributed under the Creative Commons Attribution License, which permits unrestricted use, distribution, and reproduction in any medium, provided the original work is properly cited.

Editorial Board

- Michael Aizenshtein, Israel
Jarir Aktaa, Germany
Konstantinos Anthymidis, Greece
Amit Bandyopadhyay, USA
Arun Bansil, USA
Massimiliano Barletta, Italy
Mikhael Bechelany, France
Jozef Bednarcik, Germany
Avi Bendavid, Australia
Jamal Berakdar, Germany
Giovanni Berselli, Italy
Patrice Berthod, France
Didier Blanchard, Denmark
Susmita Bose, USA
Heinz-Günter Brokmeier, Germany
Steve Bull, UK
Peter Chang, Canada
Daolun Chen, Canada
Gianluca Cicala, Italy
Gabriel Cuello, France
Narendra B. Dahotre, USA
João P. Davim, Portugal
Angela De Bonis, Italy
Francesco Delogu, Italy
Seshu B. Desu, USA
Guru P. Dinda, USA
Yong Ding, USA
Nadka Tzankova Dintcheva, Italy
Kaveh Edalati, Japan
Philip Eisenlohr, USA
Paolo Ferro, Italy
Massimo Fresta, Italy
Eric Freysz, France
Sergi Gallejo, Spain
Santiago Garcia-Granda, Spain
Filippo Giannazzo, Italy
Daniel Guay, Canada
Fawzy H. Samuel, Canada
- Hiroki Habazaki, Japan
Joke Hadermann, Belgium
Satoshi Horikoshi, Japan
David Houivet, France
Rui Huang, USA
Michele Iafisco, Italy
Katsuyuki Kida, Japan
Jae-Ho Kim, Republic of Korea
Akihiko Kimura, Japan
Takayuki Kitamura, Japan
Hongchao Kou, China
Prashant Kumta, USA
Luciano Lamberti, Italy
Heinrich Lang, Germany
Pavel Lejcek, Czech Republic
Cristina Leonelli, Italy
Ying Li, USA
Jun Liu, China
Meilin Liu, Georgia
Wei Liu, France
Yunqi Liu, China
Fernando Lusquiños, Spain
Peter Majewski, Australia
Philippe Miele, France
Hossein Moayedi, Iran
Paul Munroe, Australia
Rufino M. Navarro, Spain
Luigi Nicolais, Italy
Hiroschi Noguchi, Japan
Chérif Nouar, France
José L. Ocaña, Spain
Tsutomu Ohzuku, Japan
Olanrewaju Ojo, Canada
Gianfranco Palumbo, Italy
Anna Paradowska, Australia
Matthew Peel, UK
Gianluca Percoco, Italy
Giorgio Pia, Italy
- Jean-Francois Pierson, France
Simon C. Potter, Canada
Manijeh Razeghi, USA
Yuri Ribakov, Israel
Anna Richelli, Italy
Antonio Riveiro, Spain
Pascal Roussel, France
Timo Sajavaara, Finland
Antti Salminen, Finland
Carlo Santulli, Italy
Franz-Josef Schmitt, Germany
Jainagesh A. Sekhar, USA
Fridon Shubitidze, USA
Maria A. Signore, Italy
Donato Sorgente, Italy
Charles C. Sorrell, Australia
Costas M. Soukoulis, USA
Sam-Shajing Sun, USA
Kohji Tashiro, Japan
Somchai Thongtem, Thailand
Achim Trampert, Germany
Filip Tuomisto, Finland
Krystyn Van Vliet, USA
Qiang Wang, China
Rong Wang, USA
Rui Wang, China
Lu Wei, China
Jörg M. K. Wieszorek, USA
Wei Wu, USA
Hemmige S. Yathirajan, India
Wenbin Yi, China
Belal F. Yousif, Australia
Jinghuai Zhang, China
Li Zhang, China
Ming-Xing Zhang, Australia
Wei Zhou, China

Contents

Structural Dynamics and Stability of Composite Structures

Sung-Cheon Han, Ireneusz Kreja, Guillermo Rus, and Gilson R. Lomboy
Volume 2016, Article ID 7468181, 2 pages

Safety Evaluation of a Hybrid Substructure for Offshore Wind Turbine

Min-Su Park, Youn-Ju Jeong, Young-Jun You, and Yoon-Koog Hwang
Volume 2016, Article ID 8089426, 14 pages

Relationships between Imperfections and Shear Buckling Resistance in Web Plate with Sectional Damage Caused by Corrosion

Jin-Hee Ahn, Shigenobu Kainuma, Won-Hong Lee, Youn-Ju Jeong, and In-Tae Kim
Volume 2016, Article ID 6467589, 12 pages

Experimental and Analytical Investigation Based on 1/2 Scale Model for a Cleanroom Unit Module Consisting of Steel Section and Reinforced Concrete

Sijun Kim and Se Woon Choi
Volume 2016, Article ID 6920725, 11 pages

Structural Stability and Dynamics of FGM Plates Using an Improved 8-ANS Finite Element

Weon-Tae Park
Volume 2016, Article ID 2821473, 9 pages

Analysis of Dynamic Fracture Parameters in Functionally Graded Material Plates with Cracks by Graded Finite Element Method and Virtual Crack Closure Technique

Li Ming Zhou, Guang Wei Meng, Xiao Lin Li, and Feng Li
Volume 2016, Article ID 8085107, 14 pages

Editorial

Structural Dynamics and Stability of Composite Structures

Sung-Cheon Han,¹ Ireneusz Kreja,² Guillermo Rus,³ and Gilson R. Lomboy⁴

¹Department of Civil & Railroad Engineering, Daewon University College, Jecheon, Republic of Korea

²Faculty of Civil and Environmental Engineering, Gdańsk University of Technology, 80-952 Gdańsk, Poland

³Department of Structural Mechanics, University of Granada, Granada, Spain

⁴Civil, Construction & Environmental Engineering, Iowa State University, Ames, IA 50011, USA

Correspondence should be addressed to Sung-Cheon Han; hasc1203@daum.net

Received 3 August 2016; Accepted 3 August 2016

Copyright © 2016 Sung-Cheon Han et al. This is an open access article distributed under the Creative Commons Attribution License, which permits unrestricted use, distribution, and reproduction in any medium, provided the original work is properly cited.

In structural applications, past few decades have seen outstanding advances in the use of composite materials including Functionally Graded Materials (FGM). Most structures, whether they are used in civil, marine, or aerospace engineering, are subjected to dynamic loads during their operation. Therefore, Dynamic and Stability Analysis is receiving much attention in academia and industries. Recent advances in Dynamic and Stability Analysis have led to the development of macro-, micro-, and nanolaminated composites and FGM plates.

In M.-S. Park et al.'s paper, the authors investigated the safety evaluation of a hybrid substructure for offshore wind turbine. Towers and rotor-nacelles are being enlarged to respond to the need for higher gross generation of the wind turbines. However, the accompanying enlargement of the substructure supporting these larger offshore wind turbines makes it strongly influenced by the effect of wave forces. In the present study, the hybrid substructure is suggested to reduce the wave forces by composing a multicylinder having different radii near free surface and a gravity substructure at the bottom of the multicylinder. In addition, the reaction forces acting on the substructure due to the very large dead load of the offshore wind turbine require very firm foundations. This implies that the dynamic pile-soil interaction has to be fully considered. Therefore, ENSOFT Group V7.0 is used to calculate the stiffness matrices on the pile-soil interaction conditions. These matrices are then used together with the loads at TP (Transition Piece) obtained from GH-Bladed for the structural analysis of the hybrid substructure by ANSYS ASAS. The structural strength and deformation are

evaluated to derive an ultimate structural safety of the hybrid substructure for various soil conditions and show that the first few natural frequencies of the substructure are heavily influenced by the wind turbine. The modal analysis is carried out through GH-Bladed to examine the resonance between the wind turbine and the hybrid substructure.

The relationship between imperfections and shear buckling resistance of web plates with sectional damage caused by corrosion is studied. To examine the imperfection effect on the shear buckling resistance of a web plate with sectional damage, a series of a nonlinear finite element (FE) analyses were carried out for a web plate with sectional damage, which was assumed as local corrosion damage. For considering imperfections of the web plate in the girder, initial out-of-plane deformation was introduced in the FE analysis model. Using the FE analysis results, the changes in the shear buckling resistance of the web plate with sectional damage were quantitatively examined and summarized according to the aspect ratio, boundary conditions, and height of the damaged section of the web plate. The effects of web imperfections on the shear buckling resistance were evaluated to be little compared to that of the web plate without sectional damage. The shear buckling resistances were shown to significantly change in the high-aspect-ratio web plate. A simple evaluation equation for the shear buckling resistance of a web plate with sectional damage was modified for use in the practical maintenance of a web plate in corrosive environments.

The rapid advances in high tech industries and the increased demand for high precision and reliability of their production environments call for larger structures and higher

vertical vibration performance for high technology facilities. Therefore, there is an urgent demand for structural design and vertical vibration evaluation technologies for high tech facility structures. For estimating the microvibration performance for a clean room unit module in high technology facilities, this study performs the scale modeling experiment and analytical validation. First, the 1/2 scale model (width 7500 mm, depth 7500 mm, and height 7250 mm) for a clean room unit module is manufactured based on a mass-based similitude law which does not require additional mass. The dynamic test using an impact hammer is conducted to obtain the transfer function of 1/2 scale model. The transfer function derived from the test is compared with the analytical results to calibrate the analytical model. It is found that, unlike static analyses, the stiffness of embedded reinforcement must be considered for estimating microvibration responses. The similitude law used in this study is validated by comparing the full-scale analytical model and 1/2 scale analytical model for a clean room unit module.

In the present work, the vibration and buckling analysis of Functionally Graded Material (FGM) structures, using a modified 8-node shell element that allows for the effects of transverse shear deformation, was improved. The properties of FGM vary continuously through the thickness direction according to the volume fraction of constituents defined by sigmoid function. The finite element is improved by the combined use of different sets of collocation points for interpolation of the strain components and assumed natural strains. The modified 8-ANS shell element has been employed to study the effect of power law index on dynamic analysis of FGM plates with various boundary conditions and buckling analysis under combined compressive, tensile, and shear loads and interaction curves of FGM plates subjected to combined loading is carried out. To overcome shear and membrane locking problems, the assumed natural strain method is employed. In order to validate and compare the finite element numerical solutions, the reference results of plates based on Navier's method and the series solutions of sigmoid FGM (S-FGM) plates are compared. Results of the present study show good agreement with the reference results. The solutions of vibration and buckling analysis are numerically illustrated in a number of tables and figures to show the influence of power law index, side-to-thickness ratio, aspect ratio, types of loads, and boundary conditions in FGM structures.

Based on the finite element software ABAQUS and graded element method, we developed a dummy node fracture element, wrote the user subroutines UMAT and UEL, and solved the energy release rate component of Functionally Graded Material (FGM) plates with cracks. An interface element tailored for the virtual crack closure technique (VCCT) was applied. Fixed cracks and moving cracks under dynamic loads were simulated. The results were compared to other VCCT-based analyses. With the implementation of a crack speed function within the element, it can be easily expanded to the cases of varying crack velocities, without convergence difficulty for all cases. Neither singular element nor collapsed element was required. Therefore, due to its simplicity, the VCCT interface element is a potential tool for engineers

to conduct dynamic fracture analysis in conjunction with commercial finite element analysis codes.

These papers represent an exciting, insightful observation into the state of the art as well as emerging future topics, in this important interdisciplinary field. We hope that this special issue would attract a major attention of the peers.

Acknowledgments

We would like to express our appreciation to all the authors, reviewers, and the Editorial Board members for the great support to make this special issue possible.

*Sung-Cheon Han
Ireneusz Kreja
Guillermo Rus
Gilson R. Lomboy*

Research Article

Safety Evaluation of a Hybrid Substructure for Offshore Wind Turbine

Min-Su Park, Youn-Ju Jeong, Young-Jun You, and Yoon-Koog Hwang

Structural Engineering Research Institute, Korea Institute of Civil Engineering and Building Technology, 283 Goyangdae-ro, Ilsanseo-gu, Goyang-si, Gyeonggi-do 10223, Republic of Korea

Correspondence should be addressed to Min-Su Park; mspark@kict.re.kr

Received 18 May 2016; Accepted 26 July 2016

Academic Editor: Sung-Cheon Han

Copyright © 2016 Min-Su Park et al. This is an open access article distributed under the Creative Commons Attribution License, which permits unrestricted use, distribution, and reproduction in any medium, provided the original work is properly cited.

Towers and rotor-nacelles are being enlarged to respond to the need for higher gross generation of the wind turbines. However, the accompanying enlargement of the substructure supporting these larger offshore wind turbines makes it strongly influenced by the effect of wave forces. In the present study, the hybrid substructure is suggested to reduce the wave forces by composing a multicylinder having different radii near free surface and a gravity substructure at the bottom of the multicylinder. In addition, the reaction forces acting on the substructure due to the very large dead load of the offshore wind turbine require very firm foundations. This implies that the dynamic pile-soil interaction has to be fully considered. Therefore, ENSOFT Group V7.0 is used to calculate the stiffness matrices on the pile-soil interaction conditions. These matrices are then used together with the loads at TP (Transition Piece) obtained from GH-Bladed for the structural analysis of the hybrid substructure by ANSYS ASAS. The structural strength and deformation are evaluated to derive an ultimate structural safety of the hybrid substructure for various soil conditions and show that the first few natural frequencies of the substructure are heavily influenced by the wind turbine. Therefore, modal analysis is carried out through GH-Bladed to examine the resonance between the wind turbine and the hybrid substructure.

1. Introduction

Offshore wind energy has gained attention in many countries as an alternative and reliable energy source since its potential has been recognized for long and mostly associated to the concept of nondestructive renewable energy. Therefore, many offshore wind farms are in the planning phase like in Europe, where wind farms will be established at greater water depths with larger turbines. In addition, towers and rotor-nacelles are being enlarged to respond to the need for higher gross generation of wind turbines. However, the accompanying enlargement of the substructure supporting these larger offshore wind turbines makes it strongly influenced by the effect of wave forces, which requires adopting new concepts for the substructure. Various substructures are available for the offshore wind turbines, such as the monopole, gravity-based structure, tripod, suction bucket, jacket, and floating platform. The type of substructure for the offshore wind turbine mainly depends on the water depth, turbine size, and soil conditions and has been studied by many researchers [1–6].

So far, less than twenty tripods have been installed in Europe. Thirty jacket foundations will also be installed at the Ormonde wind farms. Zaaier [7] analyzed different substructures for a 6 MW wind turbine in 20 m water depth. Føreland et al. [8] designed mono-pile, gravity-based structure, jacket, and three-pile fixed support structures for 2.5, 5, and 10 MW wind turbines for different water depths to quantify the economic differences provided by different wind turbine foundation systems for the environmental conditions of the North Sea.

The southwestern coast of the Korean peninsula is one of the most suitable places for the construction of offshore wind turbines. However, it is difficult to determine a proper substructure type because of the water depth range between 20 and 30 m and the very soft clay layer constituting the seabed in this area. This implies that a new substructure type suitable for the environmental characteristics of the southwestern coast of Korea must be developed.

In the present study, the hybrid substructure is suggested for the offshore wind turbines to be installed in

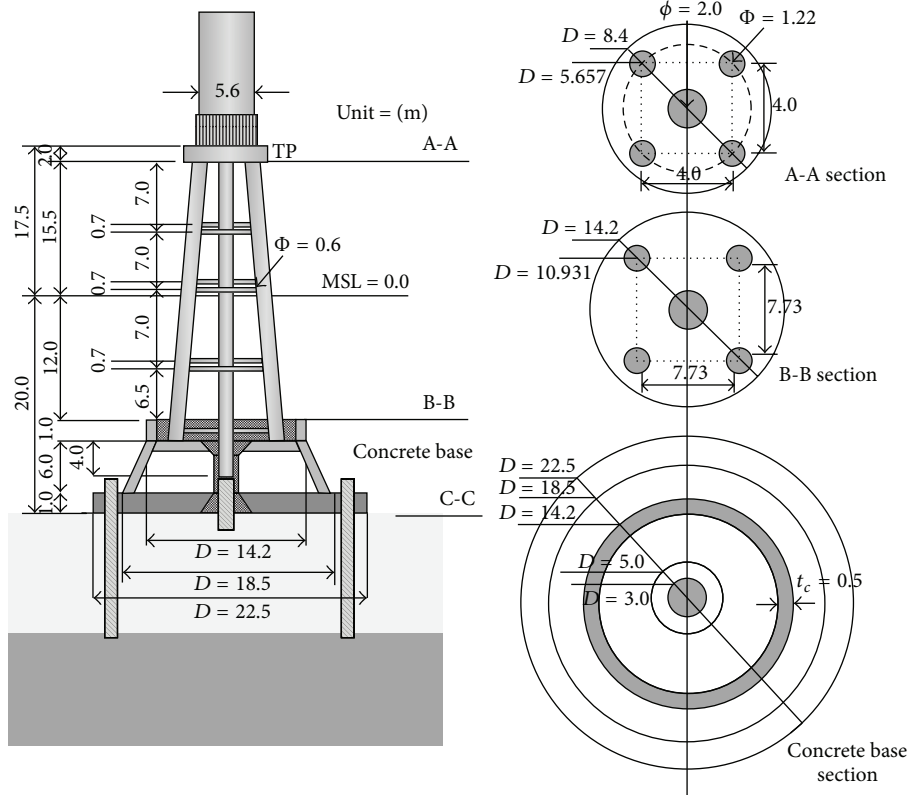


FIGURE 1: Geometrical configuration of the hybrid substructure.

the Korean southwest offshore wind project by composing a multicylinder having different radii near free surface and a gravity substructure at the bottom of the multicylinder [9]. In addition, the reaction forces acting on the substructure due to the very large dead load of the offshore wind turbine require very firm foundations. Therefore, the pile-soil interaction model should be adequately chosen according to the analysis type by performing sensitivity analysis. Some guidelines such as DNV, API, and GL recommend the use of the full nonlinear model for extreme load cases and foundation design. In this study, the ENSOFT Group V7.0 is used to calculate the stiffness matrices for the pile-soil interaction conditions and these matrices are then used together with the loads at TP (Transition Piece) obtained from GH-Bladed for the structural analysis of the hybrid substructure by ANSYS ASAS. The structural strength and deformation are evaluated to derive an ultimate structural safety of the hybrid substructure for various soil conditions and show that the first few natural frequencies of substructure are heavily influenced by the wind turbine. Therefore, the first natural frequency of the substructure must be within the soft-stiff range in between the rotor frequency (1P) and the blade passing frequency (3P). Therefore, modal analysis is carried out through GH-Bladed to investigate the resonance between the wind turbine and the hybrid substructure. It is found that the suggested hybrid substructure can be effective for reducing the hydrodynamic effects and construction costs in the southwestern sea of South Korea.

TABLE 1: Details of 3.0 MW wind turbine model.

Turbine parameters	Unit	Value
Rated power	MW	3.0
Configuration	—	3 blades
Design wind class	—	IEC IA
Rotor diameter	m	91.3
Hub height	m	80
Cut-in speed	m/s	3
Cut-out speed	m/s	25
Rated wind speed	m/s	13
Rated rotor speed	rpm	15.7

2. Numerical Model and Environmental Conditions

2.1. Wind Turbine and Substructure Model. In the present study, the 3.0 MW wind turbine model of Doosan Heavy Industries is selected for the structural safety analysis of the hybrid substructure. The details of this wind turbine are provided in Table 1.

The height of the hybrid substructure is 37.5 m from seabed and the water depth (MSL) is 20.0 m as shown in Figure 1. Since the water particle velocity is the largest near free surface, the hybrid substructure is composed of a multicylinder having different radii near free surface to reduce the wave forces acting on the substructure and a gravity-based

TABLE 2: Dimensions of multicylinder (mm).

Multicylinder	Cylinder part		Joint part	
	Diameter	Thickness	Diameter	Thickness
Side cylinder	1220	30	1224	32
Center cylinder	2000	25	2024	37
Brace	600	20	624	32

TABLE 3: Properties of materials.

	Steel	Concrete
Density (kg/m ³)	7850	2500
Young's modulus (N/m ²)	2.0×10^{11}	3.0×10^{10}
Shear modulus (N/m ²)	7.692×10^{10}	1.271×10^{10}

substructure at the bottom of the multicylinder to increase the stability against overturning moment. The multicylinder and the gravity-based substructure are, respectively, made of steel and concrete with 0.5 m thickness. The main dimensions and characteristics of the hybrid substructure are listed in Tables 2 and 3.

2.2. Design Load Cases and Environmental Conditions. The structural safety analysis adopts design code IEC 61400-3 [10] and is carried out according to the ultimate design load cases (DLC) presented in Table 4.

The wind and wave for the southwestern sea of South Korea are presented in Table 5. In Table 5, FLS stands for fatigue limit state and ULS for ultimate limit state. The data at the selected site measured from July, 1979, to December, 2010, are used to estimate the extreme wind and wave conditions with return period of 50 years according to IEC61400-1 design standard. The extreme current velocities at free surface and seabed are 1.05 m/s and 0.54 m/s, respectively.

2.3. Stiffness for Pile-Soil Interaction. The interaction between the superstructure and foundation system intensifies with larger mass of the substructure. This indicates that this interaction contributes increasingly to the structural response of the total system increases. Based on the soil condition at the selected site, the stiffness matrices for the pile-soil interaction conditions are calculated using ENSOFT Group V7.0. The corresponding stiffness for the pile-soil interaction foundation system is provided in Tables 7–10.

3. Numerical Results and Discussion

3.1. Natural Frequencies and Resonance. For a modern wind turbine, the design criterion for the natural vibration characteristics of the offshore wind turbine is the so-called soft-stiff design. In this case, the lowest natural frequencies of the complete system fore-aft or side-to-side are adjusted so that they remain above the rotational frequency (1P) and below the blade passing frequency (3P) for the entire operating range of the turbine [11]. In order to evaluate the resonance between the wind turbine and the hybrid substructure,

modal analysis is carried out through GH-Bladed for pile-soil interaction and fixed foundation system.

Table 11 and Figure 2 arrange, respectively, the natural frequencies and the mode shapes of the hybrid substructures considering pile-soil interaction and fixed foundation. The difference in the first mode frequency between pile-soil interaction and fixed condition is about 4.3%. Since the coupled stiffness between forces and moments is not considered in this study, the difference becomes larger for higher modes. In addition, the dynamic responses of the hybrid substructure are slightly influenced by this effect. Figure 3 plots the natural frequency of the hybrid substructure system obtained from modal analysis with respect to the spectrum density of the turbine and the wave condition. It is found that the natural frequency of the hybrid substructure system stands between the turbine's natural frequency (1P) and the blade's passing frequency (3P). Accordingly, there is no possibility of resonance to occur between the wind turbine and the hybrid substructure.

3.2. Wave Force Evaluation. Figures 4 and 5 compare, respectively, the wave forces and the wave moments of the hybrid substructure and the mono-pile for various water depths. The properties of the mono-pile are based on Espinosa's model [12] and its diameter is 6 m. The water depths corresponding to the lowest still water level (LSWL), mean sea level (MSL), and highest still water level (HSWL) are 15.44 m, 20.00 m, and 24.56 m, respectively. In the comparison, the calculated total wave forces are divided by the incident wave amplitude ($H/2$) and the wave moments are calculated at seabed. Since the wave force is closely related to the wetted surface of the substructure and the largest water particle velocity occurs near free surface, the wave forces and moments on the mono-pile increase gradually with larger water depth. The largest wave forces on the hybrid substructure are observed at LSWL because the gravity-based substructure is located at seabed. However, the wave forces on the hybrid substructure decrease gradually with larger water depth due to the reduction of the wave forces acting on the gravity-based substructure with increasing water depth. This indicates that installing the multicylinder near free surface can be effective for decreasing the wave forces. The peak wave forces at MSL and HSWL decrease by about 19% and 32% compared to the peak value at LSWL. Moreover, the suggested hybrid substructure appears to be very effective for increasing the stability against overturning moment since the hybrid substructure experiences extremely small variation compared to the large variation encountered by the mono-pile.

3.3. Structural Results. The dynamic responses of the offshore wind turbine supported by the hybrid substructure are investigated for various design load cases (DLC) based on IEC 61400-3 [10] design code. The loads at TP (Transition Piece) obtained from GH-Bladed are presented in Table 12. In the present study, the values at TP for DLC 6.2ja-2 (idling with grid loss condition) are used because they are the largest among all the DLC. Figures 6 and 7 show the time histories of the forces and the moments at TP.

TABLE 4: Design load cases (DLC) for ultimate limit state.

DLC	Condition	Wave	Wind
1.1	Power production	Normal	Normal
1.3	Power production	Normal	Extreme
1.4	Power production	Normal	Extreme
1.5	Power production	Normal	Extreme
1.6a	Power production	Severe	Normal
2.1	Power production + control system fault	Normal	Normal
2.2	Power production + occurrence of fault	Normal	Normal
2.3	Power production + loss of electrical grid connection	Normal	Extreme
4.2	Normal shut-down + deterministic gust	Normal	Extreme
5.1	Emergency shut-down	Normal	Normal
6.1a	Idling	Extreme	Extreme
6.2a	Idling with grid loss	Extreme	Extreme
6.3a	Idling with extreme yaw misalignment	Extreme	Extreme
7.1a	Idling with pitch failure	Extreme	Extreme
8.1	Transport, assembly, maintenance, and repair	Normal	15 m/s

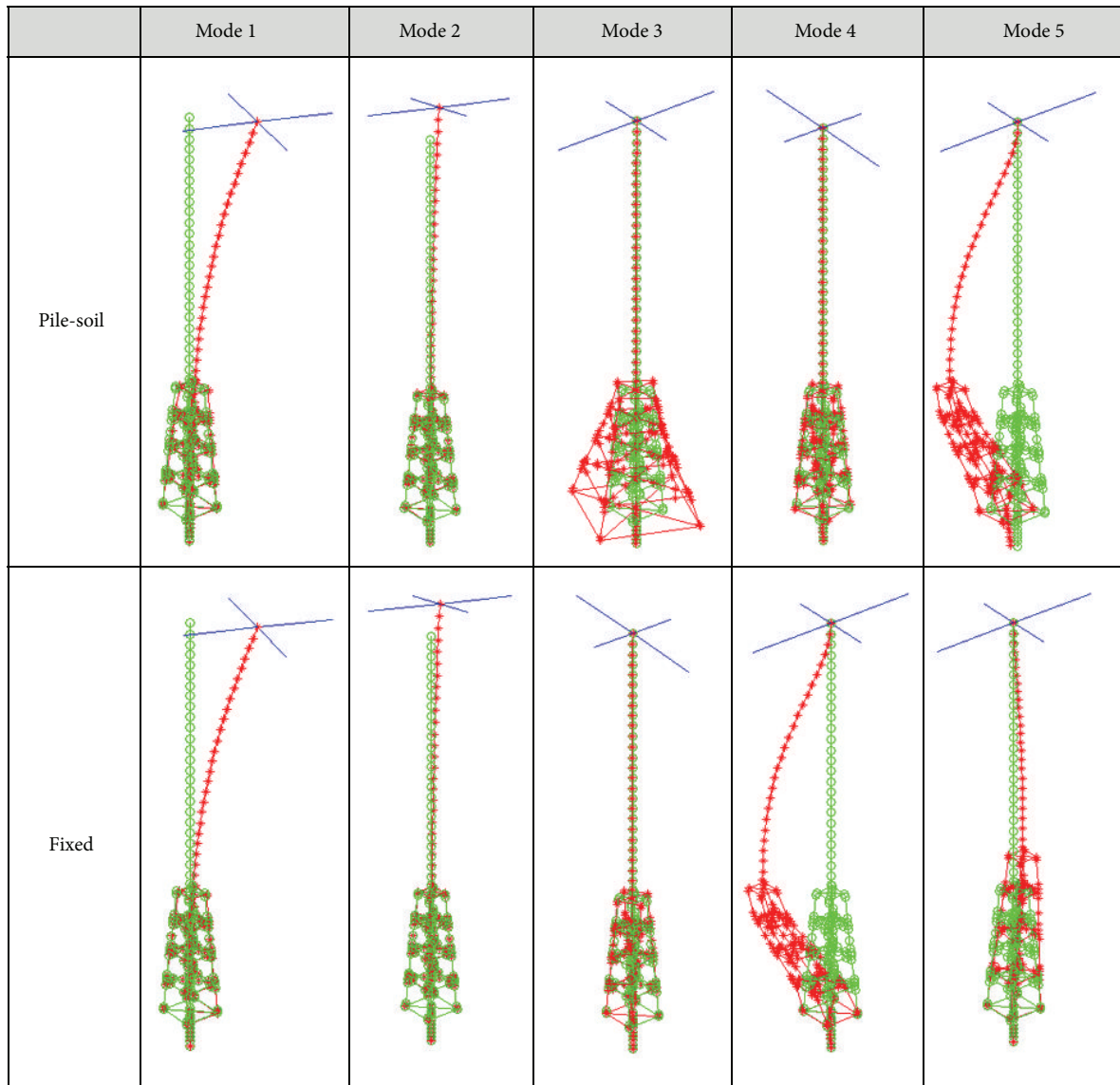


FIGURE 2: Comparison of mode shapes of hybrid substructure.

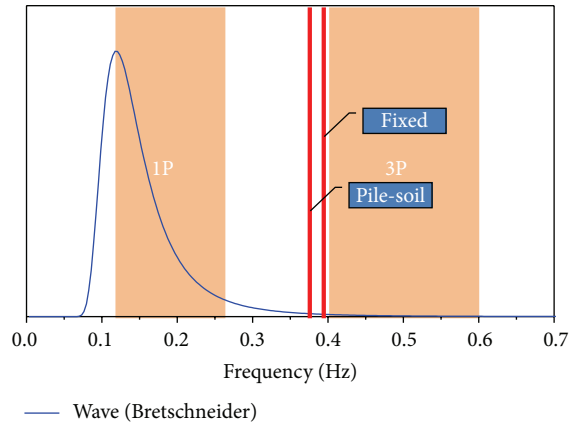


FIGURE 3: Comparison of hybrid substructure on the spectrum density of wind turbine and wave.

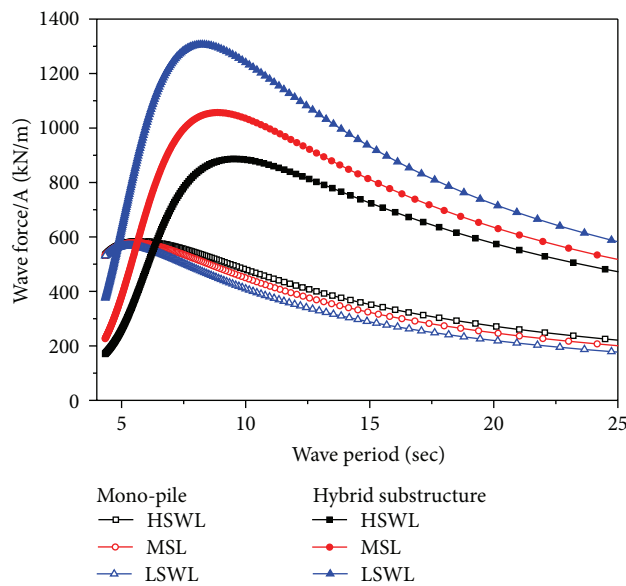


FIGURE 4: Comparison of wave forces for various water depths.

TABLE 5: Environmental conditions.

	Wind	Wave	Limit state
Normal	6.90 m/s	$H_s = 1.48$ m, $T_p = 6.25$ sec	FLS
Extreme	42.99 m/s	$H_s = 6.87$ m, $T_p = 13.70$ sec	ULS
Extreme design	42.99 m/s	$H_d = 12.78$ m, $T_p = 13.70$ sec	ULS

Using the wind loads at TP and the stiffness matrices for pile-soil foundation system, the structural analysis of the hybrid substructure is carried out for various water depths using ANSYS ASAS. The 9th-order stream function wave theory is adopted to model the design wave that is regular wave with $H = 12.78$ m and $T = 13.76$ sec. The structural results are summarized in Table 13. A safety factor of 1.35 is applied for all cases. The displacements with pile-soil

condition are larger than those with fixed condition but the results exhibit very different patterns. The displacement and the bending moment at MSL are largest in all cases since the middle brace is strongly influenced by the wave forces. The combined stress is concentrated at the connecting part between the multicylinder and the concrete cone and shows also large variation. Therefore, this connecting part should be examined explicitly in order to achieve reliable design of the substructure. The structural displacement and the bending moment at MSL are plotted in Figures 8–11 for various soil conditions. Since the loads at TP are larger than the wave forces acting on the substructure, the time histories of the displacement and bending moment do not present regular pattern, which means that the substructure is mainly influenced by the wind forces acting on the offshore wind turbine.

The JONSWAP wave spectrum is used to model irregular wave condition with $H = 6.87$ m and $T = 13.70$ sec. The JONSWAP wave spectrum was developed during the Joint

TABLE 6: Soil conditions.

	Depth (m)	SPT (N)	Density (kN/m ³)	Adhesion (kPa)	Internal friction angle (°)
Silty sand	0.0~7.5	5/30~16/30	19.0	—	27
Silty clay	7.5~10.5	4/30~12/30	18.5	44.5	—
Silty sand	10.5~24.3	24/30~50/27	19.0	—	38
Weathered soil	24.3~27.0	50/15	19.0	25	31
Weathered rock	27.0~34.0	50/7~50/3	21.0	34	32

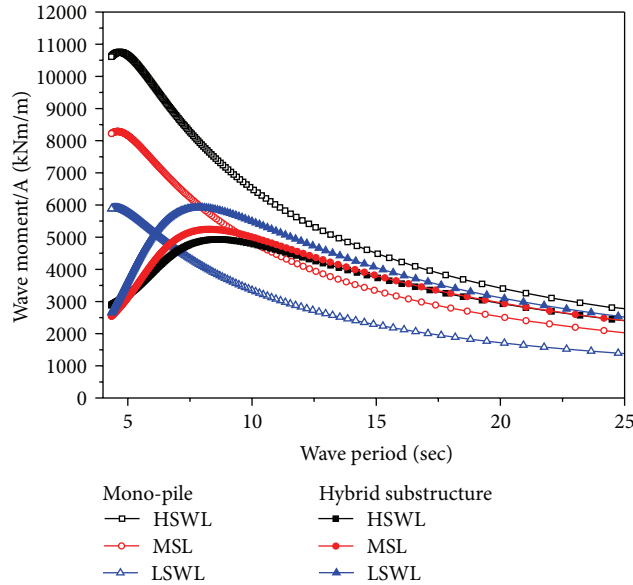


FIGURE 5: Comparison of wave moments for various water depths.

TABLE 7: Stiffness for F_x versus U_x (F_y versus U_y).

Displacement, U_x (m)	Load, F_x (N)
0	0
0.0015	1.127×10^6
0.00319	2.255×10^6
0.00494	3.382×10^6
0.00672	4.510×10^6
0.00852	5.637×10^6
0.0103	6.764×10^6
0.0122	7.892×10^6
0.014	9.019×10^6
0.0159	1.015×10^7
0.0179	1.127×10^7

TABLE 8: Stiffness for F_z versus U_z .

Displacement, U_z (m)	Load, F_z (N)
0	0
3.47×10^{-4}	2.063×10^6
6.93×10^{-4}	4.126×10^6
0.00105	6.189×10^6
0.00142	8.252×10^6
0.00178	1.031×10^7
0.00214	1.238×10^7
0.0025	1.444×10^7
0.00286	1.650×10^7
0.00323	1.857×10^7
0.00359	2.063×10^7

North Sea Wave Project by Hasselmann et al. [13] based on the fact that the wave spectrum is never fully developed. These authors suggested using the family of JONSWAP wave spectra in the design of an offshore structure in a fetch limited area. Therefore, the JONSWAP wave spectrum is applicable to this study. Here also, a safety factor of 1.35 is applied for all cases. The structural results for various water depths are summarized in Table 14. The largest displacement is observed at HSWL. The difference in the displacement at HSWL between pile-soil interaction condition and fixed condition is about

0.0077 m and is smaller than the minimum displacement under pile-soil interaction condition. The dynamic responses exhibit different patterns according to the wave depth and the displacement is strongly influenced by the soil conditions. The structural displacement and the bending moment at HSWL are plotted in Figures 12–15 for various soil conditions.

The structural members and the joints connecting two or more structural members should be checked according to recognized standard. In the present study, ISO 19902 [14] is used for the check of the hybrid substructure under extreme

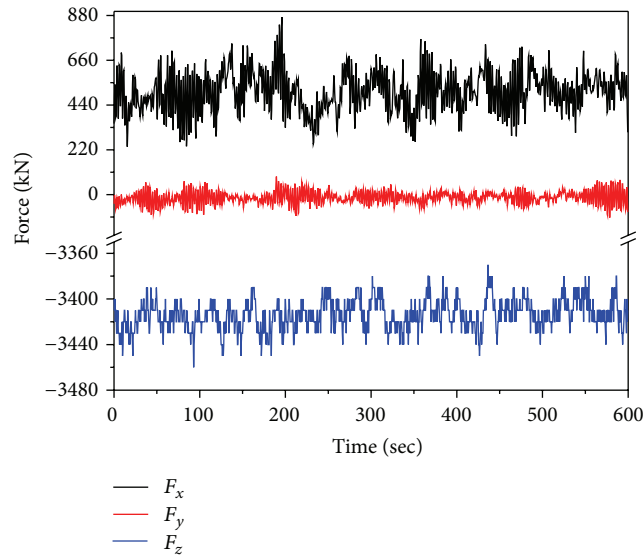


FIGURE 6: Wind forces at TP for DLC 6.2ja-2.

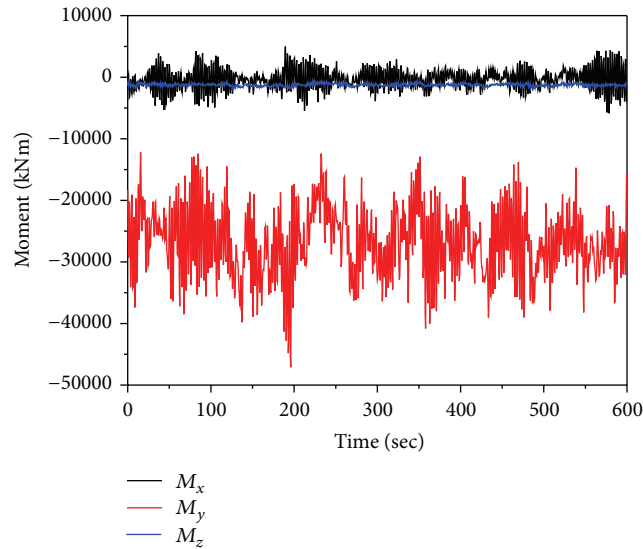


FIGURE 7: Wind moments at TP for DLC 6.2ja-2.

TABLE 9: Stiffness for M_x versus R_x (M_y versus R_y).

Displacement, R_x (rad)	Load, M_x (Nm)
0	0
1.31×10^{-4}	2.200×10^7
2.65×10^{-4}	4.401×10^7
4.01×10^{-4}	6.601×10^7
5.47×10^{-4}	8.801×10^7
6.99×10^{-4}	1.10×10^8
9.41×10^{-4}	1.32×10^8
0.0012	1.54×10^8
0.00153	1.76×10^8
0.00189	1.98×10^8
0.00225	2.20×10^8

TABLE 10: Stiffness for M_z versus R_z .

Displacement, R_z (rad)	Load, M_z (Nm)
0	0
1.0	2.21×10^9

design condition and a value of 250 MPa is adopted for the yield stress of steel. Tables 15–18 show the member unity checks and the joint unity checks for various water depths. The values under regular wave are larger than those under irregular wave. The values with pile-soil condition are larger than those with fixed condition for regular wave but happen to be smaller in case of irregular wave. The values at MSL are the largest for regular wave condition and the values at HSWL are the largest for irregular wave condition. This means that

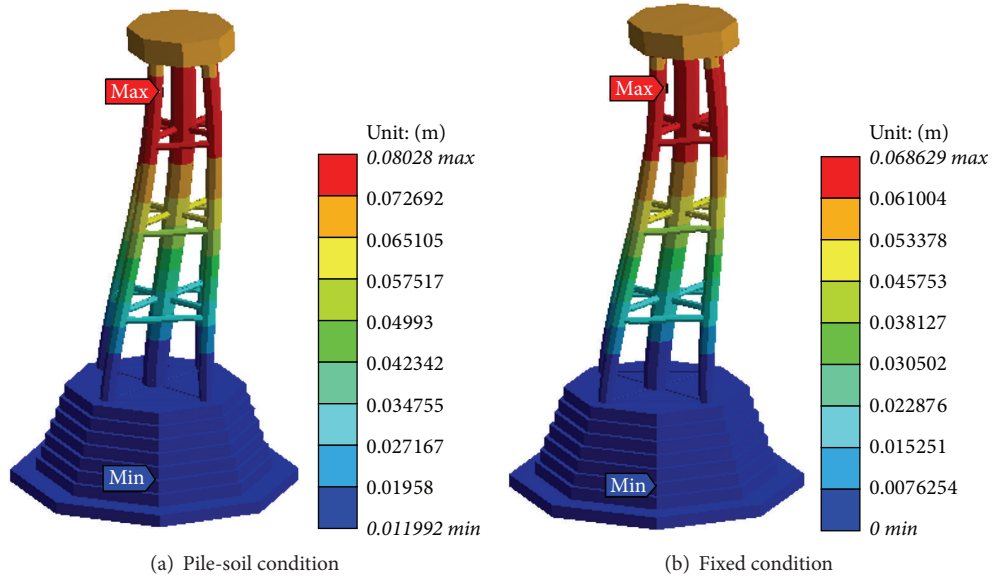


FIGURE 8: Comparison of displacements with regular wave at MSL.

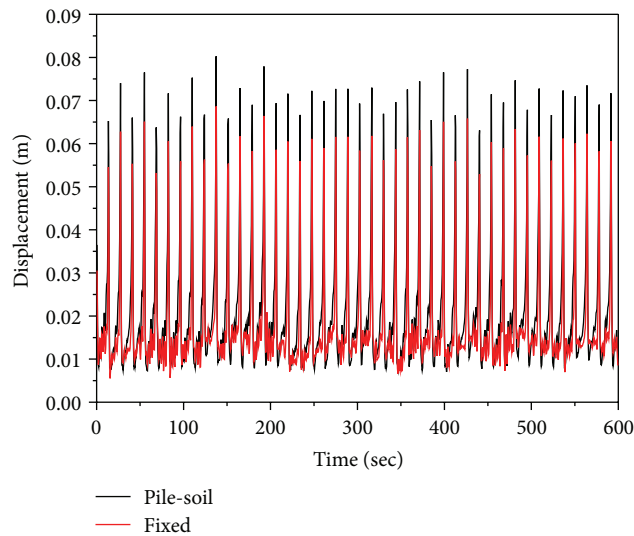


FIGURE 9: Maximum displacements with regular wave at MSL.

TABLE II: Natural frequencies of hybrid substructure (Hz).

Mode	Pile-soil interaction	Fixed condition	Difference (%)
1	0.375	0.392	4.3
2	0.377	0.394	4.3
3	0.867	1.209	28.2
4	0.886	1.873	52.6
5	1.534	1.873	18.0
6	1.534	2.043	24.9
7	1.888	2.256	16.3
8	2.060	4.330	52.4
9	2.641	5.179	49.0
10	2.641	5.179	49.0

the dynamic response of the hybrid substructure is strongly influenced by the wave conditions. The member unity checks for yield 2 at MSL and the joint unity checks for combined (axial + bending) at HSWL are plotted in Figures 16 and 17, respectively. Noting that a value less than 1.0 indicates the satisfaction of the recognized standard, it appears that the structural members and the joints of the hybrid substructure system satisfy the ULS design condition in all cases.

4. Conclusions

The hybrid substructure for 3 MW offshore wind turbine is newly suggested to reduce the wave forces acting on the substructure and to increase the stability against overturning moment. The comparison of the wave forces and moments

TABLE 12: Extreme values at TP due to extreme wind.

	Load case	M_z (kN-m)	M_y (kN-m)	M_x (kN-m)	F_z (kN)	F_y (kN)	F_x (kN)	Safety factor	
M_x	Max	DLC2.2cc+6	9456.5	18087	13125	-3827.3	225.9	-318.4	1.10
M_x	Min	DLC2.2cc+6	-10008	-8834.0	-22000	-3665.7	-378.1	138.2	1.10
M_y	Max	DLC6.2cc-6	1866.1	51227	9174.7	-3738.2	214.1	-927.3	1.10
M_y	Min	DLC6.2ja-2	-1830.9	-52925	-1609.6	-3749.0	-38.1	969.4	1.10
M_z	Max	DLC1.4af2	283.4	3677.1	46109	-4652.0	729.5	-8.73	1.35
M_z	Min	DLC1.4bf2	-2726.2	-10127	-47158	-4580.9	-629.8	177.0	1.35
M_{yz}	Max	DLC6.2ja-2	-1830.9	-52925	-1609.6	-3749.0	-38.1	969.4	1.10
M_{yz}	Min	DLC2.2da+7	47.3	0.16	2.11	-3726.7	15.4	-1.03	1.10
F_x	Max	DLC7.1aa6-5	-5.34	-192.6	11270	-3510.0	236.5	-9.91	1.10
F_x	Min	DLC1.1k-2	3983.2	4726.5	29063	-5254.3	460.3	-11.2	1.50
F_y	Max	DLC1.1g-1	-419.8	2944.5	44202	-5152.8	756.1	-4.80	1.50
F_y	Min	DLC1.4bf4	-3216.8	-10304	-46468	-4557.8	-654.2	179.2	1.35
F_z	Max	DLC6.2ja-2	-1831.3	-52815	-1962.0	-3755.3	-45.4	970.4	1.10
F_z	Min	DLC6.2dc-3	1928.2	50715	-1722.4	-3789.9	-2.68	-942.4	1.10
F_{yz}	Max	DLC6.2ja-2	-1831.3	-52815	-1962.0	-3755.3	-45.4	970.4	1.10
F_{yz}	Min	DLC2.1ab3+6	17.8	-89.3	-505.1	-4597.6	-0.015	0.013	1.35

TABLE 13: Structural results under regular wave condition.

		LSWL		MSL		HSWL	
		Pile-soil	Fixed	Pile-soil	Fixed	Pile-soil	Fixed
Displacement (m)	Max	0.0620	0.0508	0.0802	0.0686	0.0728	0.0615
	Min	0.0115	0.0000	0.0119	0.0000	0.0117	0.0000
Axial force (MN)	Max	2.8239	2.824	2.8254	2.8264	2.8364	2.8364
	Min	-74.888	-74.888	-93.499	-93.489	-113.01	-113.01
Shear force (MN)	Max	8.0512	11.496	7.8327	10.838	9.779	9.7793
	Min	0.0000	0.0000	0.0000	0.0000	0.0000	0.0000
Bending moment (MN-m)	Max	84.369	89.679	109.07	110.93	97.144	97.147
	Min	0.0000	0.0002	0.0001	0.0001	0.0000	0.0000
Torsional moment (MN-m)	Max	2.3783	2.3783	3.0623	3.0932	2.699	2.4025
	Min	-2.3166	-2.3166	-3.0115	-3.0412	-2.6511	-2.372

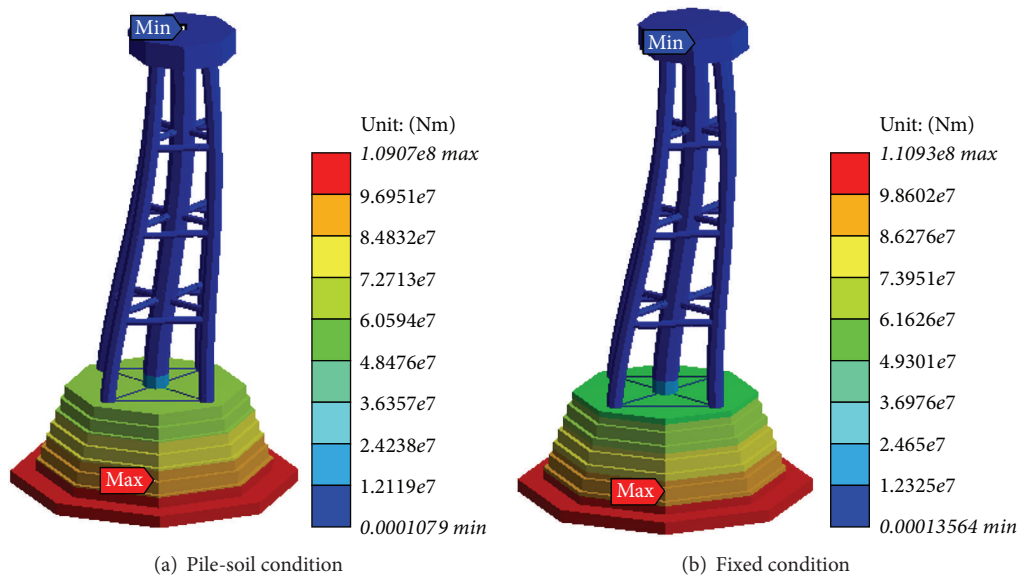


FIGURE 10: Comparison of bending moments with regular wave at MSL.

TABLE 14: Structural results under irregular wave condition.

		LSWL		MSL		HSWL	
		Pile-soil	Fixed	Pile-soil	Fixed	Pile-soil	Fixed
Displacement (m)	Max	0.0340	0.0251	0.0378	0.0305	0.0437	0.0359
	Min	0.0093	0.0000	0.0084	0.0000	0.0092	0.0000
Axial force (MN)	Max	2.2824	2.8266	2.2828	2.8335	2.847	2.847
	Min	-82.77	-82.767	-10.092	-10.091	-119.06	-119.06
Shear force (MN)	Max	7.2287	10.787	6.1829	9.1615	8.0996	8.0999
	Min	0.0000	0.0000	0.0000	0.0000	0.0000	0.0000
Bending moment (MN·m)	Max	34.109	46.133	33.927	42.136	45.724	45.727
	Min	0.0000	0.0001	0.0000	0.0000	0.0000	0.0000
Torsional moment (MN·m)	Max	2.3784	2.3785	2.3786	2.379	2.38	2.38
	Min	-2.3167	-2.3168	-2.317	-2.3174	-2.3185	-2.3185

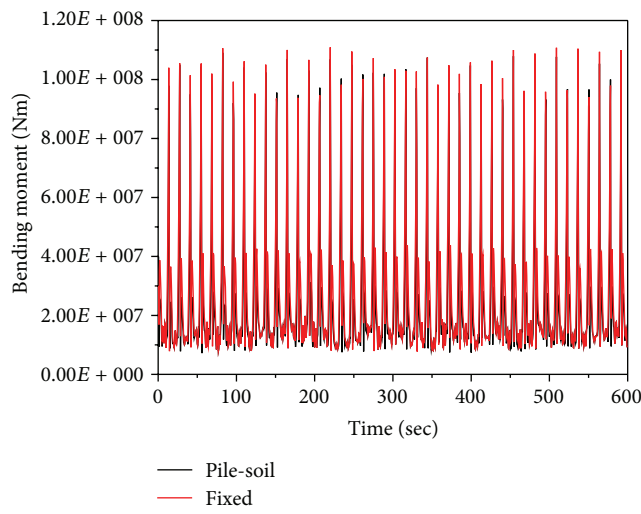


FIGURE 11: Maximum bending moments with regular wave at MSL.

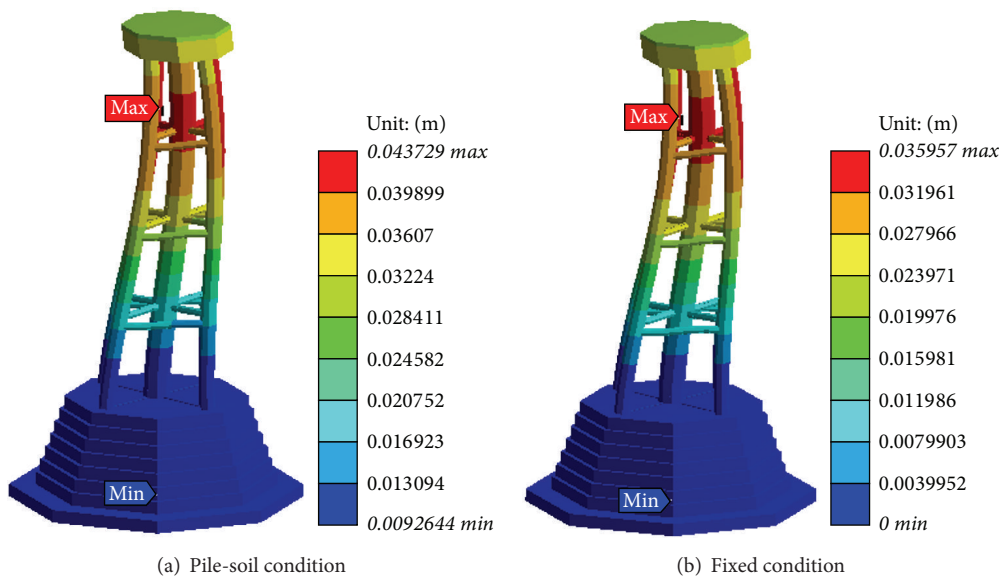


FIGURE 12: Comparison of displacements with irregular wave at HSWL.

TABLE 15: Member unity checks for regular wave.

	LSWL		MSL		HSWL	
	Pile-soil	Fixed	Pile-soil	Fixed	Pile-soil	Fixed
Axial	0.14359	0.14354	0.14295	0.14269	0.13998	0.13998
Shear	0.19755	0.19487	0.27729	0.27351	0.24710	0.24710
Bending	0.52860	0.51713	0.61652	0.60624	0.53309	0.53309
Torsion	0.02232	0.02232	0.02232	0.02232	0.02232	0.02232
Yield 1	0.39809	0.39115	0.58153	0.57361	0.50640	0.50640
Yield 2	0.59662	0.58563	0.68441	0.67472	0.59856	0.59857

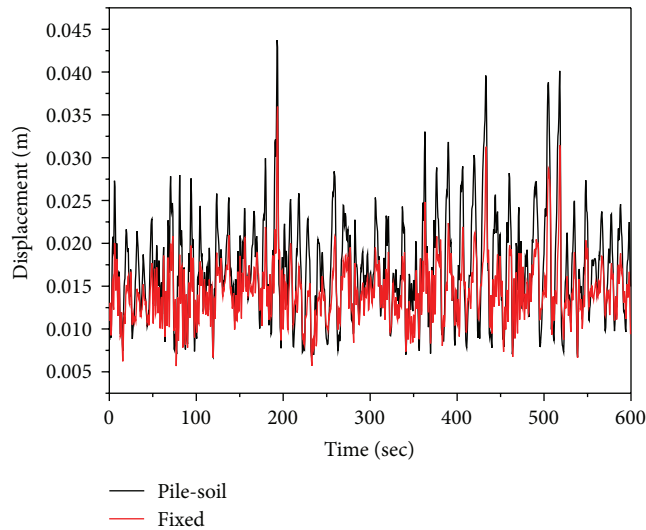


FIGURE 13: Maximum displacements with irregular wave at HSWL.

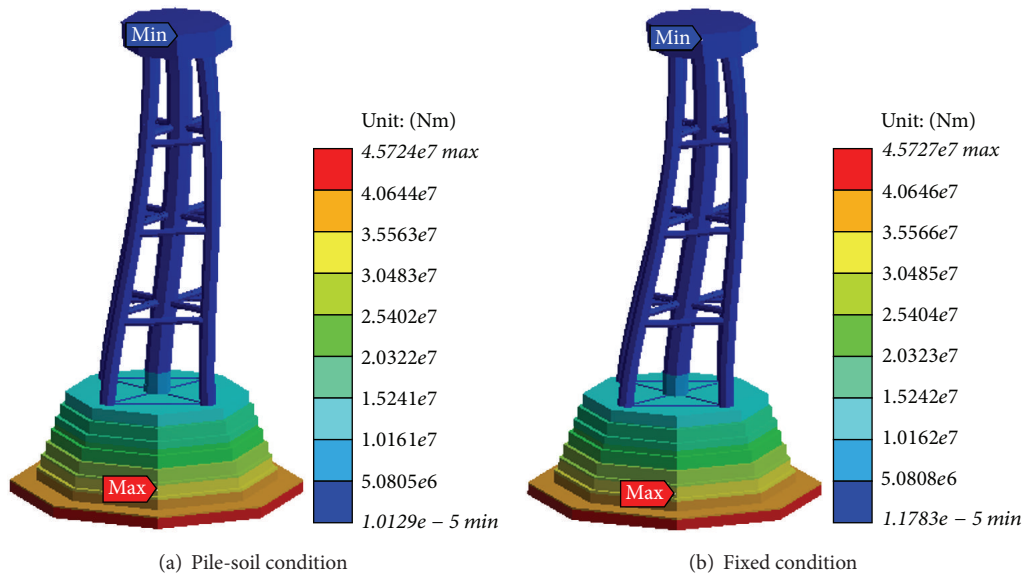


FIGURE 14: Comparison of bending moments with irregular wave at HSWL.

between the hybrid substructure and the mono-pile revealed that installing the multicylinder near free surface can be effective for decreasing the wave forces and installing the gravity-based substructure at the seabed can be very effective for increasing the stability against overturning moment. The

structural analysis of the hybrid substructure was carried out by ANSYS ASAS for various wave conditions using the wind forces obtained from GH-Bladed and the stiffness matrices for pile-soil foundation system and showed that the dynamic responses of the hybrid substructure were strongly influenced

TABLE 16: Member unity checks for irregular wave.

	LSWL		MSL		HSWL	
	Pile-soil	Fixed	Pile-soil	Fixed	Pile-soil	Fixed
Axial	0.15328	0.15321	0.15296	0.15275	0.15154	0.15154
Shear	0.10457	0.10489	0.13127	0.13303	0.16796	0.16797
Bending	0.23846	0.24313	0.29839	0.30532	0.34586	0.34586
Torsion	0.02626	0.02626	0.02626	0.02626	0.02626	0.02626
Yield 1	0.26791	0.26798	0.26823	0.26844	0.35680	0.35680
Yield 2	0.30494	0.30978	0.36472	0.37194	0.41247	0.41247

TABLE 17: Joint unity checks for regular wave.

	LSWL		MSL		HSWL	
	Pile-soil	Fixed	Pile-soil	Fixed	Pile-soil	Fixed
Axial	0.05868	0.05920	0.03708	0.03753	0.02884	0.02884
In-plane bending	0.75487	0.74347	0.94235	0.94135	0.92134	0.92134
Out-of-plane bending	0.11832	0.11895	0.11375	0.01131	0.09605	0.09605
Combined (axial + bending)	0.69249	0.67478	0.96058	0.96008	0.94048	0.94049

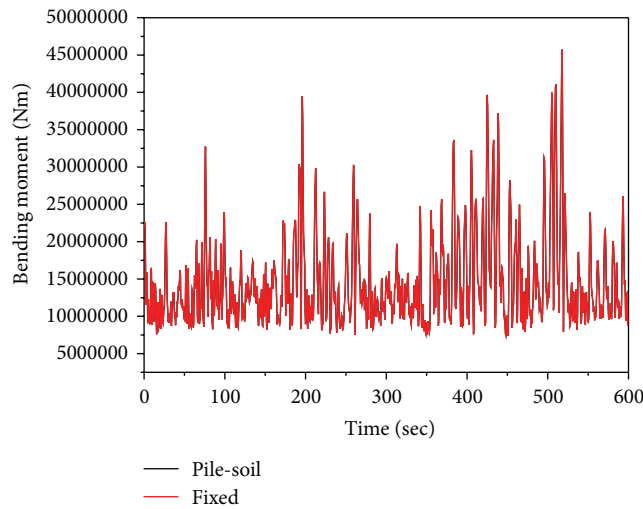


FIGURE 15: Maximum bending moments with irregular wave at HSWL.

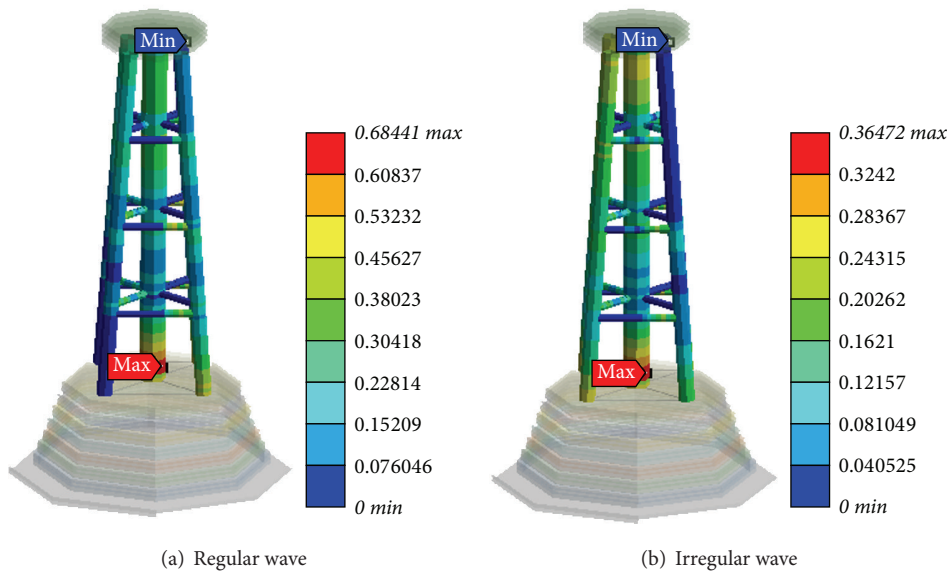


FIGURE 16: Member unity checks for yield 2 at MSL.

TABLE 18: Joint unity checks for irregular wave.

	LSWL		MSL		HSWL	
	Pile-soil	Fixed	Pile-soil	Fixed	Pile-soil	Fixed
Axial	0.02433	0.02420	0.02161	0.02181	0.02121	0.02121
In-plane bending	0.37216	0.37455	0.48123	0.48824	0.61702	0.61703
Out-of-plane bending	0.06896	0.07041	0.06833	0.06973	0.07128	0.07128
Combined (axial + bending)	0.20636	0.20991	0.30202	0.30911	0.44869	0.44870

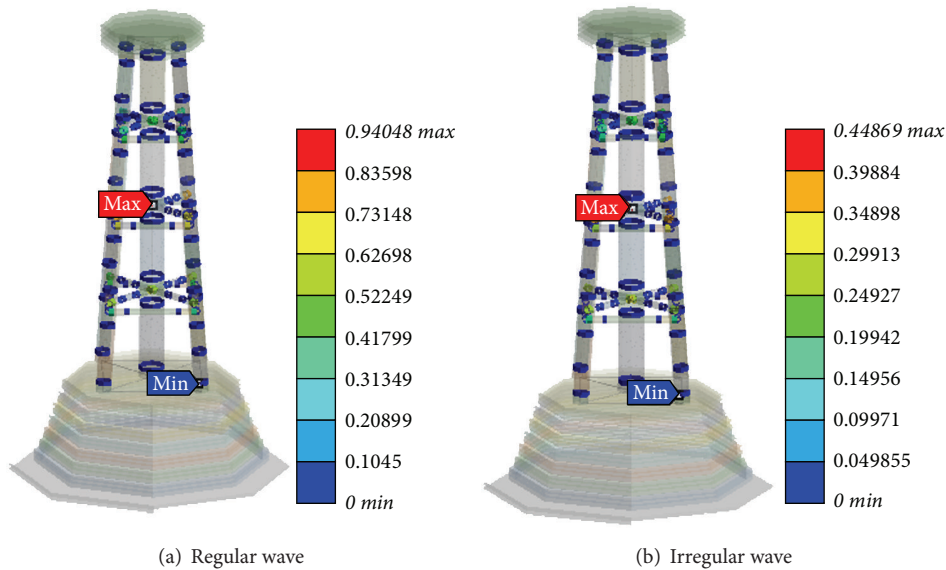


FIGURE 17: Joint unity checks for combined (axial + bending) at HSWL.

by the soil conditions (Table 6) and the wave conditions. The hybrid substructure system was also seen to secure structural safety with respect to ULS (ultimate limit state) design condition for all wave conditions. In addition, the comparison of the first natural frequency with 1P and 3P frequencies showed that the hybrid substructure exhibited soft-stiff design properties and indicated that resonance between the wind turbine and the hybrid substructure would not occur. Consequently, the suggested hybrid substructure can be effective for reducing the hydrodynamic effects and construction costs for the future wind turbines to be installed in the southwestern sea of South Korea.

Competing Interests

The authors declare that there are no competing interests regarding the publication of this paper.

Acknowledgments

This research was supported by Korea Institute of Energy Technology Evaluation and Planning through the research projects “Development of hybrid substructure systems for offshore wind farm (20123010020110)” and “Development of 3 kW cylindrical wave energy system with horizontal rotation for increasing gross generation (20153030071630).”

References

- [1] M. Klose, P. Dalhoff, and K. Argyriadis, “Integrated load and strength analysis for offshore wind turbines with jacket structures,” in *Proceedings of the European Offshore Wind Energy Conference and Exhibition*, Berlin, Germany, December 2007.
- [2] J. Weinzettel, M. Reenaas, C. Solli, and E. G. Hertwich, “Life cycle assessment of a floating offshore wind turbine,” *Renewable Energy*, vol. 34, no. 3, pp. 742–747, 2009.
- [3] J. M. Jonkman, “Dynamics of offshore floating wind turbines-model development and verification,” *Wind Energy*, vol. 12, no. 5, pp. 459–492, 2009.
- [4] Z. Gao, N. L. J. Saha, T. Moan, and J. Amdahl, “Dynamic analysis of offshore fixed wind turbines under wind and wave loads using alternative computer codes,” in *Proceedings of the 3rd TORQUE Conference*, Crete, Greece, 2010.
- [5] D. Kaufer, T. Fischer, F. Vorpahl, W. Popko, and M. Kühn, “Different approaches to modeling jacket support structures and their impact on overall wind turbine dynamics,” in *Proceedings of the 10th German wind Energy Conference (DEWEK '10)*, Bremen, Germany, 2010.
- [6] E. Lozano-Minguez, A. J. Kolios, and F. P. Brennan, “Multi-criteria assessment of offshore wind turbine support structures,” *Renewable Energy*, vol. 36, no. 11, pp. 2831–2837, 2011.
- [7] M. B. Zaaier, “Comparison of monopile, tripod, suction bucket and gravity base design for a 6 MW turbine,” in *Proceedings of the Offshore Wind Energy in Mediterranean and Other European Seas Conference*, Naples, Italy, 2003.

- [8] S. Føreland, M. O. Rastad, and K. Aas-Jacobsen, "A parametric study on fixed bottom wind turbines in the North Sea," in *Proceedings of the Nordic Steel Construction Conference*, p. 831, Oslo, Norway, September 2012.
- [9] M.-S. Park, Y.-J. Jeong, and Y.-J. You, "Structural analysis of a hybrid substructure with multi-cylinder for 5 MW offshore wind turbines," in *Proceedings of the ASME 33rd International Conference on Ocean, Offshore and Arctic Engineering (OMAE '14)*, San Francisco, Calif, USA,, June 2014.
- [10] IEC, "Wind turbines-part 3: design requirements for offshore wind turbines," IEC 61400-3, International Electrotechnical Commission, 2009.
- [11] W. Shi, J. H. Han, C. W. Kim, D. Y. Lee, H. K. Shin, and H. C. Park, "Feasibility study of offshore wind turbine substructures for southwest offshore wind farm project in Korea," *Renewable Energy*, vol. 74, pp. 406–413, 2014.
- [12] J. G. Espinosa, "Design and calculus of the foundation structure of an offshore monopile wind turbine," Polytechnic University of Catalonia, Barcelona, Spain, 2012.
- [13] K. Hasselmann, W. Sell, D. B. Ross, and P. Müller, "A parametric wave prediction model," *Journal of Physical Oceanography*, vol. 6, no. 2, pp. 200–228, 1976.
- [14] ISO, "Petroleum and natural gas industries—fixed steel offshore structures," ISO 19902, International Organization for Standardization, Geneva, Switzerland, 2007.

Research Article

Relationships between Imperfections and Shear Buckling Resistance in Web Plate with Sectional Damage Caused by Corrosion

Jin-Hee Ahn,¹ Shigenobu Kainuma,² Won-Hong Lee,¹ Youn-Ju Jeong,³ and In-Tae Kim⁴

¹Department of Civil Engineering, Gyeongnam National University of Science and Technology, Jinju, Gyeongnam 660-758, Republic of Korea

²Department of Civil Engineering, Kyushu University, Fukuoka 819-0395, Japan

³Structural Engineering Research Institute, Korea Institute of Civil Engineering and Building Technology, Goyang, Gyeonggi 411-712, Republic of Korea

⁴Department of Civil Engineering, Pusan National University, Pusan 609-735, Republic of Korea

Correspondence should be addressed to In-Tae Kim; itkim@pusan.ac.kr

Received 10 May 2016; Accepted 16 June 2016

Academic Editor: Guillermo Rus

Copyright © 2016 Jin-Hee Ahn et al. This is an open access article distributed under the Creative Commons Attribution License, which permits unrestricted use, distribution, and reproduction in any medium, provided the original work is properly cited.

This study deals with the relationship between imperfections and shear buckling resistance of web plates with sectional damage caused by corrosion. To examine the imperfection effect on the shear buckling resistance of a web plate with sectional damage, a series of nonlinear finite element (FE) analyses were carried out for a web plate with sectional damage, which was assumed as local corrosion damage. For considering imperfections of the web plate in the girder, initial out-of-plane deformation was introduced in the FE analysis model. Using the FE analysis results, the changes in the shear buckling resistance of the web plate with sectional damage were quantitatively examined and summarized according to the aspect ratio, boundary conditions, and height of the damaged section of the web plate. The effects of web imperfections on the shear buckling resistance were evaluated to be little compared to that of the web plate without sectional damage. The shear buckling resistance was shown to significantly change in the high-aspect-ratio web plate. A simple evaluation equation for the shear buckling resistance of a web plate with sectional damage was modified for use in the practical maintenance of a web plate in corrosive environments.

1. Introduction

For steel girder bridges, the structural member at the end girder near the support can be easily exposed to rain water, high humidity, and wet depositions, which are causes of atmospheric corrosion. Thus, research related to corrosion problems, focused on end girders, has been conducted to determine the residual strength and behaviors of corroded end girders to improve their strengthening methods and maintenance. For the end girder part, the lower region of the web panel, the stiffener on the bearing, and the lower flange on the sole plate have been considered to be the regions vulnerable to corrosion due to their atmospheric corrosion environment, which consists of high humidity caused by

poor air circulation, sediments, and rainwater (antifreeze) [1–5]. Corroded lower flanges in end girders have a relatively smaller effect on the flexible resistance of a girder due to their structural behaviors under applied moment conditions. Therefore, the lower region of a web panel and a stiffener on a bearing are the main components that should be examined for residual strength or local structural behaviors when conducting research on corrosion problems focused on end girders. A lot of research on the structural behaviors of web panels with lower regional sectional damage has been carried out to examine the shear buckling resistance and shear buckling behaviors [1–12]. Many researches were conducted in Japan, where there are severe corrosion environments and many old structures [2, 4, 10, 11]. The research mainly dealt with

the shear buckling resistance and behaviors of web panels using experimental and numerical methods [3–5]. The shear buckling strength of a web panel is affected by the geometrical properties of the web panel. Imperfections and residual stress also affect its shear buckling strength. However, most of the previously conducted research deals with the corroded area and level of web plate as the main parameters affecting shear buckling resistance [3–6]. Imperfections such as eccentric deformation and residual stress were partially considered [13, 14]. Therefore, they were not evaluated to examine the change in their effect on shear buckling resistance. The residual stress of a web panel cannot be clearly determined until after its long service period. In contrast, the eccentric deformation of a web plate can occur during its service period. Therefore, the imperfection effect of eccentric deformation on the shear buckling strength can be considered to determine the lower boundary of the shear buckling resistance of a web panel with local sectional damage caused by corrosion. In this study, therefore, the imperfection effects of eccentric deformation on the shear strengths of web panels with local sectional damage were examined using finite element (FE) analysis. An allowable imperfection level suggested by the design guidelines for the steel structure was considered to identify the shear buckling behaviors of web panels. After identifying a shear buckling analysis model incorporating imperfections, parametric studies were conducted to quantitatively evaluate the shear buckling strengths and the modified shear buckling reduction factor for the damaged web section with imperfections.

2. FE Analysis Model of Sectional Damaged Web Plate with Imperfections

In previous studies, Kim et al. conducted a shear loading test of a web plate with artificial sectional damage to experimentally examine the shear buckling resistant behaviors [3]. FE analyses on shear buckling behaviors of a sectional damaged web plate caused by corrosion were conducted to suggest changes in the residual shear buckling strength based on geometrical properties of the web and corrosion level [4]. The shear buckling failure mode of the web plate was also examined considering the corrosion pattern [5]. In previous studies, however, imperfection effect as eccentric deformation was not considered in suggesting its residual shear buckling strength. In this study, an FE analysis model including imperfections was made based on previous models [3, 4].

2.1. Geometrical Properties of Web Plates. In this study, imperfection was considered as a main parameter. Eccentric deformation of the web plate was considered as the initial imperfection. Thus, three different initial imperfection magnitudes of $H/100,000$, $H/500$, and $H/100$ were used to examine the imperfections of the web panel, where H is the web height of the web panels. An arbitrary small initial imperfection level of $H/100,000$ was incorporated in an attempt to find a bifurcation-type buckling load. $H/100$ is the maximum imperfection level allowed by the Bridge Welding Code [15], and $H/500$ is an intermediate level between the

two values. For web plate models, a two-web-panel plate girder was selected that had a height of 800 mm, a flange width of 200 mm, a flange thickness of 16 mm, and a web thickness of 6 mm. These dimensions are similar to previous studies [3]. Figure 1 shows the basic dimensions of the FE analysis model.

For the sectional area damaged by corrosion, a damaged area was selected from the lower flange to 100 mm and 200 mm, as shown in Figure 1. For the selected corroded area, web thickness was decreased from the design thickness for both of the web plates. To consider the aspect ratio of the web plate and the boundary conditions based on the deterioration of the support (bearing) due to corrosion and depositions around the support, the aspect ratios were also changed to 1.0, 1.25, and 1.50, and their boundary conditions were changed from a simply supported case to a hinge-supported case.

The following describe the numerical parameters in this study:

- (1) Imperfection levels (initial eccentric deformation): 0, $H/100$, $H/500$, and $H/100,000$.
- (2) Sectional damaged web height (h_c): 100 mm to 200 mm from the lower flange.
- (3) Web plate thickness (h_c): changed to 1 mm from the design thickness.
- (4) Web plate aspect ratio (l_w/h_c): 1.0, 1.25, and 1.50.
- (5) Boundary condition: simply supported model and hinge-supported model (with deterioration of support).

2.2. FE Analysis Model. To numerically examine the shear buckling strength of web panels, eigenvalue and incremental nonlinear analyses were conducted. MARC Mentat 2010 was used as the numerical FE program and the web plate model was constructed using a four-node shell element with a 10 mm mesh size, as shown in Figure 2 [16]. The web plate model was assumed to exhibit elastic, perfectly plastic behavior, and the von Mises yield criterion was used for material plasticity. An incremental load was applied at the center span of the upper flange. Its material was determined to have Young's Modulus of 206,000 MPa, a nominal yield stress of 359 MPa, and Poisson's ratio of 0.3 [3]. To consider the imperfection effect in the FE analysis model, artificial eccentric deformation was applied to the center of the web plate girder model according to each imperfection level. For the previously mentioned boundary condition cases of the FE analysis models, the left and right supports were changed to hinges or rollers, depending on the supported conditions, as shown in Table 1. Lateral translations and rotations of both supports were restricted, and longitudinal translation of the center of the lower flange was also restricted.

2.3. FE Model Comparison. To validate the FE analysis model, an FE analysis model of the shear loading test specimen in the previous study [3, 4] was also constructed for comparison with the FE analysis results from this study. In cases of shear loading tests, out-of-plane deformation can be a major

TABLE I: Boundary conditions.

Boundary condition	Boundary	u_x	u_y	u_z	r_x	r_y	r_z
Simple support	Boundary A	Movable	Fixed	Fixed	Fixed	Fixed	Movable
	Boundary B	Movable	Fixed	Fixed	Fixed	Fixed	Movable
	Boundary C	Fixed	Movable	Movable	Movable	Movable	Movable
Hinge support	Boundary A	Fixed	Fixed	Fixed	Fixed	Fixed	Movable
	Boundary B	Fixed	Fixed	Fixed	Fixed	Fixed	Movable
	Boundary C	Movable	Movable	Movable	Movable	Movable	Movable

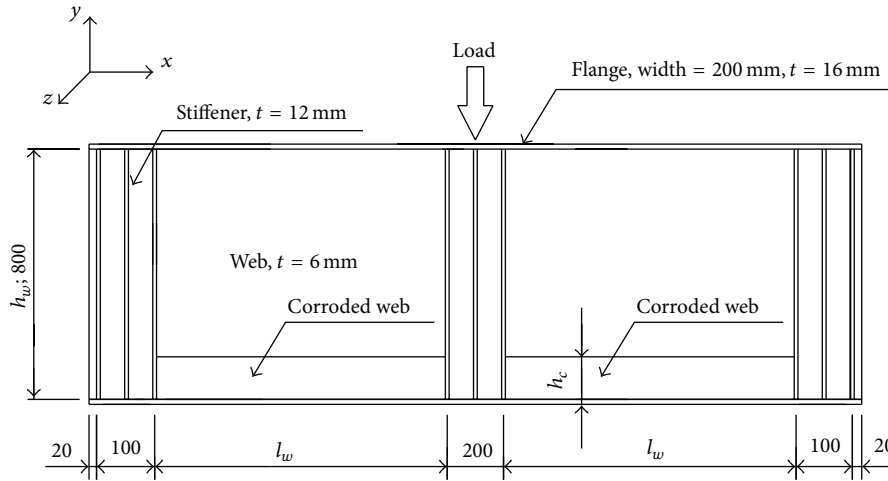


FIGURE 1: Dimensions of FE analysis model (unit: mm).

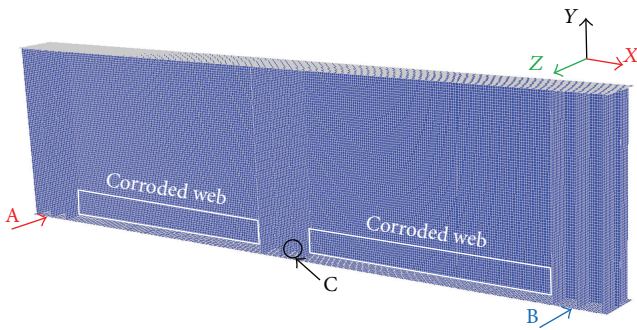


FIGURE 2: FE analysis model.

concern in shear buckling behaviors of web panels. Thus, out-of-plane displacements of each test specimen were directly compared with those of the constructed FE analysis model. In previous shear loading tests and analysis studies, corrosion conditions were considered as a main parameter and initial eccentric deformations were not identified. Therefore, initial imperfection effects were not considered in previous studies [3, 4]. In the validation model, three initial eccentric deformations of the web plate were considered as imperfections, and both supports were considered as hinge supports, like the support conditions of previous shear loading tests [3, 4].

Figure 3 shows the out-of-plane displacement comparison at the web center between the shear buckling test results and the FE analysis results under varying initial eccentric

deformations (imperfection magnitudes) of the web panel. As shown in the figure, if there is no initial imperfection in the web panel, out-of-plane displacement does not occur before elastic shear buckling of the web panel. After elastic shear buckling of the web panel, out-of-plane displacement appears laterally in the FE analysis results without initial imperfections, as in the previous study [4]. In the results of the shear loading test specimens [3], their out-of-plane displacements could be directly found without the lateral resistance of the web plate after applying shear load to all test specimens. Table 2 and Figure 4 summarized the comparison of shear buckling strengths of test specimens and FE analysis results. For the Ch00T6 specimen without sectional damage, its out-of-plane displacement behavior shows that it is similar to that of the analysis model, excluding the $H/100,000$ cases, in that the test results were similar to the analysis model as initial imperfection magnitude increased. For the $H/500$ case, the tendency toward out-of-plane displacements was shown to be in agreement with those of the test results. The shear buckling strength of FE analysis result was also shown to be close to those of the test results for $H/100$, although it was stiffer than the other cases in the Ch00T6 specimen. Thus, the initial eccentric deformation of the Ch00T6 specimen could be thought to be about 1.6 mm. Other specimens with sectional damage also showed similar results to the analysis results of the Ch00T6 specimen. They also had about 1.6 mm of initial eccentric deformations (imperfection magnitudes). Their shear buckling strength test results were

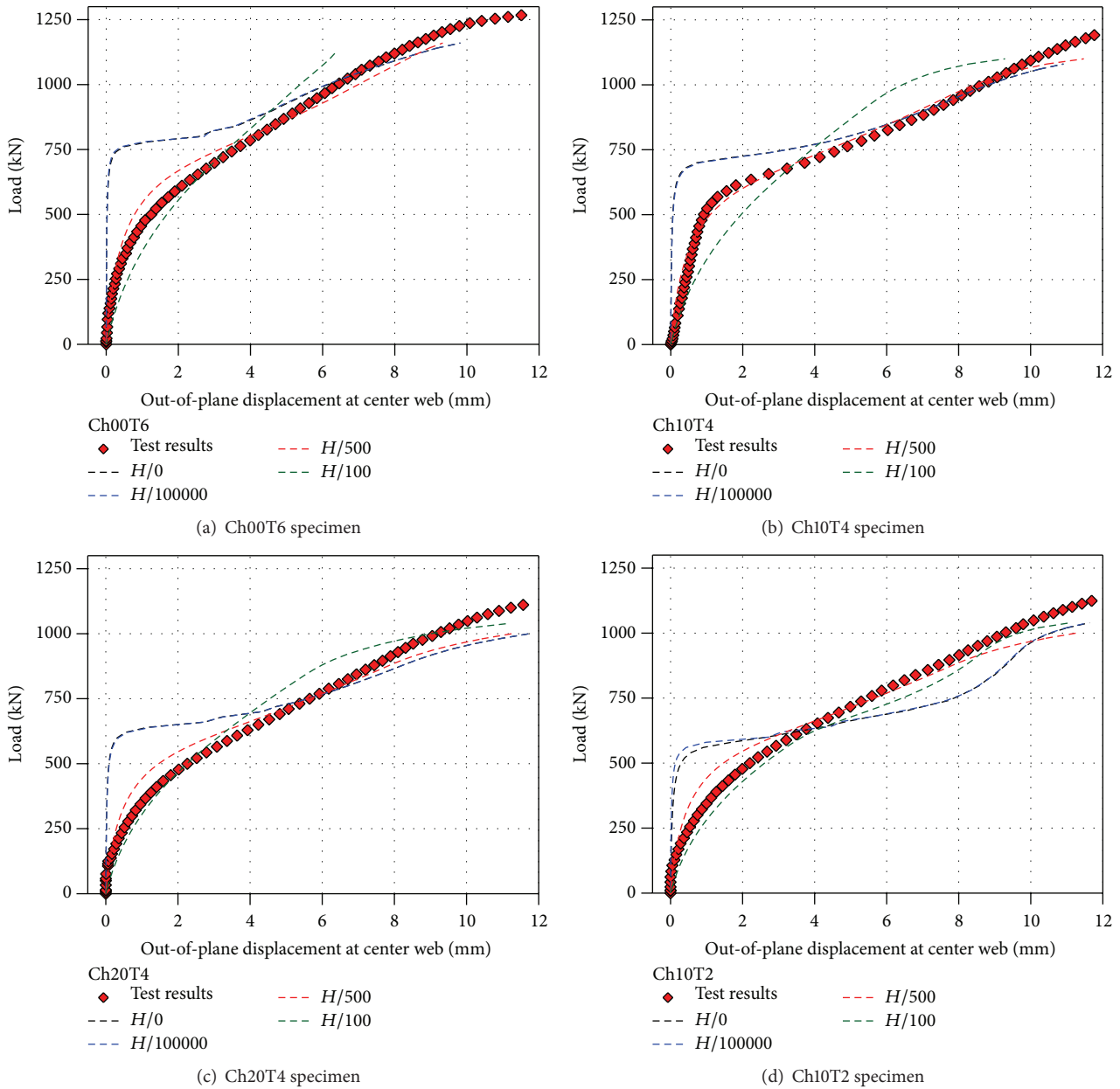


FIGURE 3: Out-of-plane displacement comparisons at center web of shear buckling test specimens.

approximately 110% of the FE analysis results. From the FE analysis results, their shear buckling strengths were shown to slightly decrease, depending on the increase in the initial eccentric deformations.

For the shear loading test specimens, typical shear failures of the webs with a tension field band were shown from the shear resistant behavior of the web, as shown in Figure 5(i) [3]. In particular, for the specimen with sectional damage, the tension field bands were larger and extended into the sectional damaged web plate. An additional pronounced shear-bending tension field occurred in the sectional damaged web [3]. To evaluate the differences between the shear failure modes of the web plate with sectional damage more clearly, the failure modes were also compared according to

their initial eccentric deformation. Since the out-of-plane displacements of the $H/500$ and $H/100$ cases were shown to be similar to the test results, the representative shear failure modes of the test results were compared with those of the FE analysis, as shown in Figure 5. Their comparison showed a typical diagonal tension field, as well as a pronounced shear tension field in the sectional damaged web plate regardless of their initial eccentric deformation levels, although the point of the maximum out-of-plane displacement slightly decreased. This is shown in Figure 5.

By comparing their out-of-plane displacement behavior, the FE analysis model with initial eccentric deformation was considered to well simulate the shear buckling behaviors of a web plate with an initial imperfection. An initial eccentric

TABLE 2: Shear buckling strengths of test specimens and FE analysis results.

	Corroded height (mm)	Corroded thickness (mm)	Corroded volume ratio (%)	Shear buckling strength (P_u), kN				
				Tests	$H/0$	$H/10000$	$H/500$	$H/100$
Ch00T6	00	0/00	00	1286.54	1160.0	1160.0	1160.0	1140.0
Ch10T4	100	2	4.17	1275.75	1120.0	1120.0	1120.0	1100.0
Ch20T4	200	2	8.33	1152.46	1080.0	1080.0	1080.0	1060.0
Ch10T2	100	4	8.33	1186.37	1060.0	1060.0	1060.0	1040.0

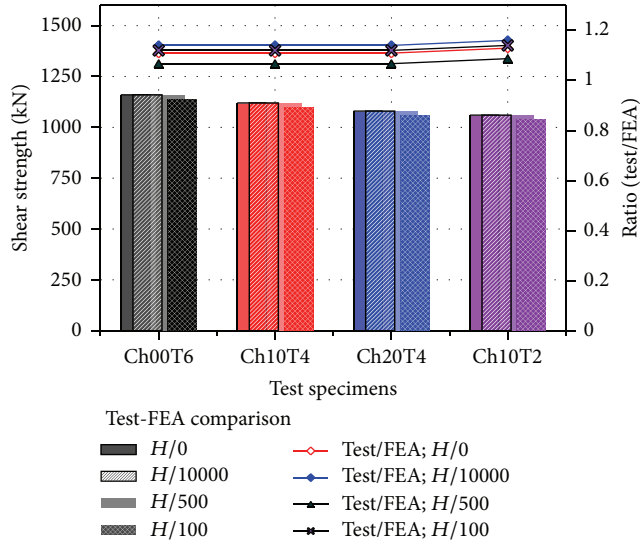


FIGURE 4: Comparison of test and FE analysis results.

deformation of the web plate could slightly affect the shear buckling strength. Therefore, the FE analysis model and FE analysis parameters are suitable for evaluating the shear buckling strength of a web plate with initial eccentric deformations and for examining the relationship between imperfections and shear buckling strength of a web plate with sectional damage.

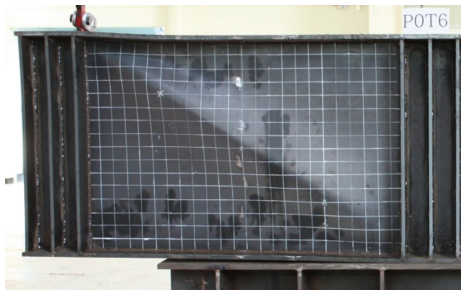
3. Discussion of FE Analysis Results

3.1. Shear Buckling Resistance Depending on Imperfection

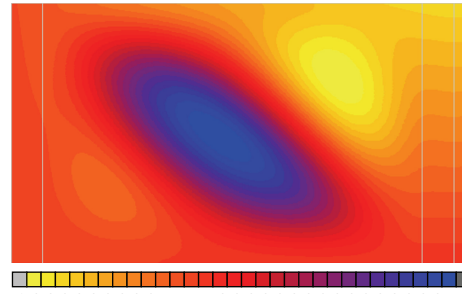
3.1.1. Relationship between Imperfection and Corrosion Height. Imperfection effects on shear buckling strengths of a web plate with sectional damage caused by corrosion were compared using an FE analysis model and shear loading test results. Three different initial eccentric deformations of $H/100,000$, $H/500$, and $H/100$ in an 800×1200 mm web plate were compared for simple supported conditions. As their shear buckling behaviors were shown to be similar according to test results and model comparisons, the change in the shear buckling strength was examined based on the initial eccentric deformations of the web at each damaged web height (100 mm and 200 mm). Table 3 summarizes the shear buckling strengths of web panels with sectional damage based on their imperfection conditions. Using the data from Table 3, Figure 6 shows the change in the shear buckling strengths of

a web plate with imperfections with varying damaged web thickness and corrosion volume. In web panels with a 100 mm sectional damaged web plate, the shear buckling strengths without imperfection changed from 1160.0 to 959.9 kN, and the shear buckling strengths with an $H/00$ eccentric deformation changed from 1140.0 to 940.0 kN. In web panels with a 200 mm sectional damaged web plate, the strengths without imperfection changed from 1160.0 to 779.9 kN, and the strengths with an $H/00$ eccentric deformation changed from 1140.0 to 779.9 kN. These results showed that the height of the sectional damaged web plate affected the decrease in the shear buckling strengths of web panels from 17.54% to 32.77% due to the decreased shear resistance of the web plate, as shown in Table 3 and Figure 6. These results were similar to the decrease in the shear buckling strengths of web panels with increasing sectional damaged web plate thickness and height found in the previous study [4]. For $H/100,000$ and $H/500$ eccentric deformations of web panels, their effects were shown to be similar to those of the web plate without eccentric deformation, as shown in the out-of-plane displacement relationship comparisons of the shear loading test in Figure 3 and Table 2. In particular, in the case of $H/100$, its values decreased slightly more than in the other cases, and its values were evaluated to be 2% of the values of the web plate without eccentric deformation. Thus, it was determined that the effect of the initial eccentric deformation of a web plate is relatively less than that of the sectional damaged web plate.

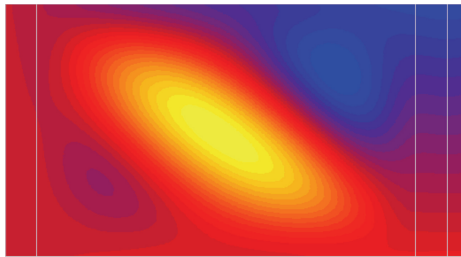
3.1.2. Relationship between Imperfections and Boundary Conditions. In the previous study [4], the critical shear buckling value of a web plate was affected by the boundary conditions, and shear buckling resistance was steadily decreased according to sectional damage related to web corrosion. The boundary conditions had very little effect on shear buckling strengths [4]. In this study, the effect of initial eccentric deformation on shear strength was also examined to determine the relationship between shear strength and boundary condition. The same initial eccentric deformations and sectional damaged height conditions as the imperfection model cases were applied to the FE analysis model, and the model boundary conditions were only changed by incorporating a hinge considered to be a deteriorated boundary. Table 4 and Figure 7 summarize the shear buckling strengths of a web plate with sectional damage based on their imperfection and boundary conditions. With regard to the imperfection levels, the shear buckling strengths were evaluated to be similar to values of the simply supported condition regardless of



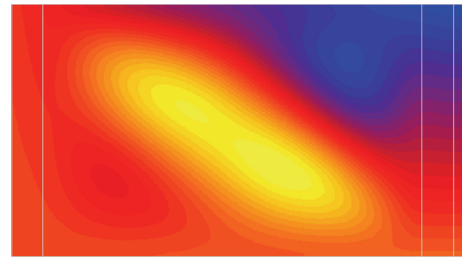
(i) Failure mode of test model



(ii) Out-of-plane displacement contour without imperfection



(iii) Out-of-plane displacement contour with $H/500$

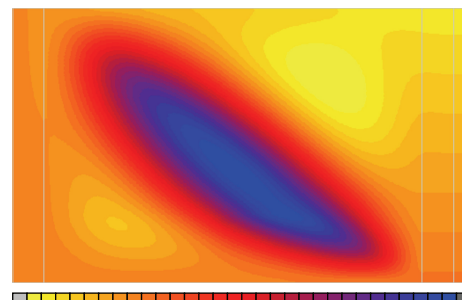


(iv) Out-of-plane displacement contour with $H/100$

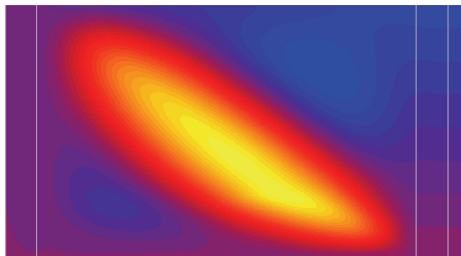
(a) Ch00T6 specimen



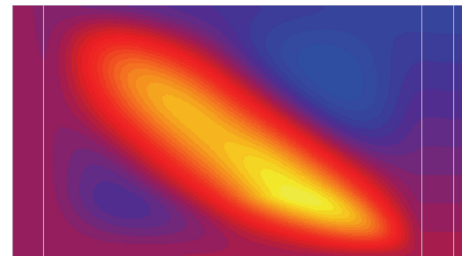
(i) Failure mode of test model



(ii) Out-of-plane displacement contour without imperfection



(iii) Out-of-plane displacement contour with $H/500$



(iv) Out-of-plane displacement contour with $H/100$

(b) Ch20T4 specimen

FIGURE 5: Failure mode comparisons of shear buckling test specimens depending on imperfection.

TABLE 3: Shear buckling resistance of a web plate with imperfection (kN).

Height (mm)	Web corroded condition		Imperfection (initial eccentric deformation)			
	Corroded thickness (mm)	Corroded volume (%)	0	$H/100000$	$H/500$	$H/100$
100	0	0	1160.0	1160.0	1160.0	1140.0
	1	2.08	1160.0	1160.0	1160.0	1140.0
	2	4.17	1140.0	1140.0	1140.0	1120
	3	6.25	1100.0	1100.0	1100.0	1080.0
	4	8.33	1060.1	1060.1	1060.1	1039.9
	5	10.42	1020.0	1020.0	1020.0	1000.0
	6	12.50	959.9	959.9	959.9	940.0
200	0	0	1160.0	1160.0	1160.0	1140.0
	1	2.08	1160.0	1160.0	1160.0	1140.0
	2	4.17	1119.9	1119.9	1119.9	1100.0
	3	6.25	1039.9	1039.9	1039.9	1020.0
	4	8.33	959.9	959.9	959.9	940.0
	5	10.42	920.0	920.0	920.0	900.1
	6	12.50	779.9	779.9	779.9	779.9

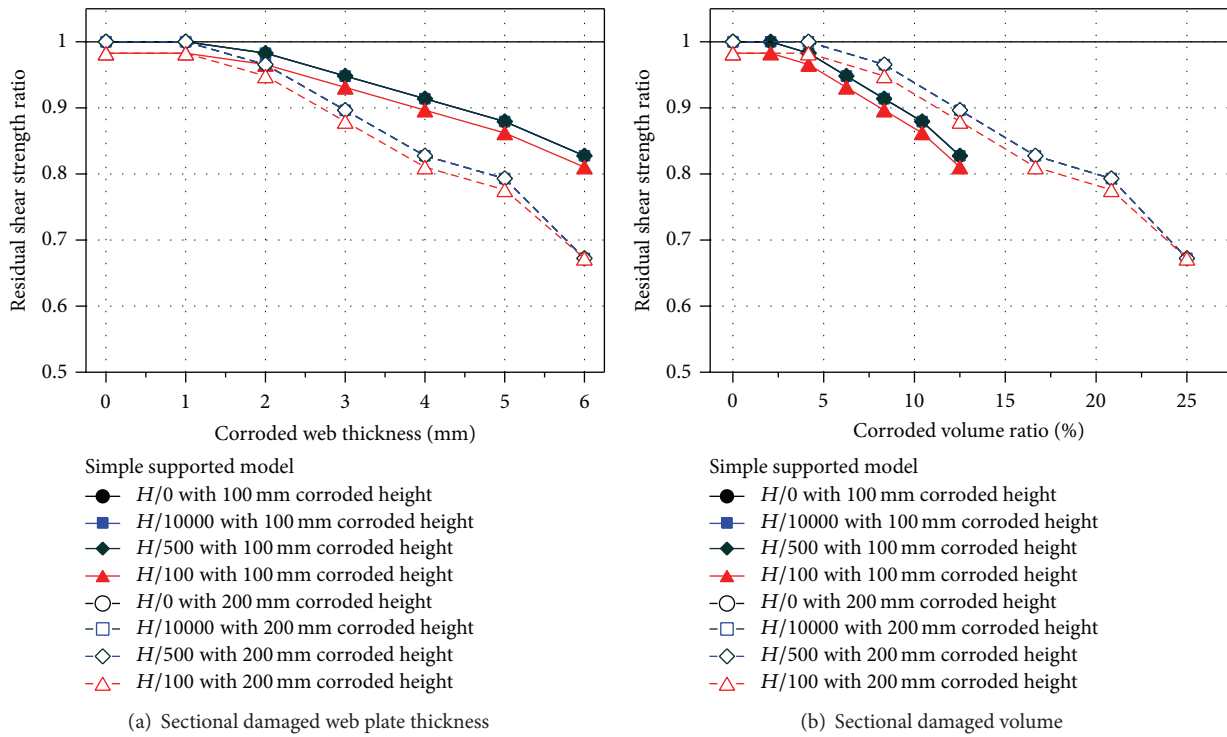


FIGURE 6: Shear buckling resistance ratios with roller support.

the boundary conditions, as shown in Table 4 and Figure 7. The shear buckling strengths steadily decreased at the same level as those of the simply supported cases. Thus, it was determined that boundary condition effect is not related to the relationship between imperfection and shear buckling strength of a web panel with sectional damage.

3.1.3. Relationship between Imperfection and Aspect Ratio Condition. In this study, an 800×1200 mm web plate was used,

because the FE model was based on the shear loading test specimen. Three aspect ratios were considered as analysis parameters to examine the relationship between imperfections and shear buckling strength, as the aspect ratio can be related to the web resistant properties for the shear loading condition. The effects of the aspect ratios were compared to the values of each analysis condition for corrosion level and corrosion height. Table 5 and Figure 8 summarize the FE analysis results. In web panels with an aspect ratio of

TABLE 4: Shear buckling resistance of web plate with imperfection at hinge boundary (kN).

Height (mm)	Web corroded condition		Imperfection (initial eccentric deformation)			
	Corroded thickness (mm)	Corroded volume (%)	0	$H/100000$	$H/500$	$H/100$
100	0	0	1160.0	1160.0	1160.0	1140.0
	1	2.08	1140.0	1140.0	1140.0	1120.0
	2	4.17	1120.0	1120.0	1120.0	1110.0
	3	6.25	1080.0	1080.0	1080.0	1060.1
	4	8.33	1039.9	1039.9	1039.9	1020.0
	5	10.42	1020.0	1020.0	1020.0	1000.0
	6	12.50	940.0	940.09	940.0	920.0
200	0	0	1160.0	1160.0	1160.0	1140.0
	1	2.08	1140.0	1140.0	1140.0	1120.0
	2	4.17	1080.0	1080.0	1080.0	1060.1
	3	6.25	1020.0	1020.0	1020.0	1000.0
	4	8.33	959.9	959.9	959.9	940.0
	5	10.42	920.0	920.0	920.0	900.1
	6	12.50	779.9	779.9	779.9	779.9

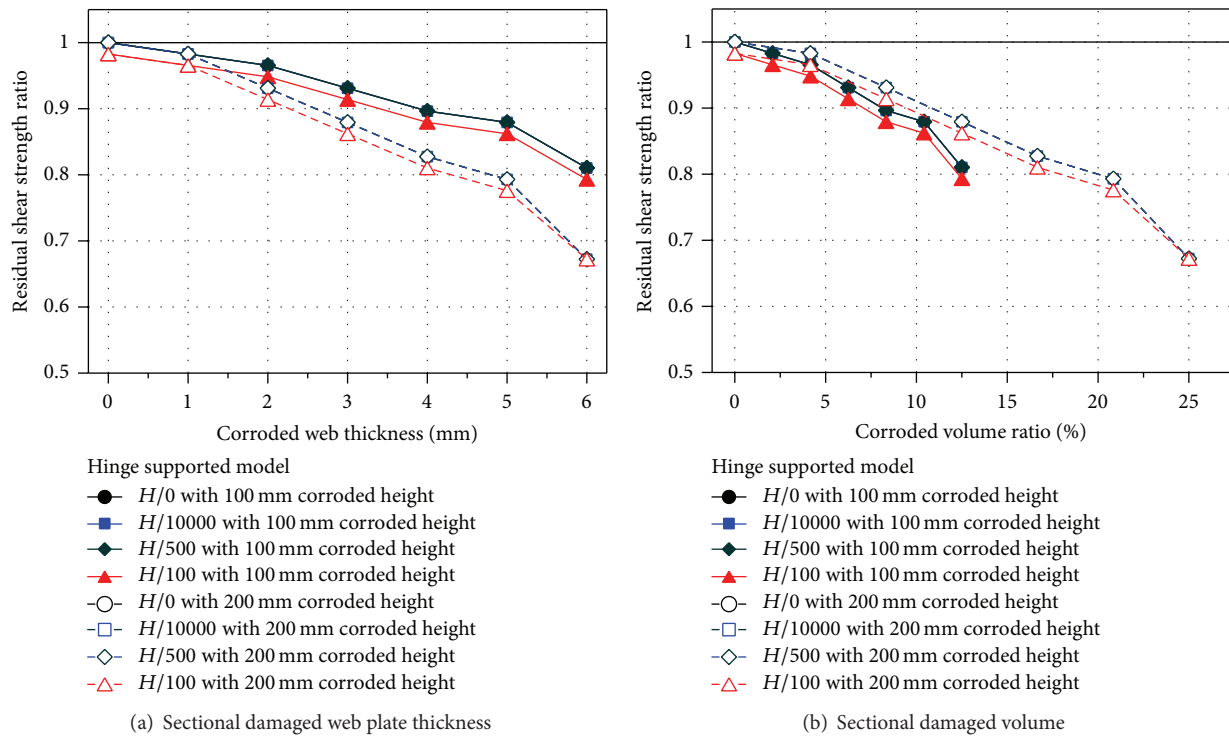


FIGURE 7: Shear buckling resistance ratios with hinge support.

1.0, the shear buckling strength steadily decreased to 79% of the shear buckling strength of web panels without corrosion. For a 1.25 aspect ratio, the strength decreased to 73% of the shear buckling strength of web panels without sectional damage caused by corrosion. For a 1.50 aspect ratio, the strength decreased to 67% of the shear buckling strength of web panels without sectional damage. The changes in the shear buckling strengths presented similar tendencies to the other cases and previous study [4], and they showed a

relatively significantly greater change with a higher aspect ratio web panel. Although their web aspect ratio was changed, the values of the web plate with the $H/100$ eccentric deformation were also affected by approximately 2% compared to those without eccentric deformation, like in the other analysis cases. Therefore, it is thought that the aspect ratio of a web plate is not related to the relationship between imperfection and shear buckling strength of a web panel with corrosion.

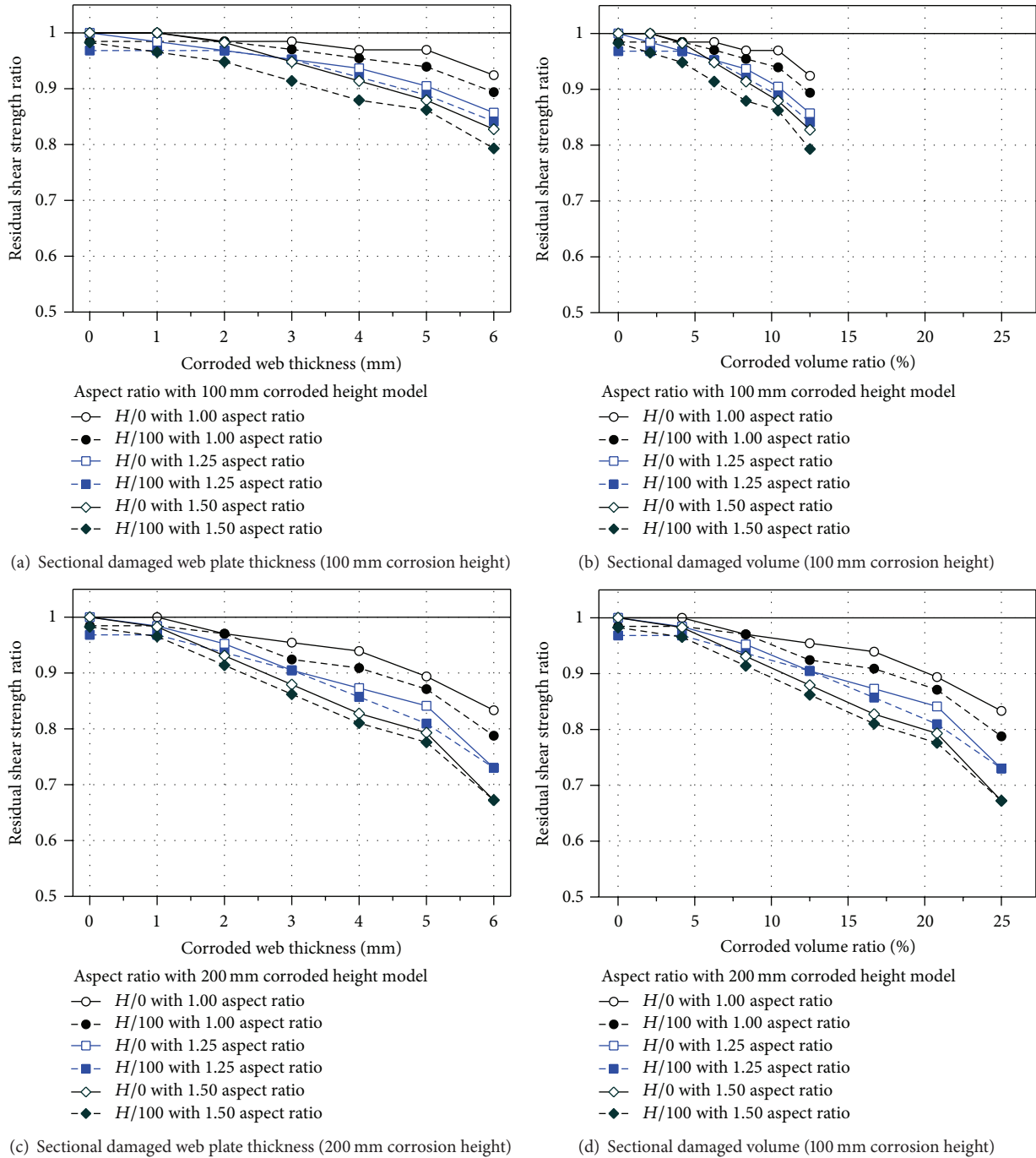


FIGURE 8: Shear buckling resistance ratios depending on aspect ratio.

3.2. Expanded Equation for Shear Buckling Resistance Factor

3.2.1. Expanded Shear Buckling Resistance Factor Equations.

In a web plate with sectional damage caused by corrosion, it is difficult to determine the shear resistant coefficient for calculating the design strength of the web plate according to design specifications since it has local sectional loss caused by corrosion, and its sectional loss is difficult to measure due to its irregular surface. Thus, a simple estimation method is needed to determine the sectional loss of a web plate with

corrosion. In previous studies [4], the change in the shear buckling strength was assessed from a parametric study, and the residual shear resistant equation was suggested based on the corroded volume of the web section, using its reduction factor to easily estimate shear buckling resistance. As mentioned before in this study, it was evaluated that the initial eccentric deformation of a web plate with corrosion has a relatively small effect on the reduced shear buckling performance of the web. Shear buckling strengths of web panels with corrosion were shown to steadily decrease, depending

TABLE 5: Shear buckling resistance of a web plate with imperfection depending on aspect ratio (kN).

Aspect ratio	Web damaged condition			Imperfection (initial eccentric deformation)	
	Height (mm)	Corroded thickness (mm)	Corroded volume (%)	0	$H/100$
1.0	100	0	0	1320.1	1299.9
		1	2.08	1320.1	1299.9
		2	4.17	1299.9	1299.9
		3	6.25	1299.9	1281.0
		4	8.33	1280.0	1260.0
		5	10.42	1280.0	1240.1
		6	12.50	1220.1	1180.0
1.0	200	0	0	1320.1	1299.9
		1	2.08	1320.1	1299.9
		2	4.17	1281.0	1281.0
		3	6.25	1260.0	1220.1
		4	8.33	1240.1	1199.9
		5	10.42	1180.0	1150.0
		6	12.50	1100.0	1039.9
1.25	100	0	0	1260.0	1220.1
		1	2.08	1240.1	1220.1
		2	4.17	1220.1	1220.1
		3	6.25	1199.9	1199.9
		4	8.33	1180.0	1160.0
		5	10.42	1140.1	1119.9
		6	12.50	1080.0	1060.1
1.25	200	0	0	1260.0	1220.1
		1	2.08	1240.1	1220.1
		2	4.17	1199.9	1180.0
		3	6.25	1140.1	1140.1
		4	8.33	1100.0	1080.0
		5	10.42	1060.1	1020.0
		6	12.50	920.0	920.0
1.50	100	0	0	1160.0	1140.0
		1	2.08	1140.0	1120.0
		2	4.17	1120.0	1100.0
		3	6.25	1080.0	1060.1
		4	8.33	1039.9	1020.0
		5	10.42	1020.0	1000.0
		6	12.50	940.0	920.0
1.50	200	0	0	1160.0	1140.0
		1	2.08	1140.0	1120.0
		2	4.17	1080.0	1060.1
		3	6.25	1020.0	1000.0
		4	8.33	959.9	940.0
		5	10.42	920.0	900.1
		6	12.50	779.9	779.9

on web corrosion conditions, regardless of geometrical and boundary conditions. The decreased shear buckling strength tendency could be explained by volume loss caused by corrosion. Thus, FE analysis results were combined with FE analysis results of a previous study to expand the shear buckling resistance factor equation, including the effect of imperfections in a web plate on its shear strength. To expand the shear buckling strength relationship, the web volume ratio (C_v) and the shear strength reduction factor (RS_f) are defined in (1) as in the previous study:

$$C_v = \frac{C_c}{C_s} \tag{1}$$

$$RS_f = \frac{U_c}{U_s},$$

where C_s is the total volume of the web, C_c is the sectional damage volume of the web plate, U_s is the shear buckling strength of the web without sectional damage, and U_c is the shear buckling strength of the web with sectional damage caused by corrosion.

From the FE analyses of a web plate without an initial eccentric deformation, its shear buckling reduction factor equation was derived as (2), using the damaged web volume ratio (sectional damaged volume ratio, C_v). From the FE analysis data in this study, the shear buckling reduction factor equation was suggested as (3). Equation (3), derived by the FE analysis results with an initial eccentric deformation, shows a slightly different distributed shape compared to the distributions of the FE analysis results of the previous study. However, some FE analysis data of the previous study showed some differences when compared to (3) derived from the FE analysis data of this study. In addition, almost all of the FE analysis results with an initial eccentric deformation were within the 95% prediction band derived from the regression curve in the previous study as the initial eccentric deformation effect on the shear buckling strength is not high. As shown in Figure 9, in the case of low sectional damage caused from corrosion, the variation of the reduction in the shear buckling resistance had little effect on the sectional damage. In the case of higher sectional damage caused from corrosion, however, its variation in the same corrosion was greatly apparent. If corrosion volume was used as a performance parameter and not a structural sectional parameter, as in this study and the previous study, it could be necessary to evaluate more conservatively by including various damage conditions and imperfections. In the case of the lower boundary, its 95% prediction band, derived in the previous study using (4), was satisfied conservatively, except for some results. Therefore, (4) can be used to conservatively evaluate the shear buckling reduction factor of a web plate with corrosion when unable to estimate the exact section damage caused by corrosion:

$$RS_f = 0.7368 + \frac{0.2859}{1 + e^{-((C_v - 8.8318)/-3.4666)}} \tag{2}$$

$$RS_f = -0.5806 + \frac{1.8005}{1 + e^{-((C_v - 47.4707)/-24.1883)}} \tag{3}$$

$$RS_f = 0.6246 + \frac{0.2997}{1 + e^{-((C_v - 8.9931)/-3.6791)}} \tag{4}$$

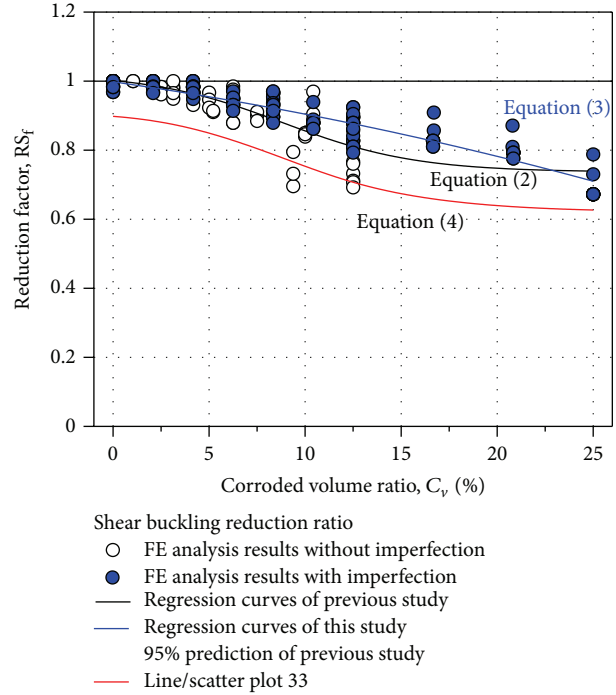


FIGURE 9: Shear buckling reduction factor equation.

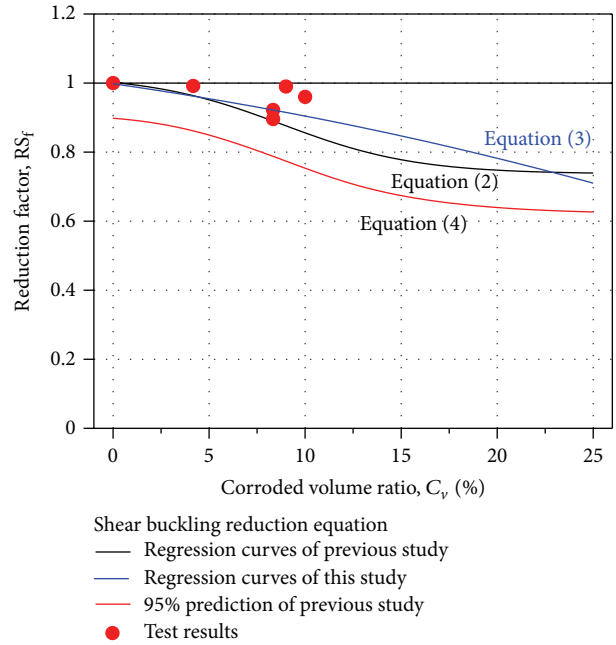


FIGURE 10: Comparison of test results with suggested shear buckling equation.

3.2.2. Example for Calculation of Shear Buckling Resistance of a Web Plate with Sectional Damage. To verify the expanded shear buckling reduction factor for maintenance and inspection of web panels, the sectional damage of the web plate used in shear loading tests was calculated and compared to the suggested shear buckling resistance equations [3, 12]. Figure 10 shows the comparison between the suggested shear

buckling resistance equations and the test results. As shown in the figure, the test results are similar to (2) and (3) for relatively little sectional damage of the web plate. For shear loading tests, sectional damage was exactly calculated; thus, the shear buckling strengths were very similar to the values calculated using (2) and (3). However, it is difficult to calculate exact sectional damage caused by corrosion in the field. Therefore, (4) can be used to conservatively estimate the shear buckling strength for a web plate when the exact amount of sectional loss due to corrosion is unknown, such as in the field.

4. Conclusions

This study carried out a series of a nonlinear finite element (FE) analyses of a web plate pane to examine the relationship between imperfections and shear buckling resistance of a web plate with sectional damage caused by corrosion. To examine the imperfection effect on the shear buckling resistance of a web plate with sectional damage, an initial out-of-plane deformation was considered as a main parameter, and the shear buckling resistance of the sectional damaged web plate was examined based on aspect ratio, boundary condition, and the sectional damaged height of the web plate from the lower flange.

The shear buckling resistance of a sectional damaged web panel with $H/100,000$ and $H/500$ imperfections was shown to be similar to that of a web plate without imperfections. However, for web panels with an $H/100$ imperfection, their shear resistance values decreased to approximately 2% of those of the web plate without sectional damage. In terms of sectional web damage thickness, the shear resistance values decreased according to the sectional damage web height from the lower flange, but they were also shown to significantly decrease in the web panel that had a lower sectional damage web height compared to the sectional damage volume ratio. For the sectional damaged web plate with different aspect ratios, their resistance to change exhibited a similar tendency, and it markedly changed in the higher aspect ratio web. The equation for shear buckling resistance of a web plate with sectional damage was modified based on a comparison of the previous study results for use in the practical maintenance of corrosion damaged web plates.

Competing Interests

The authors declare that there is no conflict of interests regarding the publication of this paper.

Acknowledgments

This research was supported by Development of Hybrid Substructure System for Offshore Wind Farm, Project no. 20123010020110 funded by the Ministry of Trade, Industry and Energy, Korea.

References

- [1] J. R. Kayser and A. S. Nowak, "Reliability of corroded steel girder bridges," *Structural Safety*, vol. 6, no. 1, pp. 53–63, 1989.
- [2] J.-H. Ahn, S. Kainuma, F. Yasuo, and I. Takehiro, "Repair method and residual bearing strength evaluation of a locally corroded plate girder at support," *Engineering Failure Analysis*, vol. 33, pp. 398–418, 2013.
- [3] I.-T. Kim, M.-J. Lee, J.-H. Ahn, and S. Kainuma, "Experimental evaluation of shear buckling behaviors and strength of locally corroded web," *Journal of Constructional Steel Research*, vol. 83, pp. 75–89, 2013.
- [4] J.-H. Ahn, I.-T. Kim, S. Kainuma, and M.-J. Lee, "Residual shear strength of steel plate girder due to web local corrosion," *Journal of Constructional Steel Research*, vol. 89, pp. 198–212, 2013.
- [5] J.-H. Ahn, S. Kainuma, and I.-T. Kim, "Shear failure behaviors of a web panel with local corrosion depending on web boundary conditions," *Thin-Walled Structures*, vol. 73, pp. 302–317, 2013.
- [6] J. K. Paik, J. M. Lee, and M. J. Ko, "Ultimate shear strength of plate elements with pit corrosion wastage," *Thin-Walled Structures*, vol. 42, no. 8, pp. 1161–1176, 2004.
- [7] D. Ok, Y. Pu, and A. Incecik, "Computation of ultimate strength of locally corroded unstiffened plates under uniaxial compression," *Marine Structures*, vol. 20, no. 1-2, pp. 100–114, 2007.
- [8] J. E. Silva, Y. Garbatov, and C. Guedes Soares, "Ultimate strength assessment of rectangular steel plates subjected to a random localised corrosion degradation," *Engineering Structures*, vol. 52, pp. 295–305, 2013.
- [9] J. Huh, I.-T. Kim, and J.-H. Ahn, "Locally corroded stiffener effect on shear buckling behaviors of web panel in the plate girder," *Advances in Materials Science and Engineering*, vol. 2015, Article ID 586264, 19 pages, 2015.
- [10] National Institute for Land and Infrastructure Management, "Research on local corrosion of highway steel bridges," Technical Note 294, National Institute for Land and Infrastructure Management, 2006 (Japanese).
- [11] J. Murakoshi and Y. Tanaka, "Research on retrofitting for corroded steel girder around expansion joint," Civil Engineering Research Reports, CAESAR, 2008.
- [12] J.-H. Ahn, J.-H. Cheung, W.-H. Lee, H. Oh, and I.-T. Kim, "Shear buckling experiments of web panel with pitting and through-thickness corrosion damage," *Journal of Constructional Steel Research*, vol. 115, pp. 290–302, 2015.
- [13] T. E. Dunbar, N. Pegg, F. Taheri, and L. Jiang, "A computational investigation of the effects of localized corrosion on plates and stiffened panels," *Marine Structures*, vol. 17, no. 5, pp. 385–402, 2004.
- [14] M. F. Hassanein, "Imperfection analysis of austenitic stainless steel plate girders failing by shear," *Engineering Structures*, vol. 32, no. 3, pp. 704–713, 2010.
- [15] AASHTO/AWS, "Bridge welding code," Tech. Rep. ANSI/AASHTO/AWS D1.5M/D1.5:2002, A Joint Publication of American Association of State Highway and Transportation Officials, Washington, DC, USA; American Welding Society, Miami, Fla, USA, 2002.
- [16] Marc 2012 User's Guide, MSC Software Corporation, 2012.

Research Article

Experimental and Analytical Investigation Based on 1/2 Scale Model for a Cleanroom Unit Module Consisting of Steel Section and Reinforced Concrete

Sijun Kim¹ and Se Woon Choi²

¹Department of Plant Architectural Engineering, Kyonggi University, Suwon, Kyonggido 16227, Republic of Korea

²Department of Architecture, Catholic University of Daegu, Kyeongsan-si, Kyeongbuk 38430, Republic of Korea

Correspondence should be addressed to Se Woon Choi; watercloud@cu.ac.kr

Received 20 May 2016; Revised 21 June 2016; Accepted 23 June 2016

Academic Editor: Gilson R. Lomboy

Copyright © 2016 S. Kim and S. W. Choi. This is an open access article distributed under the Creative Commons Attribution License, which permits unrestricted use, distribution, and reproduction in any medium, provided the original work is properly cited.

The rapid advances in high tech industries and the increased demand for high precision and reliability of their production environments call for larger structures and higher vertical vibration performance for high technology facilities. Therefore, there is an urgent demand for structural design and vertical vibration evaluation technologies for high tech facility structures. For estimating the microvibration performance for a cleanroom unit module in high technology facilities, this study performs the scale modeling experiment and analytical validation. First, the 1/2 scale model (width 7500 mm, depth 7500 mm, and height 7250 mm) for a cleanroom unit module is manufactured based on a mass-based similitude law which does not require additional mass. The dynamic test using an impact hammer is conducted to obtain the transfer function of 1/2 scale model. The transfer function derived from the test is compared with the analytical results to calibrate the analytical model. It is found that, unlike for static analyses, the stiffness of embedded reinforcement must be considered for estimating microvibration responses. Finally, the similitude law used in this study is validated by comparing the full-scale analytical model and 1/2 scale analytical model for a cleanroom unit module.

1. Introduction

Advances in information communication technology and production technology in recent years have increasingly sophisticated high technology products, such as semiconductors, liquid crystal displays (LCD), and optical microscopes. Demands for these products are predicted to rise further as they make our lives more convenient.

Semiconductors, LCD, and optical microscopes require high precision, and thus their production equipment and facilities must satisfy stringent terms. Vertical vibration that occurred must be strictly controlled because vertical vibration exposure during production increases production error and results in defects. Therefore, manufacturers of the production equipment conduct vibration tests and disclose vibration specifications for their equipment [1].

Vibration performances provided by manufacturers are based on vibration testing in an environment controlled for vibration, temperature, and humidity. Therefore, to exhibit

the vibration performance of a piece of equipment, an environment with extremely limited vibrations is required. However, it is difficult to satisfy such stringent conditions in regular production environments. A variety of vibration sources (e.g., traffic, personnel activities, and motion of motor in equipment) are present in high technology facilities that produce vibration-sensitive products, and resulting vibrations are transferred to the high technology equipment via the structures consisting of the facility (e.g., columns, beams, and floor plates), ultimately undermining the precision of the production process. Hence, strict management of vibration performance of structures consisting of high technology facilities as well as high technology equipment is demanded.

The vibration performance of structures is evaluated using generic vibration design criteria, rather than specific criteria for each piece of equipment [2–6]. The criteria take the form of a set of one-third-octave band velocity spectra labeled vibration criterion curves VC-A through

VC-E and are known as the BBN Criterion Curves [4]. These curves have been used for evaluations of microvibration performance of various structures within high technology facilities [7–10].

For general structures, the structural design strategy that the structures are more flexible so as to buffer the shocks of lateral loads such as earthquakes is employed [11–13]. This is because a flexible structure has a lower risk for resonance, which would reduce vibration resonance. However, this is not the solution for microvibration of high technology facility structures. These structures cannot be simply designed to be flexible because the types and frequencies of vibrations that affect the floor—upon which high technology equipment is installed—are diverse. Furthermore, while specific vibration frequencies or regions are dominant in general buildings, those are not dominant in the floor structural systems. For these reasons, it is difficult to avoid the resonance frequency through designing floor structures flexibly.

Thus, the problems of microvibration in the high technology facility structures are addressed by maximizing the stiffness of the structures to prevent resonance below a certain vibration frequency [14]. It is necessary that stiffness of the structures be increased because the high accuracy equipment generally is more sensitive to low frequencies. The primary natural frequency of vertical vibrations in the floor structures of general office buildings ranges from 5 to 10 Hz while that of structures within high technology facilities ranges from 10 to 20 Hz.

Microvibration performance in the high technology facility structure is affected by the size and arrangement of structural members, story height, and span length, so these should be taken into consideration during the design process [14–17]. Despite such significance, research literatures on the structural design and microvibration performance evaluation of the high technology facility structure have been relatively limited. One reason is that design data for high technology facility are generally not open to the public.

Furthermore, experimental data and structural analysis modeling techniques are required to develop structure design and performance evaluation technologies. However, high technology facility structures are bound to be large-scale in terms of story height, span length, and cross-sectional size of members compared to those of general buildings because of production and environmental equipment as well as vibration performance requirements. The problems of costs and space induced by such large sizes have crippled research efforts on experimental evaluations and structural analysis modeling of high technology facility structures. However, the rapid advances in high tech industries and the increased demand for high precision and reliability of their production environments call for larger structures and higher vibration performance for high technology facilities. Therefore, there is an urgent demand for structural design and vibration evaluation technologies for high tech facility structures, which in turn call for more vigorous experimental and analytical studies on this matter.

Studies in various aspects of high tech facility structures are required. But most of all, we must verify the vibration

performances of these facilities as designed with conventional techniques. Performance evaluations for vibration should be conducted at the building level because a variety of building members and conditions affect vibration performance. By and large, a vibration analysis is performed to evaluate vibration response to be reflected on the design of high tech plants that require stringent management of microvibration. However, the theoretical and practical limitations of structural analysis technology generate a gap between the actual vibration and the computed vibration of the structure. Therefore, more experimental studies are required to develop and improve structural design techniques for high tech facility structures.

Experimenting with the full-scale structures would produce the most accurate results with regard to the vibration properties of a specific structure, but such experiments are practically impossible due to spatial limitations as well as cost and time inefficiency. Therefore, scale models are usually manufactured for experiments. Existing studies using scale models mostly focused on the evaluation of seismic performance or wind performance of structures [18–23], and experimental studies to evaluate the microvibration performance of high tech facility structures have rarely been reported.

This study seeks to conduct an experiment to analyze the differences in the actual and analytical measurements so as to develop data for future references for designing microvibration control in high tech facility structures. To this end, we manufactured the 1/2 scale model according to the mass-based scaling method. It is quite difficult to predict the performance of the actual structure by experimenting with a scale model. Hence, the existing scale model studies employ the similitude law, which defines the scale effects in physical terms. However, scaling down a structure is associated with a variety of variables, and some factors cannot be quantitatively scaled down. In other words, it is impossible to apply an identical similitude for all variables. Hence, an appropriate scaling method should be selected to meet specific experimental objectives and conditions. This study selects the mass-based scaling method for microvibration evaluation of high tech facility structures by analyzing the general scaling methods (i.e., mass-based, time-based, and acceleration-based). The mass-based scaling method does not require additional masses. The others require additional masses where it is difficult to conduct the scale model experiment of high tech facility structures.

The dynamic experimental test using an impact hammer is performed on the scaled-down model, and the transfer function is found based on this data. Transfer functions include the dynamic characteristic information for higher-order modes (e.g., 1st, 2nd, and 3rd) and thus are the most popular index in identifying structural properties [24]. In the present study, the transfer function acquired from the experiment is used as a comparative index to validate the analytical modeling technique. It is known that nonstructural components such as partition walls, infilled walls, external walls, and elevator shafts as well as the structural components affect the stiffness and frequencies of buildings [25, 26]. These effects should be considered to obtain the simulation model

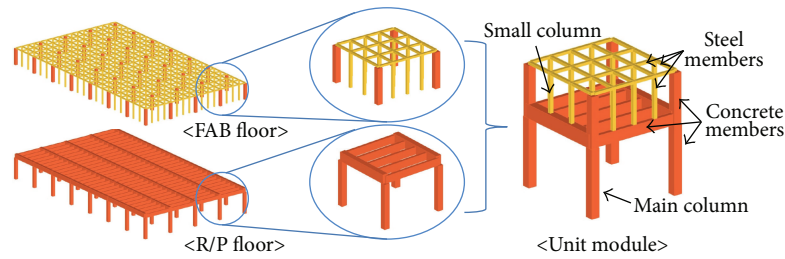


FIGURE 1: The example of the unit module consisting of high tech facility structures.

that shows the good agreement with the behaviors of real structures.

A small-scale model must be able to generate results that reliably mock the prototype's behaviors. To validate these results, a full-scale model in addition to the small-scale model must be manufactured to compare and analyze the results with identical experimental methods. In particular, because the scale model used in this study is a complex structure comprising steel members and reinforced concrete (RC) members, the similitude of the scale model must be validated. However, manufacturing a full-scale model of high tech facility structures is realistically impossible as their long span lengths and high story heights require considerable costs, large spaces, and risky experiments. Therefore, we additionally perform an analytical modeling for the prototype using an analytical modeling technique verified via the 1/2 scale model experiment. To validate the similitude law used in this study, the analytic results obtained from both the scale model and prototype are compared.

2. Cleanroom in High Tech Facility Structures

Industrial facilities that produce high-precision products, such as semiconductors, LCD, and optical microscopes, are equipped with a space called a cleanroom [27–29]. A cleanroom is an environmentally controlled space in which contaminants such as airborne dusts or hazardous gases are regulated to meet stringent standards.

Cleanrooms require air conditioning equipment to maintain a clean air environment. Airflow within a cleanroom can be divided into vertical laminar airflow, horizontal laminar airflow, and turbulent airflow. Despite high initial costs and maintenance fees, vertical laminar airflow is the mostly widely used type because it can maintain a highly clean environment with minimal influence from personnel.

As shown in Figure 1, vertical laminar airflow is arranged such that a unit module comprising a fabrication (FAB) level and return plenum (R/P) level is continuously repeated. Production equipment is installed on the FAB level and the R/P level refers to the space in the lower section of FAB level to circulate air injected from the ceiling of the FAB level. Supply/exhaust duct, cable, and pipe are installed on the R/P level. The FAB level must meet stringent vibration specifications as high technology production activities are performed at this level. Therefore, the FAB level must be highly stiff, which is achieved by densely positioning small columns between the FAB and R/P levels. The main columns that support the

FAB level are relatively widely spread. Small columns are only built in the lower sections of the FAB level and do not interfere with equipment arrangement; however, the main columns limit the arrangement of production equipment. It is critical to quickly construct plants for productions in the high technology industry owing to rapid technological advances and fierce competition. Therefore, to reduce the construction period of cleanrooms, the floor of the FAB level and small columns are built with steel frames while the floor of the R/P level and main columns are built with reinforced concrete.

The requirements with regard to cleanliness of air and environmental conditions have become more stringent with increased precision of production facilities and measurement equipment. This has led to larger production equipment, air conditioning units, and ducts, which in turn caused the span lengths and story heights to increase. However, the vibration performance of structures generally is weakened as the span lengths and story heights of structures increases. To design and construct the larger high tech facility structures while satisfying the stringent vibration performance condition, it is necessary to develop and improve the experimental and analytic techniques for those.

3. Similitude Law

3.1. Overview. The similitude law is a rule for determining the desired physical measurements for an experiment based on dimensional analysis and defines the scale effects of a prototype in physical ratios. For general dynamic problems, length (L), mass (M), and time (T) are set as the basic dimensions, and the other parameters are determined based on a combination of the basic dimensions. For example, if the similitude for a prototype and small-scale model is defined as “ S ,” then the similitude relationship between the two structures is induced as shown in Table 1. Table 1 categorizes the similitudes based on acceleration, mass, and time, which signifies that all of the parameters cannot be appropriately scaled at once. For instance, if the similitude is S , the basic scale for length would be S . If the similitude for time cannot be adjusted or time (or frequency) effect should be equal in both the scale model and prototype, the similitude for time must be 1. Then, the similitude for acceleration, which incorporates both length and time as per LT^{-2} , becomes S . However, if the experiment is influenced by the acceleration of gravity, this rule cannot be applied as the acceleration of gravity cannot be manipulated.

TABLE 1: Scale factor according to the parameters.

Parameter	Range	Scale factor		
		Mass-based	Time-based	Acceleration-based
Length	L	S	S	S
Mass	M	S^3	S	S^2
Time	T	S	1	$S^{0.5}$
Stress	$ML^{-1}T^{-2}$	1	1	1
Velocity	LT^{-1}	1	S	$S^{0.5}$
Acceleration	LT^{-2}	1/S	S	1
Force	MLT^{-2}	S^2	S^2	S^2
Stiffness	MT^{-2}	S	S	S
Damping	MT^{-1}	S^2	S	$S^{3/4}$
Natural frequency	T^{-1}	1/S	1	1/S ^{0.5}

(i) *Acceleration-Based Scaling.* The acceleration ratio should be defined as 1 in order to accurately represent the gravity and inertia of a structure because even though the acceleration on a mass can be controlled, the acceleration of gravity cannot be manipulated. In this case, the similitudes for mass and time are proportional to S^2 and $S^{0.5}$, respectively, and added mass and time compression are required to conduct a dynamic test.

(ii) *Time-Based Scaling.* Time ratio can be set to 1 when the influence of gravity can be ignored. Then the frequency effect would be conserved for the prototype and scale model, which allows the researcher to acquire quantitative information about the internal performance of a structure. In this case, mass is proportional to S , so added mass is required for a dynamic test.

(iii) *Mass-Based Scaling.* When the influence of gravity cannot be ignored, the mass can be adjusted to be proportional to S^3 . In this case, this ratio is applied to the scale model for the dynamic testing. However, researchers must take note that time is proportional to S .

3.2. *Selection of Scaling Method for Similitude of High Tech Facility Structures.* Each of the three types of similitude explained above has distinct properties, so researchers should select whichever is more appropriate for their research objective. If acceleration-based scaling is chosen, the similitude for mass becomes S^2 . The similitude for length is S and the mass of the scale model is reduced by S^3 , in which case an additional mass ($S^2 - S^3$) should be added to the model. For example, if the similitude is $S = 1/2$ as used in this study, each member is scaled down by $1/2$, and the mass ratio for the small-scale becomes $(1/2)^3$. However, the mass ratio as per the similitude must be $(1/2)^2$, which means that we need to add a mass equal to $1/8$ ($= 1/4 - 1/8$) of the prototype. This means that we need an added mass equal to the scale model. Because the high tech facility structures are generally large, $1/2$ scale model of it is heavy and has the long span length and high story height. Thus, the added mass makes it difficult to set up and conduct the experimental test for high tech facility structures.

If time-based scaling method is chosen because the frequency effect is considered as the most important variable, the similitude for mass becomes S . This signifies that the size of the added mass becomes $(S - S^3)$, which is a larger value than that required for the acceleration-based scaling ($S^2 - S^3$).

In the present study, $S = 1/2$ is chosen. Therefore, we must add a mass greater than the scale model itself when we choose acceleration-based or time-based scaling method. On the other hand, if we choose the mass-based scaling method, the similitude for mass becomes S^3 . This would be automatically satisfied if we apply a similitude of S to the member measurements, so added mass would not be required. For this reason, the present study uses the mass-based scaling method.

4. Experimental Test

4.1. *One-Half-Scale Model.* We manufacture a $1/2$ scale model for the unit modules of the cleanroom as shown in Figure 2. The width, depth, and height for the model are 7.20 m, 7.20 m, and 7.25 m, respectively. The FAB level and the small columns are arranged in an H-shape, and the R/P level and the main columns are constructed with concrete. The members for the steel H-shape should be manufactured by applying the similitude as steel is a homogenous material, but the members in the scale model are very thin, which would induce deformation when welded and would undermine constructability. Therefore, we chose rolled shape as a similar alternative. The strengths and section sizes of the materials used are shown in Table 2.

For the scale model design, when reducing the member sizes according to the scale factor (S), the axial loads and moments of the section designs for the two structures have to be matched with the scale factor. Moreover, when the properties of the materials used are different, the strains of the concrete and steel frame have to be considered. In this study, since the same materials are used, the strains are not considered and the amounts of reinforcements are planned by applying the scale factor (S^3) for the moment only, while neglecting the scale regarding the axial load effect, which has the smallest impact on the dynamic behavior of the structure.

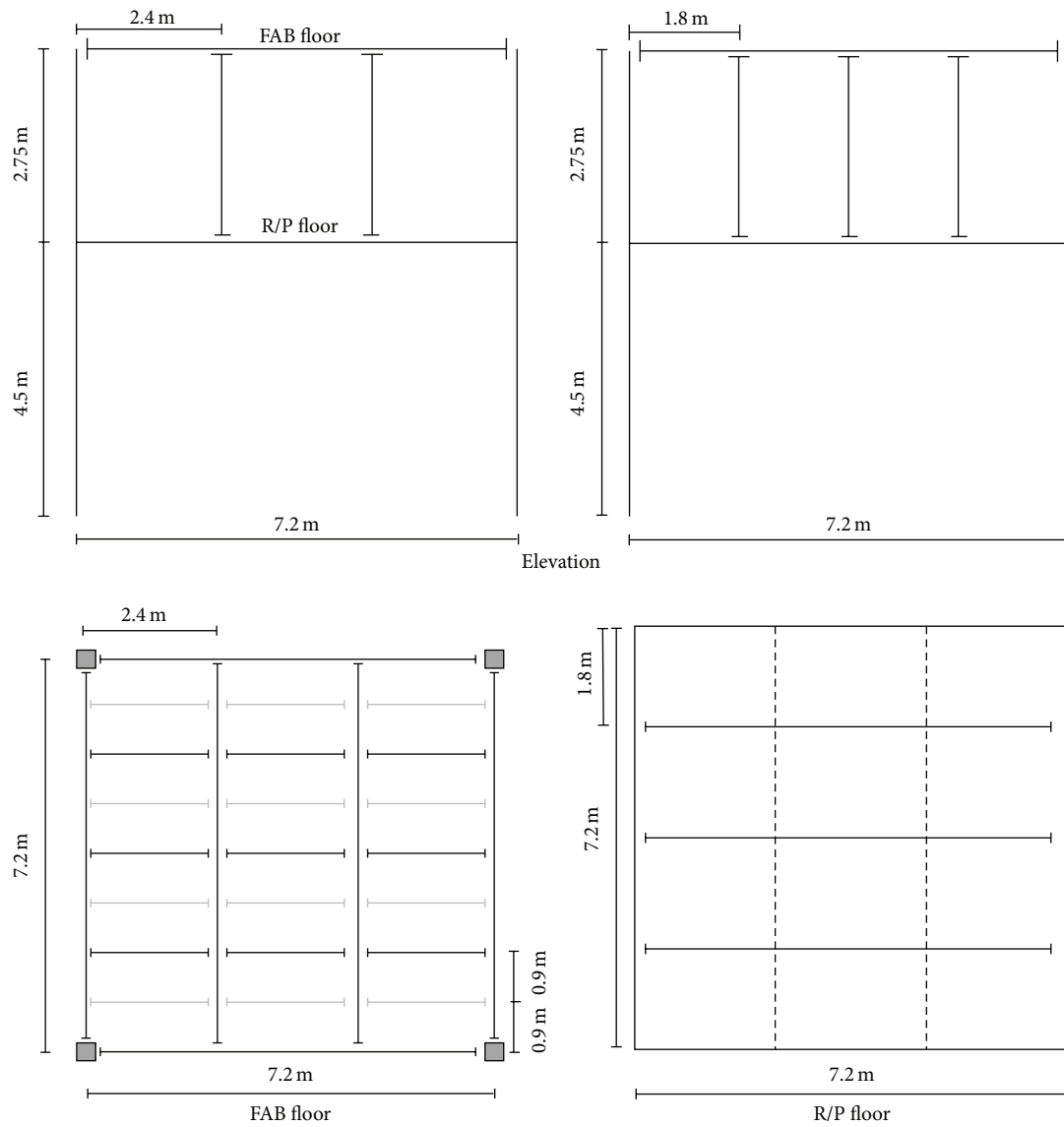


FIGURE 2: 1/2 scale model manufactured by using mass-based scaling method.

TABLE 2: Specifications of prototype model and 1/2 scale model.

Category	Prototype model	1/2 scale model
Member dimensions (unit: mm)		
R/P floor beams	800 × 1200	400 × 600
	700 × 1200	350 × 600
	1400 × 1600	700 × 800
Main column	1000 × 1000	500 × 500
FAB floor beam	H-440 × 300 × 11 × 18	H-220 × 150 × 6 × 9
Small column	H-300 × 300 × 15 × 10	H-150 × 150 × 7 × 10
Slab	Thk. = 180	Thk. = 90
Span	14400 mm × 14400 mm	7200 mm × 7200 mm
Story heights	First floor: 9000 mm	First floor: 4500 mm
	Second floor: 5500 mm	Second floor: 2750 mm
Damping ratio	3%	3%
Material strengths	27 MPa concrete	27 MPa concrete
	500 MPa rebar	500 MPa rebar
	400 MPa section steel	400 MPa section steel

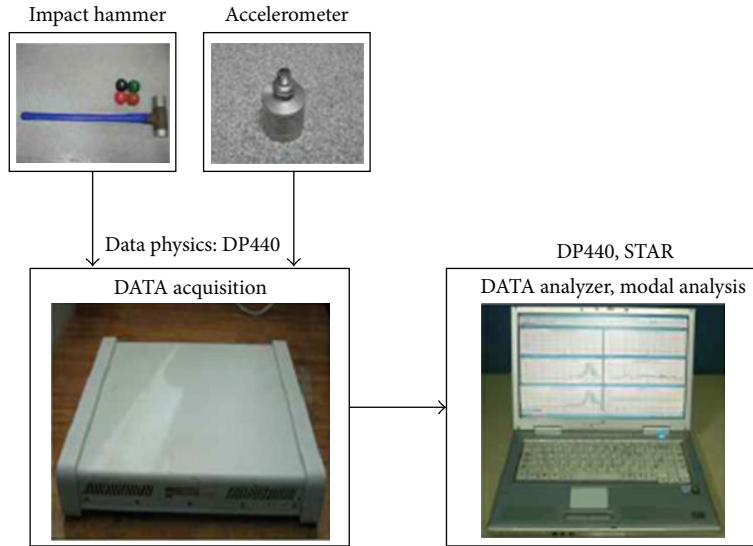


FIGURE 3: Equipment component used for the impact hammer test.

4.2. Impact Hammer Test. We perform an impact hammer test on the scale model to acquire data required for the validation of the analytical modeling technique. The objective of the impact hammer experiment in this study is to derive a transfer function for the prototype. To this end, impact hammer experiment is performed using the equipment shown in Figure 3. First, we strike the structure with the impact hammer to induce vibration. The exciting force $f(t)$ and response $x(t)$ from the structure are measured by the sensor on the impact hammer and accelerometer installed on the structure, respectively. The collected data is analyzed via the data analyzer. The exciting force $f(t)$ and response $x(t)$ are functions of time but can be converted into functions of frequency using the Fourier transform. The transformed response $X(\omega)$ and exciting force $F(\omega)$ are used to derive a transfer function $H(\omega)$ as shown in (1). A transfer function is a unique property of a structure that represents the size of

response for a unit exciting force. Hence, it is an appropriate comparative index for the evaluation of the accuracy of modeling by the analytical modeling technique:

$$H(\omega) = \frac{X(\omega)}{F(\omega)}. \quad (1)$$

5. Analytical Validation

5.1. Comparison of Transfer Functions Using Data from Scale Model Experiment. We produce an analytical model for the 1/2 scale model as shown in Figure 4. In the analytical model, the sizes of the members are determined by the design values shown in Table 2. The modulus of elasticity for concrete is set to the standard value based on the concrete strength. Although the damping value should vary depending on the mode, a uniform value is used for the analysis because it

TABLE 3: Rebar ratios of beam members.

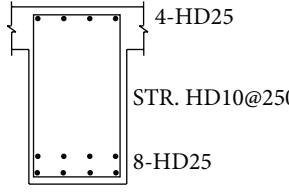
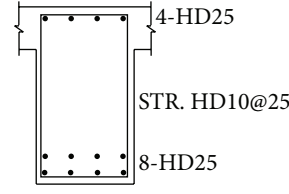
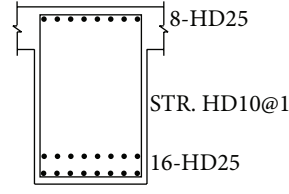
Type of beams	400 × 600	350 × 600	700 × 800
Section	 <p>4-HD25 STR. HD10@250 8-HD25</p>	 <p>4-HD25 STR. HD10@250 8-HD25</p>	 <p>8-HD25 STR. HD10@150 16-HD25</p>
Rebar ratios	0.0253	0.0290	0.0217

TABLE 4: Comparison of the simulated and measured frequencies.

Mode	Frequencies by an experimental test (Hz)	Frequencies simulated without the consideration for the stiffness of rebars		Frequencies simulated with the consideration for the stiffness of rebars	
		(Hz)	Error rate (%)	(Hz)	Error rate (%)
1st	16.25	13.90	16.91	16.11	0.87
2nd	27.75	33.80	17.90	27.34	1.50
3rd	30.50	39.50	22.78	31.25	2.40

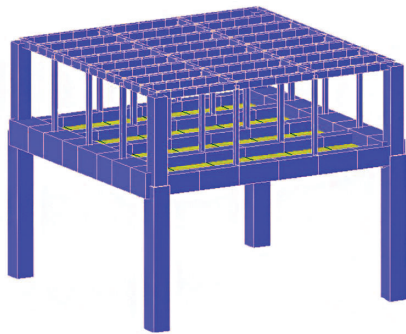
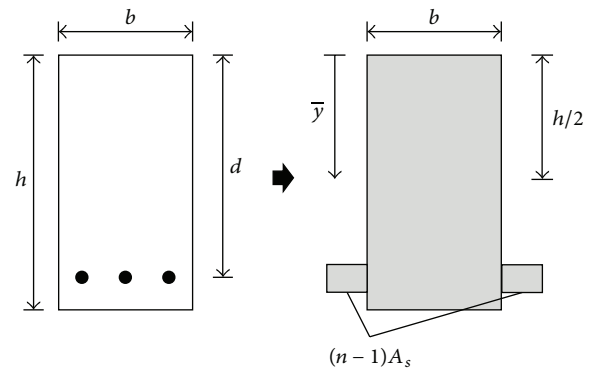


FIGURE 4: Perspective view of the analytical model.



n is the ratio of reinforcements to concrete
 A_s is the total cross-sectional area of reinforcements

FIGURE 5: The transformed area concept.

requires a damping value for frequencies that cannot be empirically calculated.

The simulation indicates about 20% error for natural frequency compared to the results of the experiment. To reduce this error, we examined the potential effects of various parameters and input values and found that considering the effect of reinforcement embedded in concrete would reduce error the most. In general, safety evaluations using static analysis of reinforced concrete structures can assume that the members of a structure are constructed purely with concrete without considering the effects of embedded reinforcement because the stiffness ratio for the members is more important. However, it is shown that analysis of microvibrations should consider the effects of reinforcement because the stiffness of each member has a considerable impact on the structure's dynamic behavior.

Therefore, we considered the effects of embedded reinforcement during our modeling of the concrete members. To this end, we applied the transformed area concept, in which

the cross-sectional area of the steel is transformed into that of concrete with equivalent axial stiffness as shown in Figure 5. Applying this concept to beam members with rebar ratios in Table 3 produced similar results with the experiment as shown in Figure 6. It is confirmed that two transfer functions from the experiment and numerical analysis show the good agreement.

Figure 7 and Table 4 show the mode shapes and frequencies of the experimental and analytic models. It is shown that the difference errors of the first, second, and third frequencies obtained from the simulated model with the consideration for the stiffness of rebars are reduced from 16.91%, 17.90%, and 22.78% to 0.87%, 1.50%, and 2.40%, respectively.

The size of a mesh in finite element analysis influences the accuracy [30, 31]. It is necessary to check whether the

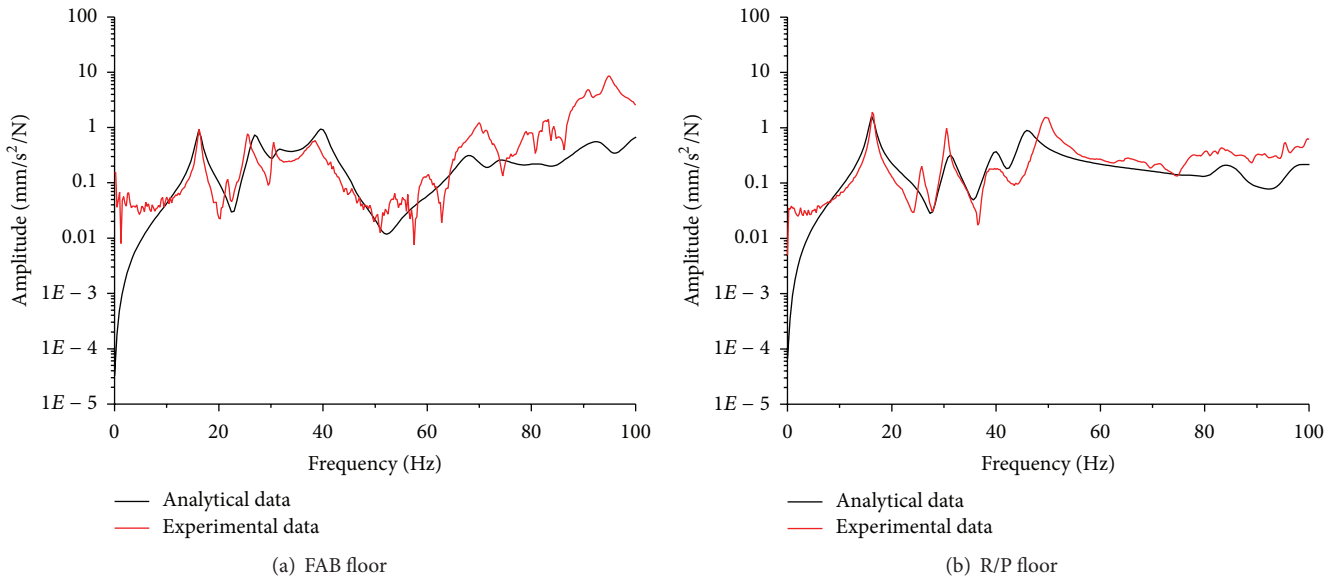


FIGURE 6: Comparisons of transfer functions from the experiment and numerical analysis.

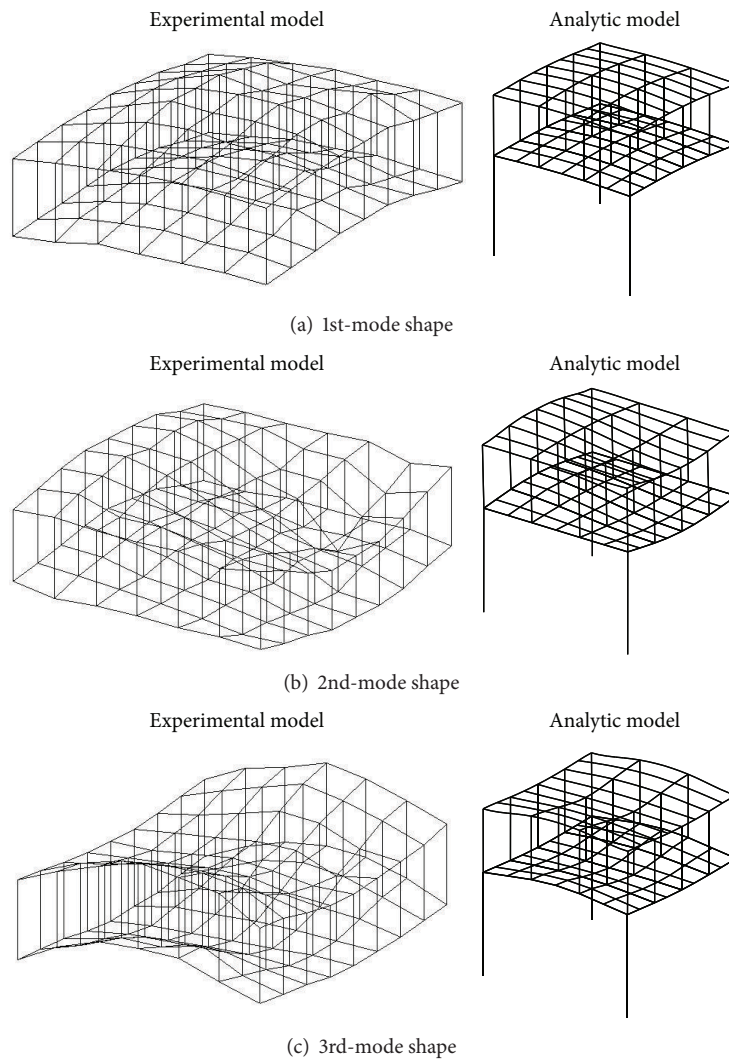


FIGURE 7: Comparison of the mode shapes obtained from the experimental and analytic models.

TABLE 5: Comparison of natural frequencies from the prototype model and 1/2 scale model.

Mode	1/2 scale model	Prototype model	Ratio of response amplitude
1st	13.9	6.9	2.01
2nd	33.8	16.9	2
3rd	39.5	19.7	2
4th	78.5	39.7	1.97
5th	97.4	48.7	2

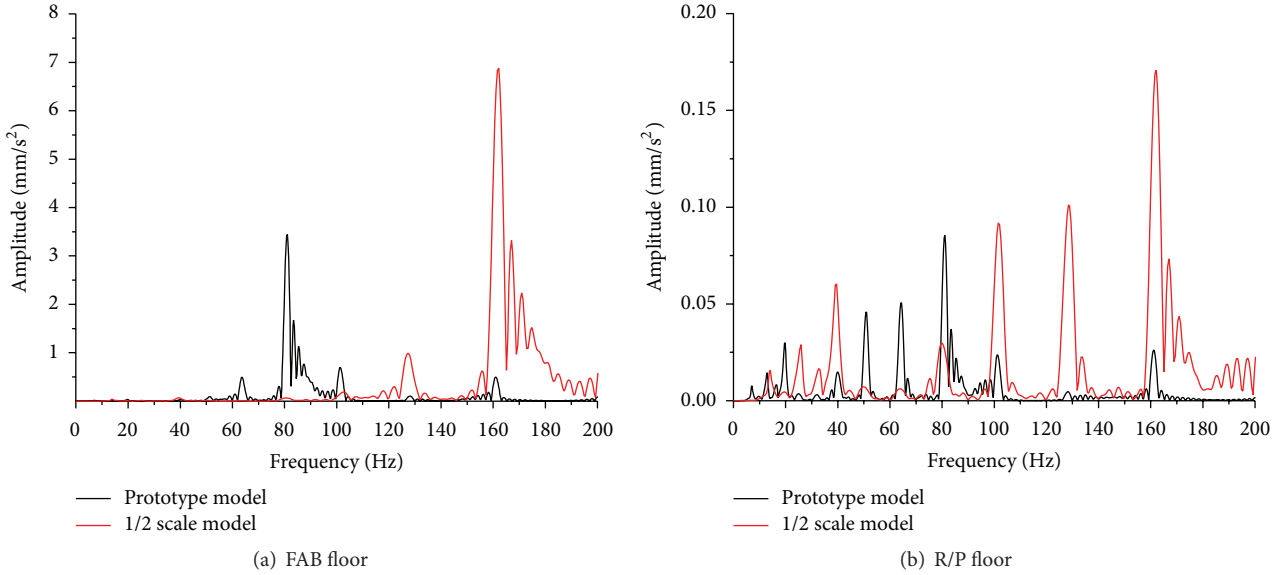


FIGURE 8: Comparisons of response results from the prototype model and 1/2 scale model.

size of a mesh is appropriate. The fine mesh is employed to investigate the local behaviors or the higher mode effects of a structure. Otherwise, it is known that when global response is of primary interest, the coarse-mesh model is attractive [32]. Because the mass participation factor of low-rise buildings for the first mode is generally more than 90%, the coarse-mesh model can be considered for the vibration analysis of low-rise buildings. It was shown that the mass participation factor of the first mode for the target structure used in this study was 99.45% and the difference between the first natural frequencies from the experimental and simulated results in Table 4 was 0.87%. Because the acceptable error rate was obtained, there was no necessity to modify the size of mesh employed in this study. If it is necessary to improve the accuracy of vibration analysis, the effects of the mesh size, nonstructural components, and so on can be considered [25, 26, 30, 31].

5.2. Validation of Similitude. In order to validate the similitude law used for designing and manufacturing the small-scale model, we create an analytical model for the prototype using the analytic technique suggested in Section 5.1. The analytical model for the prototype is compared with the small-scale analytical model, which is validated by comparing its results with that of the small-scale modeling experiment, in order to validate the similitude law. The analytical

modeling technique that is applied to the small-scale analytical model and prototype analytical model is validated via the data from scale modeling experiment, so it is thought that verifying the similitude via a comparison of the two analytical models is valid. The design data for the prototype is shown in Table 2.

The comparison of the two analytical models is shown in Table 5 and Figure 8. As shown in Table 1, if mass-based scaling (similitude of S) is applied, the natural frequency of the small-scale model should be $1/S$ of that of the prototype. The results showed that the frequencies of a scale model that is considered are double those of the prototype, signifying that the mass-based similitude law is indeed valid.

6. Conclusion

As a preliminary study for the development of technology for microvibration designs for cleanroom structures, this study performed a scale modeling experiment and analytical validation of the scaling. First, we manufactured a 1/2 small-scale model for the unit modules of a cleanroom based on the mass-based similitude law and tested the model for its dynamic properties. The experimental results were compared with those of the analysis to acquire an improved analytical modeling.

During the process of fitting with the experimental results, it was found that considering the contributions from

the stiffness of the embedded reinforcement in the concrete would generate more accurate analytical results. In other words, microvibration response, which is considered highly important in evaluating performance for high technology facilities, is sensitive to the stiffness of each member of the structure. Therefore, it is necessary that evaluations of microvibration in high technology facilities take into account the impact of reinforcement. Such analytical modeling technique can contribute to improving the technology for microvibration designs by validating various ideas and examining the effects of design parameters.

Meanwhile, we compared the results produced by the prototype analytical model and small-scale analytical model for cleanroom unit modules to validate the mass-based similitude law used in this study. The results were found to be in line with theory. We expect these outcomes to be used for reference in planning scale model experiments for high technology facilities as well as other large structures in the future.

Competing Interests

The authors declare that there is no conflict of interests regarding the publication of this paper.

Acknowledgments

This research was supported by Basic Science Research Program through the National Research Foundation of Korea (NRF) funded by the Ministry of Education (NRF-2014R1A1A2059874).

References

- [1] K. A. Salyards and R. J. Firman III, "Review of generic and manufacturer design criteria for vibration-sensitive equipment," in *Proceedings of the IMAC-XXVII: Conference & Exposition on Structural Dynamics*, 2009.
- [2] E. E. Ungar, D. H. Sturz, and C. H. Amick, "Vibration control design of high technology facilities," *Sound and Vibration*, vol. 24, no. 7, pp. 20–27, 1990.
- [3] H. Amick, "On generic vibration criteria for advanced technology facilities: with a tutorial on vibration data representation," *Journal of the Institute of Environmental Sciences*, vol. 40, no. 5, pp. 35–44, 1997.
- [4] C. G. Gordon, "Generic criteria for vibration-sensitive equipment," in *Vibration Control in Microelectronics, Optics, and Metrology*, vol. 1619 of *Proceedings of SPIE*, pp. 71–85, San Jose, Calif, USA, 1992.
- [5] C. J. Montgomery, H. Amick, P. Haswell, J. Dibattista, and M. S. Medhekar, "Use of vibration criteria in the selection of structural systems for nanotechnology research facilities," in *Buildings for Nanoscale Research and Beyond*, vol. 5933 of *Proceedings of SPIE*, pp. 1–12, San Diego, Calif, USA, July 2005.
- [6] H. Amick, M. Gendreau, T. Busch, and C. G. Gordon, "Evolving criteria for research facilities: vibration," in *Buildings for Nanoscale Research and Beyond*, vol. 5933 of *Proceedings of SPIE*, San Diego, Calif, USA, 2005.
- [7] C.-L. Lee, Y.-P. Wang, and R. K. L. Su, "Assessment of vibrations induced in factories by automated guided vehicles," *Proceedings of the Institution of Civil Engineers: Structures and Buildings*, vol. 166, no. 4, pp. 182–196, 2013.
- [8] T.-C. Pan, X. You, and C. L. Lim, "Evaluation of floor vibration in a biotechnology laboratory caused by human walking," *Journal of Performance of Constructed Facilities*, vol. 22, no. 3, pp. 122–130, 2008.
- [9] J. M. W. Brownjohn, T.-C. Pan, C. Middleton, S. C. Tan, and G. Yang, "Floor vibration serviceability in a multistory factory building," *Journal of Performance of Constructed Facilities*, vol. 30, no. 1, Article ID 04014203, 2016.
- [10] M. Ismail, J. Rodellar, and F. Ikhouane, "An innovative isolation bearing for motion-sensitive equipment," *Journal of Sound and Vibration*, vol. 326, no. 3–5, pp. 503–521, 2009.
- [11] M. Ismail, J. Rodellar, and J. R. Casas, "Seismic behavior of RNC-isolated bridges: a comparative study under near-fault, long-period, and pulse-like ground motions," *Advances in Materials Science and Engineering*, vol. 2016, Article ID 1897045, 18 pages, 2016.
- [12] B.-W. Huang, J.-H. Kuang, J.-G. Tseng, J.-C. Wang, and Y.-X. Qiu, "Seismic analysis of a viscoelastic damping isolator," *Advances in Materials Science and Engineering*, vol. 2015, Article ID 280625, 6 pages, 2015.
- [13] W. Taniwangsa, "Seismic performance of a base-isolated demonstration building," *Earthquake Spectra*, vol. 18, no. 4, pp. 777–793, 2002.
- [14] H. Amick, S. Hardash, P. Gillett, and R. J. Reaveley, "Design of stiff, low-vibration floor structures," in *Vibration Control in Microelectronics, Optics, and Metrology*, vol. 1619 of *Proceedings of SPIE*, pp. 180–191, San Jose, Calif, USA, 1992.
- [15] A. Pavic and P. Reynolds, "Vibration serviceability of long-span concrete building floors. Part I: review of background information," *Shock and Vibration Digest*, vol. 34, no. 3, pp. 191–211, 2002.
- [16] C. J. Middleton and J. M. W. Brownjohn, "Response of high frequency floors: a literature review," *Engineering Structures*, vol. 32, no. 2, pp. 337–352, 2010.
- [17] C. Q. Howard and C. H. Hansen, "Vibration analysis of waffle floors," *Computers and Structures*, vol. 81, no. 1, pp. 15–26, 2003.
- [18] J. M. Bracci, A. M. Reinhorn, and J. B. Mander, "Seismic resistance of reinforced concrete frame structures designed for gravity loads: performance of structural system," *ACI Materials Journal*, vol. 92, no. 5, pp. 597–609, 1995.
- [19] L. A. Fahnestock, J. M. Ricles, and R. Sause, "Experimental evaluation of a large-scale buckling-restrained braced frame," *Journal of Structural Engineering*, vol. 133, no. 9, pp. 1205–1214, 2007.
- [20] L. Zeng, Z. Cui, Y. Xiao, S. Jin, and Y. Wu, "Cyclical behavior of concrete-encased composite frame joints with high strength concrete," *Advances in Materials Science and Engineering*, vol. 2015, Article ID 873162, 13 pages, 2015.
- [21] Y. Zhou, T. Kijewski, and A. Kareem, "Along-wind load effects on tall buildings: comparative study of major international codes and standards," *Journal of Structural Engineering*, vol. 128, no. 6, pp. 788–796, 2002.
- [22] J.-S. Hwang, A. Kareem, and H. Kim, "Wind load identification using wind tunnel test data by inverse analysis," *Journal of Wind Engineering and Industrial Aerodynamics*, vol. 99, no. 1, pp. 18–26, 2011.
- [23] S. W. Choi, J. H. Seo, H. M. Lee, Y. Kim, and H. S. Park, "Wind-induced response control model for high-rise buildings based on resizing method," *Journal of Civil Engineering and Management*, vol. 21, no. 2, pp. 239–247, 2015.

- [24] A. M. Raich and T. R. Liskai, "Multi-objective optimization of sensor and excitation layouts for frequency response function-based structural damage identification," *Computer-Aided Civil and Infrastructure Engineering*, vol. 27, no. 2, pp. 95–117, 2012.
- [25] R. K. L. Su, A. M. Chandler, M. N. Sheikh, and N. T. K. Lam, "Influence of non-structural components on lateral stiffness of tall buildings," *The Structural Design of Tall and Special Buildings*, vol. 14, no. 2, pp. 143–164, 2005.
- [26] J. Y. Kim, E. Yu, D. Y. Kim, and S.-D. Kim, "Calibration of analytical models to assess wind-induced acceleration responses of tall buildings in serviceability level," *Engineering Structures*, vol. 31, no. 9, pp. 2086–2096, 2009.
- [27] T. Xu, "Characterization of minienvironments in a clean room: design characteristics and environmental performance," *Building and Environment*, vol. 42, no. 8, pp. 2993–3000, 2007.
- [28] Y.-C. Shih, A.-S. Yang, and C.-W. Lu, "Using air curtain to control pollutant spreading for emergency management in a cleanroom," *Building and Environment*, vol. 46, no. 5, pp. 1104–1114, 2011.
- [29] K.-C. Noh, H.-S. Kim, and M.-D. Oh, "Study on contamination control in a minienvironment inside clean room for yield enhancement based on particle concentration measurement and airflow CFD simulation," *Building and Environment*, vol. 45, no. 4, pp. 825–831, 2010.
- [30] C. H. Lee, K. B. Song, and H. W. Kim, "Vibration analysis and evaluation for the offshore structure using simplified model and RSS method," in *Proceedings of the ASME 31st International Conference on Ocean, Offshore and Arctic Engineering (OMAE '12)*, pp. 637–641, American Society of Mechanical Engineers, Rio de Janeiro, Brazil, July 2012.
- [31] M. Imregun, K. Y. Sanliturk, and D. J. Ewins, "Finite element model updating using frequency response function data: II. Case study on a medium-size finite element model," *Mechanical Systems and Signal Processing*, vol. 9, no. 2, pp. 203–213, 1995.
- [32] D. J. Nefske and S. H. Sung, "Correlation of a coarse-mesh finite element model using structural system identification and a frequency response assurance criterion," in *Proceedings of the SPIE the International Society for Optical Engineering*, SPIE International Society for Optical, 1996.

Research Article

Structural Stability and Dynamics of FGM Plates Using an Improved 8-ANS Finite Element

Weon-Tae Park

Division of Construction and Environmental Engineering, Kongju National University, 275 Budai, Cheonan 330-717, Republic of Korea

Correspondence should be addressed to Weon-Tae Park; pwtiae@kongju.ac.kr

Received 22 April 2016; Accepted 7 June 2016

Academic Editor: Guillermo Rus

Copyright © 2016 Weon-Tae Park. This is an open access article distributed under the Creative Commons Attribution License, which permits unrestricted use, distribution, and reproduction in any medium, provided the original work is properly cited.

I investigate the vibration and buckling analysis of functionally graded material (FGM) structures, using a modified 8-node shell element. The properties of FGM vary continuously through the thickness direction according to the volume fraction of constituents defined by sigmoid function. The modified 8-ANS shell element has been employed to study the effect of power law index on dynamic analysis of FGM plates with various boundary conditions and buckling analysis under combined loads, and interaction curves of FGM plates are carried out. To overcome shear and membrane locking problems, the assumed natural strain method is employed. In order to validate and compare the finite element numerical solutions, the reference results of plates based on Navier's method, the series solutions of sigmoid FGM (S-FGM) plates are compared. Results of the present study show good agreement with the reference results. The solutions of vibration and buckling analysis are numerically illustrated in a number of tables and figures to show the influence of power law index, side-to-thickness ratio, aspect ratio, types of loads, and boundary conditions in FGM structures. This work is relevant to the simulation of wing surfaces, aircrafts, and box structures under various boundary conditions and loadings.

1. Introduction

Functionally graded material (FGM) is a special kind of composites in which the material properties vary continuously and smoothly from one surface to the other. One of the main advantages of FGM is that it mitigates acute stress concentrations and singularities at intersections between interfaces usually presented in laminated composites. Chung and Chi [1] proposed a sigmoid FGM, which is composed of two power law functions to define a new volume fraction and indicated that the use of a sigmoid FGM can significantly reduce the stress intensity factors of a cracked body. Recent work on the bending, vibration, buckling, and transient analysis of FGM plates can be founded in Han et al. [2, 3] and Jung and Han [4]. Recently, the works on FGM and shear deformation theories with the thickness stretching effect are employed and developed by researchers (Belabed et al. [5], Hamidi et al. [6], Lee et al. [7], and Han et al. [8]).

It should be noted that they only investigated structural behaviors of simply supported FGM plates. Thus, needs exist for the development of shell finite element which is simple

to use for vibration and buckling analysis FGM plates with arbitrary boundary conditions.

When compressive loads are applied onto most structures including FGM plates, they tend to buckle or are subjected to dynamic loads during their operation. Understanding the natural frequency and buckling behavior is an important issue from design perspective. Consequently, numerous studies on vibration and buckling of various plates can be found in literatures. For proper use of FGM plates as various structural components, their dynamic and stability response should be studied. To the best of the author's knowledge, there are no solutions for structural stability response of FGM plates under combined compressive, tensile, and shear loads based on shear deformation theory of plate.

Bucalem and Bathe [9] improved the MITC8 shell elements [10] and concluded that while it performed quite effectively in some cases, in a few analyses the element presented a very stiff behavior rendering. In 8-node shell element [11, 12], the keeping of locking phenomena was found to continue through numerical solutions on the standard test problem of Macneal and Harder [13]. In order to improve the 8-node

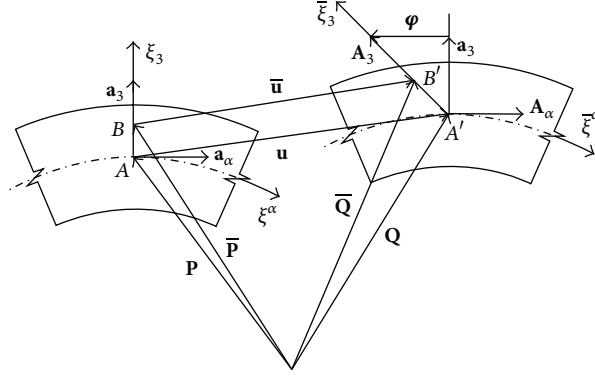


FIGURE 1: Kinematics of the first-order shear deformation theory.

ANS shell element, a new combination of sampling points is adopted. Recently, Han et al. [14] presented modified 8-ANS shell element using the new interpolation functions and combination of sampling points for the assumed natural strain.

However, a few literatures have been found on the dynamic analysis of FGM plates with various boundary conditions and structural stability analysis under combined compressive, tensile, and shear loads. In the present work modified 8-ANS shell element has been employed to study the effect of power law index on dynamic analysis of FGM plates with various boundary conditions and buckling analysis under combined compressive, tensile, and shear loads. To validate the present 8-ANS shell element models, the numerical examples are studied and compared with those results from the references. The solutions of vibration and buckling analysis are numerically illustrated in a number of tables and figures to show the influence of power law index, side-to-thickness ratio, aspect ratio, types of loads, and boundary conditions in FGM structures.

2. Modified 8-ANS Finite Element

2.1. Kinematics of Shell. The displacement $\bar{\mathbf{u}}$ of an arbitrary point of the shell (see Figure 1) for the first-order shear deformation theory can be expressed

$$\bar{\mathbf{u}}(\xi^\alpha) = \mathbf{u}(\xi^\alpha) + \xi_3 \boldsymbol{\varphi}(\xi^\alpha), \quad (1)$$

where $\boldsymbol{\varphi}$ is vector of rotation at the midsurface of shell.

A three-dimensional Green's strain tensor in the linear case (infinitesimal strain theory) is given by

$$2E_{ij} = \bar{\mathbf{u}}_{,i} \cdot \mathbf{g}_j + \bar{\mathbf{u}}_{,j} \cdot \mathbf{g}_i, \quad (2)$$

where a comma $(\)_{,i} = \partial/\partial \xi^i$ is partial differentiation and \mathbf{g}_i is a triad of base vectors for the spatial coordinates ξ^i at the surfaces ($\xi_3 = \text{const.}$) parallel to the midsurface of shell. If the displacement equation (1) is substituted into (2), the strain-displacement relations are obtained. From these strain-displacement relations, kinematics in different curvilinear coordinates can be acquired and expressed through the physical components in the matrix form

$$\mathbf{E} = \mathbf{B}\mathbf{U}, \quad (3)$$

where \mathbf{U} are physical components of displacement \mathbf{u} and rotation $\boldsymbol{\varphi}$ as follows:

$$\mathbf{U}^T = [u_1, u_2, u_3, \phi_1, \phi_2, \phi_3]. \quad (4)$$

The shell theory presented above is the so-called first-order shear deformation theory with six degrees of freedom.

2.2. Various Enhanced Strain Interpolation Patterns. In this study, the ordinary 8 nodes of Lagrangian displacement interpolations are used and the various combinations of assumed natural strain interpolation functions are employed for the very efficient 8-node shell element. Figure 2 shows various patterns of sampling points that can be used for membrane, in-plane shear, and out-of-plane shear strain interpolations for the new 8-ANS finite element. Based on Figure 2, the β pattern is used for membrane and the δ pattern and γ_6^* pattern are used for in-plane and out-of-plane shear, respectively. The interpolation functions by Polit et al. [16] are used in the γ_6^* patterns. In the γ_6^* patterns, the strain component of center point is replaced by the mean of the components at points S_1 and S_2 (Bathe and Dvorkin, [10]).

3. Material Properties of the FGM

An FGM can be defined by the variation in the volume fractions. In this paper, the sigmoid function is used for FGM structures. The volume fraction using two power law functions which confirm smooth distribution of stresses is defined by

$$V_f^1(t) = 1 - \frac{1}{2} \left(\frac{h/2 - t}{h/2} \right)^p \quad \text{for } 0 \leq t \leq \frac{h}{2}, \quad (5a)$$

$$V_f^2(t) = \frac{1}{2} \left(\frac{h/2 + t}{h/2} \right)^p \quad \text{for } -\frac{h}{2} \leq t \leq 0, \quad (5b)$$

where subscripts 1 and 2 represent the two materials used and p is the power law index, which indicates the material variation profile through the thickness. The material properties

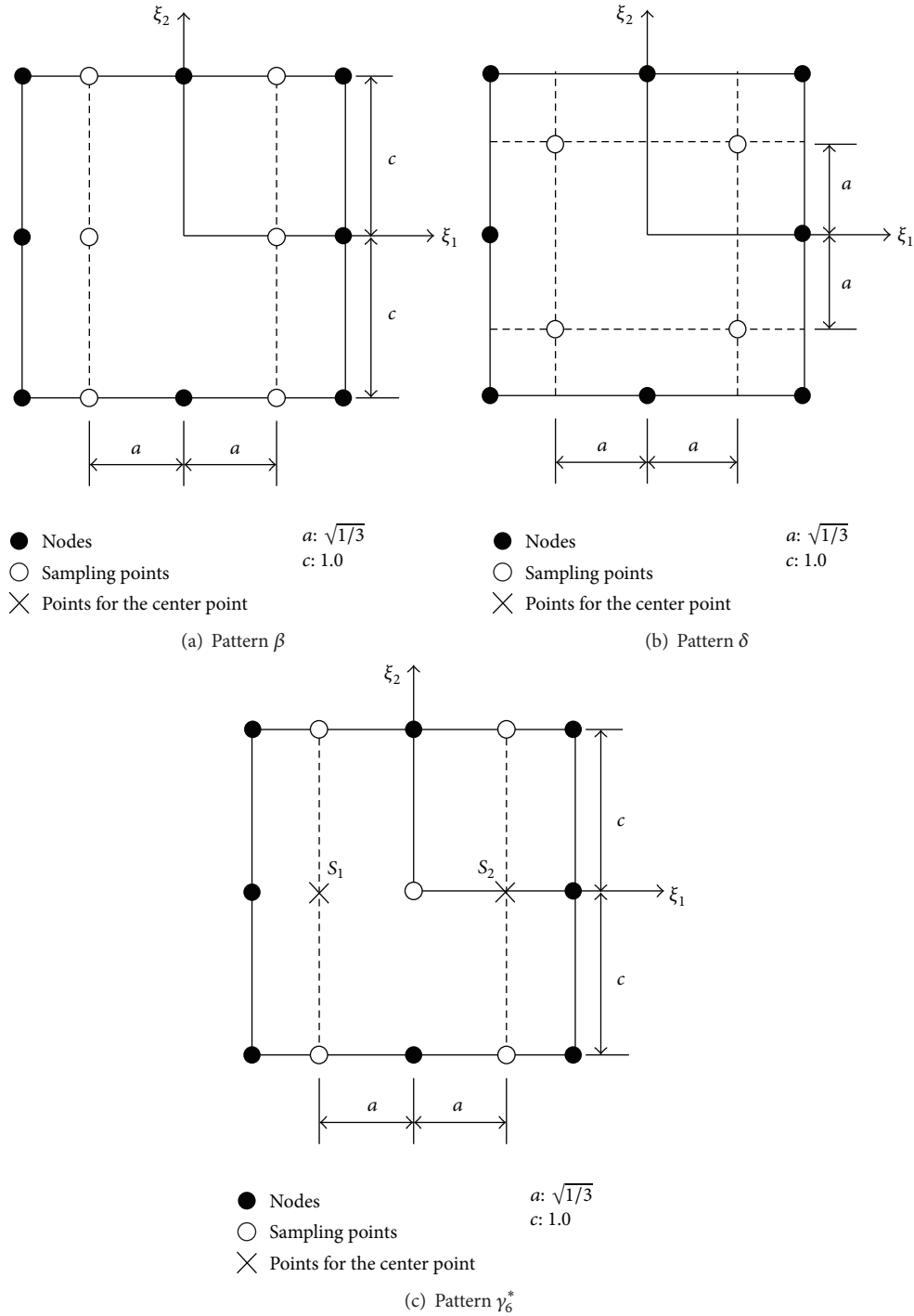


FIGURE 2: Four possible patterns of sampling points for 8-node ANS shell element.

of the S-FGM using the rule of mixture can be expressed as follows:

$$H(t) = V_f^1(t) H_1 + (1 - V_f^1(t)) H_2 \quad \text{for } 0 \leq t \leq \frac{h}{2}, \quad (6a)$$

$$H(t) = V_f^2(t) H_1 + (1 - V_f^2(t)) H_2 \quad \text{for } -\frac{h}{2} \leq t \leq 0. \quad (6b)$$

4. Equilibrium Equation

By using virtual work principle, the equilibrium equation is obtained based on the membrane (\mathbf{N}), bending (\mathbf{M}), and transverse shear resultant forces (\mathbf{Q}) as follows:

$$\int \left(\delta (E_{\alpha\beta}^m)^T \mathbf{N} + \delta (E_{\alpha\beta}^b)^T \mathbf{M} + \delta (E_{\alpha 3}^s)^T \mathbf{Q} \right) dA \equiv \delta \mathbf{u}^T \mathbf{K}_L \mathbf{u} = \int \mathbf{f} \cdot \delta \mathbf{u} dV, \quad (7)$$

TABLE I: Results of patch test under bending, shear, and tension.

Patch tests	Bending	Shear	Tension
Reference solutions	$\theta_y = \frac{ML}{EI} = 0.12 \times 10^{-4}$	$w = \frac{6SL}{5GA} = 0.312 \times 10^{-5}$	$u = \frac{TL}{EA} = 1.0 \times 10^{-6}$
Normalized solutions	1.000	1.000	0.992

where $E_{\alpha\beta}^m$, $E_{\alpha\beta}^b$, and $E_{\alpha\beta}^s$ are membrane, bending, and transverse shear strain components, \mathbf{K}_L is the linear stiffness matrix, and \mathbf{f} is the body force.

5. Buckling and Vibration Analysis

When the equation is employed to estimate buckling loads, the stability condition may be simplified by

$$\mathbf{K}_L \mathbf{u}^a + \lambda_{cr} \mathbb{G} \mathbf{u}^a = 0, \quad (8)$$

where \mathbf{u}^a is the vector of the nodal value of the displacements, λ_{cr} is the buckling load parameter and denotes the proportional increase in load needed to reach neutral equilibrium, and \mathbb{G} is the geometric stiffness matrix. Applying to the structure a reference loading N_{ref} and carrying out a generalized linear static analysis, (8) represents the standard eigenvalue problem. The lowest eigenvalue λ_{cr} in (8) is associated with buckling load. Therefore, the buckling load can be obtained by

$$N_{cr} = \lambda_{cr} N_{ref}. \quad (9)$$

The consistent mass is used to formulate the mass matrices for the FGM shell element. The mass matrix is determined using interpolation functions as follows:

$$M = \int_V \rho N^T N dV, \quad (10)$$

where N is a matrix of shape functions.

Unlike (8), the governing equations of motion for free vibration analysis are of the form

$$\mathbf{K}_L \ddot{\mathbf{u}}^a + M \dot{\dot{\mathbf{u}}}^a = 0, \quad (11)$$

where the superposed dot denotes differentiation with respect to time.

6. Numerical Results

6.1. Patch Test. Firstly, the patch tests proposed by Simo et al. [15] are investigated. In Figure 3, the boundary conditions and loading types are presented, simultaneously. The normalized solutions of nodal displacements on the right edges are shown in Table I. The nondimensional form is expressed as follows:

$$\text{Normalized solution} = \frac{\text{Present solution}}{\text{Reference solution}}. \quad (12)$$

6.2. Vibration Analysis

6.2.1. Simply Supported Rectangular FGM Plate. To validate the present 8-ANS finite element with FGM, a sigmoid FGM plate with geometrical properties is shown in Figure 4. The material properties are given by

$$\begin{aligned} E_1 &= 151 \times 10^9 \text{ Pa}, \\ \rho_1 &= 3000 \text{ kg/m}^3, \\ E_2 &= 70 \times 10^9 \text{ Pa}, \\ \rho_2 &= 2707 \text{ kg/m}^3, \\ \nu_1 &= \nu_2 = 0.3, \end{aligned} \quad (13)$$

where E_1 , ρ_1 , ν_1 and E_2 , ρ_2 , ν_2 express the property of the top and bottom faces of the plate, respectively. Equation (13) is used in computing the numerical values of all cases.

The nondimensional form of the results is defined by

$$\bar{\omega} = \omega \left(\frac{a^2}{h} \sqrt{\frac{\rho_1}{E_2}} \right). \quad (14)$$

Table 2 shows the nondimensional natural frequency of S-FGM simply supported plates for convergence test. It is noticed that present 8-ANS finite element shows an excellent agreement to the result by analytical solution.

It is shown that the natural frequency of pure metal plate is smaller than that of pure ceramic plate in Table 3. The natural frequencies of the functionally graded material plates are intermediate to that of the metal and ceramic plates. Table 3 shows that numerical results of vibration analysis are reduced by increasing the power law p .

Table 4 shows the numerical results of FGM plate for which $p = 10$. In this example, the natural frequency is normalized with respect to the plate width a , thickness h , density ρ_1 , and elastic modulus E_2 for various rectangular plate aspect ratios. As the plate aspect ratio increases, the natural frequency reduces and approaches 3.69.

6.2.2. FGM Plate with Arbitrary Edges. For convenience, a four-letter notation is used to describe the boundary conditions of the edges (see Figure 5). For example, CFSF indicates that first edge is clamped (C), second edge is free (F), third edge is simply supported (S), and the last is free (F). The natural frequencies of FGM CFFF plates are investigated and presented in Table 5. The results are expressed in the nondimensional form using (15). Numerical results show that the natural frequencies are reduced by increasing the power

TABLE 2: Normalized nondimensional natural frequency of S-FGM plate (power law index: $p = 10$).

Nodes per side	4-node shell element (see [2]) ^b	Ratio ([2]/exact)	Present	Ratio (present/exact)
5	8.076	1.105	7.717	1.056
9	7.517	1.029	7.351	1.006
17	7.366	1.008	7.323	1.002
33	7.329	1.003	—	—
Analytical solution ^a	7.307	—	—	—

^aResult is computed using Navier’s method with first-order shear deformation theory, independently.

^bResults are computed using the quasi-conforming 4-ANS finite element, independently.

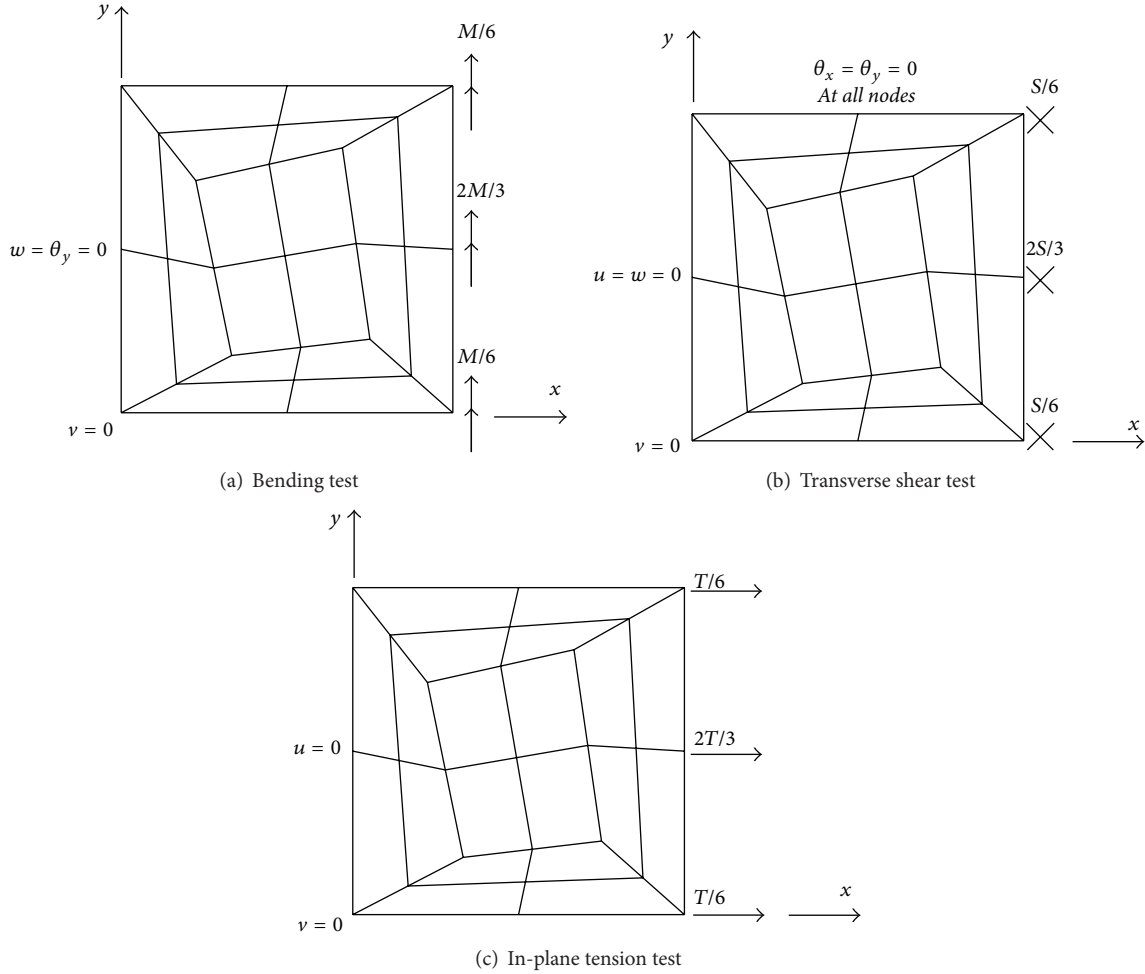


FIGURE 3: Mesh for patch test (Simo et al. [15]). Length of the square $L = 10$; Young’s modulus $E = 1.0 \times 10^7$; Poisson’s ratio $\nu = 0.3$; and thickness $h = 1.0$ and boundary displacement conditions for patch tests.

law index p . The results also confirm that power law index has significant effect on the dynamic response of FGM plates:

$$\bar{\omega} = \omega \left(\frac{a^2}{h} \sqrt{\frac{\rho_1}{E_2}} \right) \times 10. \quad (15)$$

In Table 6, the natural frequencies of FGM plates with arbitrary boundary conditions are presented. Four arbitrary values of the power law index p are examined. As expected,

results show that the natural frequencies are reduced by increasing the power law index p .

Based on present study, comprehensive results of natural frequency of FGM plates are also illustrated in Figure 7 for different boundary conditions. In each boundary condition, five different power law indices are considered. In Figure 8, two different values of side-to-thickness ratio are examined. In addition, five arbitrary values of the power law index are examined. These new results can be used for comparison with further FG plate models.

TABLE 3: Nondimensional natural frequency of simply supported FGM plates ($a/h = 100$).

Material parameter (p)	Navier solution	Mode number					
		1		2		3	
		Ref. [2]	Present	Ref. [2]	Present	Ref. [2]	Present
Pure ceramic	8.992 ^a	9.041 ^a	8.772	22.705 ^a	21.940	22.705 ^a	21.940
$p = 1$	7.518	7.555	7.526	18.992	18.819	18.993	18.820
$p = 2$	7.419	7.457	7.430	18.745	18.575	18.747	18.576
$p = 5$	7.333	7.373	7.348	18.533	18.365	18.535	18.367
$p = 10$	7.307	7.348	7.323	18.470	18.302	18.472	18.304
Pure metal	6.123 ^a	6.148 ^a	6.287	15.459 ^a	15.726	15.459 ^a	15.726

^aResults are calculated by $\rho = (\rho_1 + \rho_2)/2$.

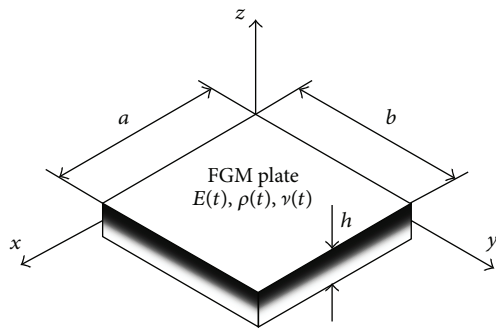


FIGURE 4: Geometry of FGM plates.

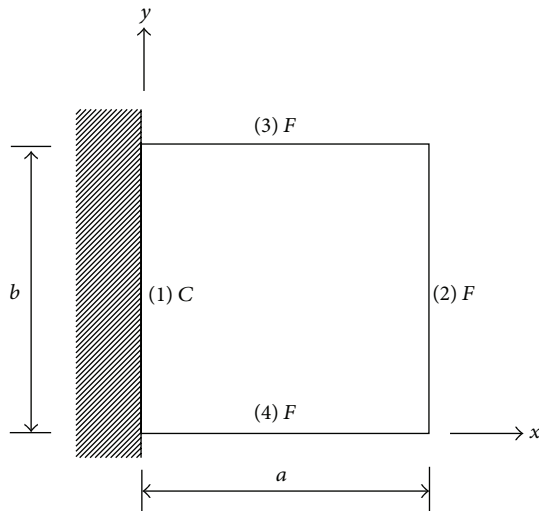


FIGURE 5: Geometry of FGM cantilever plates.

TABLE 4: Nondimensional fundamental frequency of simply supported FGM plates with various aspect ratio ($p = 10$).

Solutions	Aspect ratio (b/a)			
	0.5	2.0	5.0	10.0
Navier solution	18.258	4.568	3.800	3.691
Ref. [2]	18.346	4.593	3.817	3.706
Present	18.276	4.577	3.803	3.692

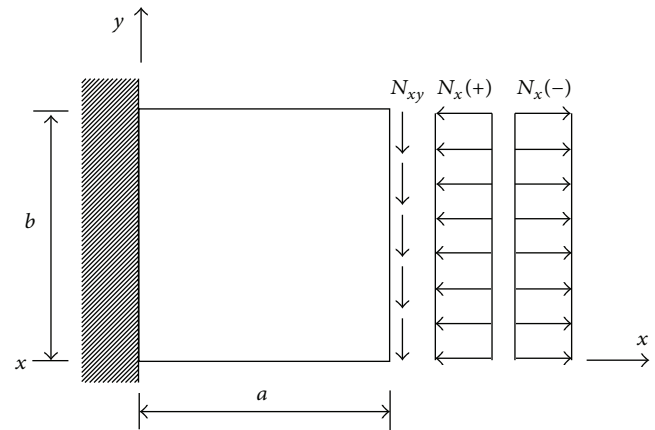


FIGURE 6: FGM cantilever plates under combined loads.

6.3. Buckling Analysis

6.3.1. *Simply Supported Rectangular FGM Plate.* For validation, the stability analysis results of S-FGM simply supported plates (see Figure 4) using Navier’s method are compared with present 8-ANS finite element. The material properties and nondimensional form are used as shown in Section 6.2.1 and (14), respectively. It is shown that the pure ceramic plate has the largest buckling load and the pure metal plate has the

smallest one in Table 7. The buckling loads of the FGM plates are intermediate to that of the metal and ceramic plates.

The buckling loads versus the plate aspect ratio are presented in Table 8. There, for large plate aspect ratios (i.e., $b/a \geq 2.0$), the plate buckles into a single half wave in the x -direction. As the plate aspect ratio decreases, the plate buckles with increasing half waves in the x -direction.

6.3.2. *FGM Cantilever Plate.* In Table 9, the stability analysis results of S-FGM cantilever plates (see Figure 6) with various aspect ratio are presented. The results are presented in the nondimensional form. Numerical results show that the buckling loads are reduced by increasing the power law index p . The results also confirm that power law index has significant effect on the buckling loads of FGM cantilever plates. The stability analysis results of S-FGM cantilever plates

TABLE 5: Nondimensional natural frequency of FGM CFFF plates ($a/h = 100$).

Material parameter (p)	Mode number							
	1		2		3		4	
	Ref. [2]	Present						
Pure ceramic	15.814 ^a	15.430	38.767 ^a	37.780	97.148 ^a	94.570	124.28 ^a	120.80
$p = 1$	13.222	13.228	32.415	32.389	81.236	81.074	103.92	103.56
$p = 2$	13.047	13.052	31.986	31.960	80.166	80.000	102.54	102.19
$p = 5$	12.896	12.901	31.617	31.590	79.244	79.073	101.36	101.00
$p = 10$	12.851	12.856	31.507	31.480	78.969	78.797	101.01	100.65
Pure metal	10.767 ^a	11.060	26.395 ^a	27.079	66.144 ^a	67.785	84.615 ^a	86.584

^aResults of [2] are calculated by $\rho = (\rho_1 + \rho_2)/2$.

TABLE 6: Nondimensional natural frequency of FGM plates ($a/h = 100$).

Material parameter (p)	Boundary conditions				
	CFFF	SSFF	SSSS	CCFF	CCSS
Pure ceramic	15.430	54.302	87.718	98.502	128.59
$p = 1$	13.228	46.643	75.264	84.446	110.25
$p = 2$	13.052	46.078	74.304	83.327	108.79
$p = 5$	12.901	45.591	73.478	82.364	107.53
$p = 10$	12.856	45.446	73.231	82.077	107.15
Pure metal	11.060	38.922	62.873	70.603	92.176

TABLE 7: Nondimensional buckling loads of FGM simply supported plates ($\bar{N}_{cr} = N_{cr}b^2/E_2h^3$).

Material parameter (p)	Navier solution	Ref. [2]	Present
Pure ceramic	7.794	7.828	7.797
$p = 1$	5.448	5.484	5.466
$p = 2$	5.305	5.346	5.331
$p = 5$	5.183	5.229	5.216
$p = 10$	5.147	5.195	5.182
Pure metal	3.613	3.629	3.615

TABLE 8: Nondimensional buckling loads of FGM simply supported plates ($\bar{N}_{cr} = N_{cr}b^2/E_2h^3$, $p = 10$).

Solutions	Aspect ratio (b/a)			
	0.5	2.0	5.0	10.0
Navier solution	5.138	8.043	34.800	131.28
Ref. [2]	5.211	8.127	34.969	131.87
Present	5.165	8.110	34.859	131.37

under various loading types are investigated in Table 10. As expected, numerical results show that the buckling loads are reduced by increasing the power law index p and also confirm that loading types have very significant effect on the buckling loads of FGM cantilever plates.

Based on present study, comprehensive results of buckling loads of FGM plates under combined loads are also illustrated in Figures 9 and 10 for CFFF boundary conditions. The influence of in-plane load direction on the relationship

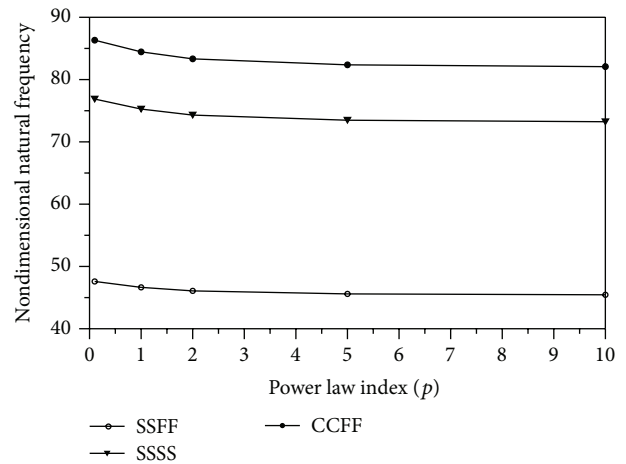


FIGURE 7: Effect of power law index on the nondimensional natural frequency of FGM plate with arbitrary edges.

between critical shear and in-plane loading is studied, when acting in combination. It is noticed that the tension may produce positive stiffness and the FGM plate becomes stronger than when it is subjected to compression.

In Figure 10, the natural frequencies of FGM plates under combined loading are investigated. Four arbitrary values of the power law index p are examined. As expected, results show that the buckling loads are increased by decreasing the power law index p .

TABLE 9: Nondimensional buckling loads of FGM plates ($\bar{N}_{cr} = (N_{cr}b^2/E_2h^3) \times 10$).

Material parameter (p)	Aspect ratio (b/a)							
	1		2		5		10	
	Ref. [2]	Present	Ref. [2]*	Present	Ref. [2]*	Present	Ref. [2]*	Present
Pure ceramic	4.693	4.679	9.551	19.040	24.160	120.75	48.449	485.42
$p = 1$	3.281	3.271	6.677	13.310	16.890	84.411	33.872	339.32
$p = 2$	3.194	3.185	6.501	12.959	16.445	82.185	32.981	330.38
$p = 5$	3.121	3.111	6.351	12.660	16.067	80.293	32.224	322.77
$p = 10$	3.099	3.090	6.307	12.572	15.955	79.733	32.000	320.52
Pure metal	2.176	2.169	4.428	8.8265	11.200	55.979	22.460	225.03

*Results of [2] are calculated by $\bar{N}_{cr} = (N_{cr}a^2/E_2h^3)(b/a) \times 10$.

TABLE 10: Nondimensional buckling loads of FGM plates ($\bar{N}_{cr} = (N_{cr}b^2/E_2h^3) \times 10$).

Material parameter (p)	Types of combined loading			
	Compression	Shear + comp.	Pure shear	Shear + tension
	Present	Present	Present	Present
Pure ceramic	4.679	4.279	15.135	95.116
$p = 1$	3.271	2.991	10.580	66.495
$p = 2$	3.185	2.912	10.302	64.745
$p = 5$	3.111	2.845	10.065	63.257
$p = 10$	3.090	2.826	9.9946	62.816
Pure metal	2.169	1.984	7.0163	44.094

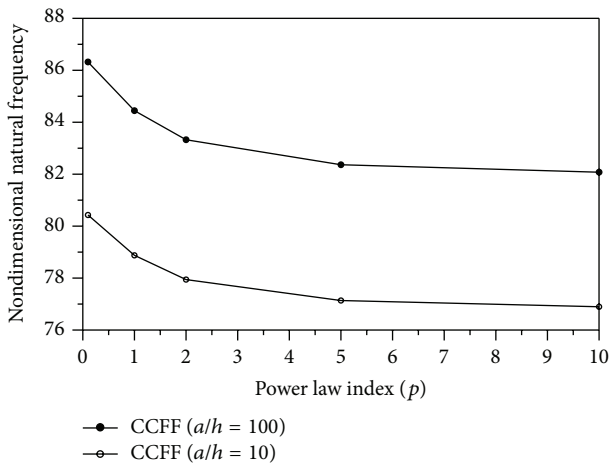


FIGURE 8: Effect of power law index on the nondimensional natural frequency of CCFF FGM plate with variation of side-to-thickness ratio.

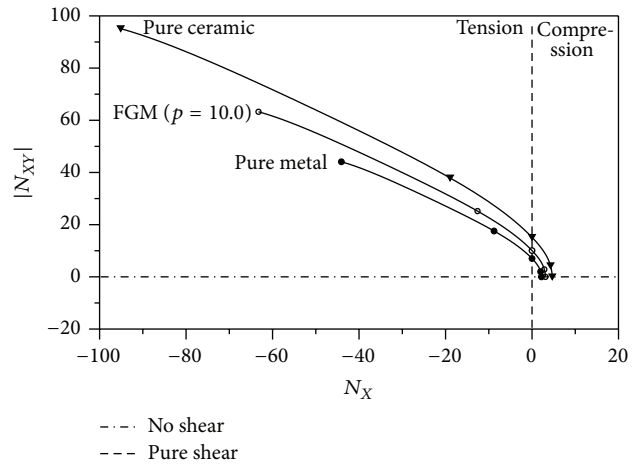


FIGURE 9: Buckling load of FGM plates: combined compressive, tensile, and shear loading.

7. Concluding Remarks

The natural frequency and buckling response have been studied for FGM plates. Extensive results obtained from computations refer to different loading, different geometry, different boundaries, and different power law indices. The advanced finite element analysis based on the modified 8-node ANS formulation shows the significance of various boundary conditions and loading conditions for FGM plates. From this study, a number of conclusions have been founded.

- (1) It is shown that the natural frequencies are reduced by increasing the power law index p . The results also confirm that power law index has significant effect on the dynamic response of FGM plates.
- (2) Dynamic response of FGM plates is affected by its boundary conditions. Clamped edges always produce a higher performance of the FGM plates than simply supported edges.
- (3) It is noticed that the tension may produce positive stiffness and the FGM plate becomes stronger than

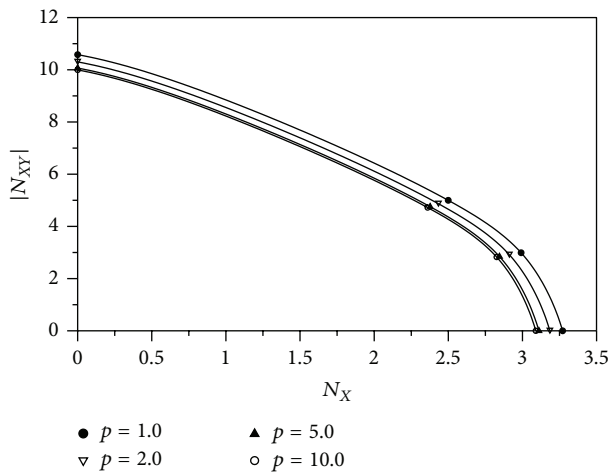


FIGURE 10: Buckling load of FGM plates with various power law index: combined compressive and shear loading.

when it is subjected to compression. For combined shear and compressive loading the stability envelopes are symmetric about the line N_{xy} .

- (4) The suitable selection of sampling point used in ANS method is very important for vibration and buckling behavior of FGM plates. It is noticed that locking phenomenon occurs in the results of reference when the plates become very thin. This phenomenon may lead us to a conclusion that the suitable selection of sampling points prevents the locking problem from occurring in vibration and buckling analysis of either thick FGM plates or very thin ones.

In order to design the FGM plates under the in-plane shear loading, the present formulation and results may serve as benchmark for future guidelines and may be extended to dynamic instability analysis of various FGM structures. The numerical results of present study may serve as benchmark for future guidelines in designing FGM plates under compressive, tension, shear, and combined loading with arbitrary boundary conditions. Also, the present theory should provide engineers with the capability for the design of various FGM plates and shells.

Competing Interests

The author declares that there are no competing interests regarding the publication of this paper.

Acknowledgments

This work was supported by the research grant of the Kongju National University in 2015.

References

- [1] Y. L. Chung and S. H. Chi, "The residual stress of functionally graded materials," *Journal of Chinese Institute of Civil and Hydraulic Engineering*, vol. 13, pp. 1–9, 2001.
- [2] S.-C. Han, G. R. Lomboy, and K.-D. Kim, "Mechanical vibration and buckling analysis of FGM plates and shells using a four-node quasi-conforming shell element," *International Journal of Structural Stability and Dynamics*, vol. 8, no. 2, pp. 203–229, 2008.
- [3] S.-C. Han, W.-H. Lee, and W.-T. Park, "Non-linear analysis of laminated composite and sigmoid functionally graded anisotropic structures using a higher-order shear deformable natural Lagrangian shell element," *Composite Structures*, vol. 89, no. 1, pp. 8–19, 2009.
- [4] W.-Y. Jung and S.-C. Han, "Transient analysis of FGM and laminated composite structures using a refined 8-node ANS shell element," *Composites Part B: Engineering*, vol. 56, pp. 372–383, 2014.
- [5] Z. Belabed, M. S. Ahmed Houari, A. Tounsi, S. R. Mahmoud, and O. Anwar Bég, "An efficient and simple higher order shear and normal deformation theory for functionally graded material (FGM) plates," *Composites Part B: Engineering*, vol. 60, pp. 274–283, 2014.
- [6] A. Hamidi, M. S. A. Houari, S. R. Mahmoud, and A. Tounsi, "A sinusoidal plate theory with 5-unknowns and stretching effect for thermomechanical bending of functionally graded sandwich plates," *Steel and Composite Structures*, vol. 18, no. 1, pp. 235–253, 2015.
- [7] W.-H. Lee, S.-C. Han, and W.-T. Park, "A refined higher order shear and normal deformation theory for E-, P-, and S-FGM plates on Pasternak elastic foundation," *Composite Structures*, vol. 122, pp. 330–342, 2015.
- [8] S. C. Han, W. T. Park, and W. Y. Jung, "3D graphical dynamic responses of FGM plates on Pasternak elastic foundation based on quasi-3D shear and normal deformation theory," *Composites Part B: Engineering*, vol. 95, pp. 324–334, 2016.
- [9] M. L. Buclelem and K. J. Bathe, "High-order MITC general shell elements," *International Journal for Numerical Methods in Engineering*, vol. 36, no. 21, pp. 3729–3754, 1993.
- [10] K.-J. Bathe and E. N. Dvorkin, "A formulation of general shell elements—the use of mixed interpolation of tensorial components," *International Journal for Numerical Methods in Engineering*, vol. 22, no. 3, pp. 697–722, 1986.
- [11] K. D. Kim and T. H. Park, "An 8-node assumed strain element with explicit integration for isotropic and laminated composite shells," *Structural Engineering and Mechanics*, vol. 13, no. 4, pp. 387–410, 2002.
- [12] K. D. Kim, G. R. Lomboy, and S. C. Han, "A co-rotational 8-node assumed strain shell element for postbuckling analysis of laminated composite plates and shells," *Computational Mechanics*, vol. 30, no. 4, pp. 330–342, 2003.
- [13] R. H. Macneal and R. L. Harder, "A proposed standard set of problems to test finite element accuracy," *Finite Elements in Analysis and Design*, vol. 1, no. 1, pp. 3–20, 1985.
- [14] S.-C. Han, W. Kanok-Nukulchai, and W.-H. Lee, "A refined finite element for first-order plate and shell analysis," *Structural Engineering and Mechanics*, vol. 40, no. 2, pp. 191–213, 2011.
- [15] J. C. Simo, D. D. Fox, and M. S. Rifai, "On a stress resultant geometrically exact shell model. Part II: the linear theory; computational aspects," *Computer Methods in Applied Mechanics and Engineering*, vol. 73, no. 1, pp. 53–92, 1989.
- [16] O. Polit, M. Touratier, and P. Lory, "A new eight-node quadrilateral shear-bending plate finite element," *International Journal for Numerical Methods in Engineering*, vol. 37, no. 3, pp. 387–411, 1994.

Research Article

Analysis of Dynamic Fracture Parameters in Functionally Graded Material Plates with Cracks by Graded Finite Element Method and Virtual Crack Closure Technique

Li Ming Zhou,¹ Guang Wei Meng,¹ Xiao Lin Li,² and Feng Li¹

¹School of Mechanical Science and Engineering, Jilin University, No. 5988 Renmin Street, Changchun 130022, China

²College of Construction Engineering, Jilin University, No. 2013 Western Democratic Street, Changchun 130026, China

Correspondence should be addressed to Guang Wei Meng; mgw@jlu.edu.cn

Received 20 February 2016; Revised 13 April 2016; Accepted 28 April 2016

Academic Editor: Ireneusz Kreja

Copyright © 2016 Li Ming Zhou et al. This is an open access article distributed under the Creative Commons Attribution License, which permits unrestricted use, distribution, and reproduction in any medium, provided the original work is properly cited.

Based on the finite element software ABAQUS and graded element method, we developed a dummy node fracture element, wrote the user subroutines UMAT and UEL, and solved the energy release rate component of functionally graded material (FGM) plates with cracks. An interface element tailored for the virtual crack closure technique (VCCT) was applied. Fixed cracks and moving cracks under dynamic loads were simulated. The results were compared to other VCCT-based analyses. With the implementation of a crack speed function within the element, it can be easily expanded to the cases of varying crack velocities, without convergence difficulty for all cases. Neither singular element nor collapsed element was required. Therefore, due to its simplicity, the VCCT interface element is a potential tool for engineers to conduct dynamic fracture analysis in conjunction with commercial finite element analysis codes.

1. Introduction

Functionally graded materials (FGMs) are composites formed of two or more constituent phases with a continuously variable composition. They are attractive in potential applications owing to their numerous advantages, including the reduction of in-plane and transverse through-the-thickness stresses and stress intensity, and the improvement in residual stress distribution, thermal properties, and fracture toughness. There are a number of reviews dealing with various aspects of FGMs in recent years [1–3]. For instance, an embedded crack in an orthotropic FGM layer is considered in the case of mechanical loading [4]. Diverse areas relevant to the theory and applications of FGMs are reflected in [5], including homogenization of particulate FGM, heat transfer, stress, stability and dynamic analyses, manufacturing and design, applications, and fracture. Many aspects of FGMs such as free vibration [6], shear deformation [7], thermal buckling [8], and stress intensity factor [9] have been investigated. Moreover, the fracture toughness of

functionally graded (FG) sections is of interest especially for a material with elastic behavior [10, 11]. Using a plate bending finite element based on FOST, Singha et al. studied the nonlinear behaviors of FG plates under transverse load, considering the physical/exact neutral surface position and assuming the power law gradation of material properties in the thickness direction [12]. Isogeometric analysis was also very promising to be applied to a wide range of practical mechanics problems such as laminated composite and sandwich plates based on inverse trigonometric shear deformation theory, functionally graded plates based on generalized shear deformation theory [13]. Until now, FGM is one predominant mode of material and has been investigated extensively.

In recent years, there are growing concerns on how cracked functional material body responds to collision under impulse loading. To accurately evaluate the fracture mechanics under dynamic loading, researchers proposed dynamic fracture parameters, such as dynamic stress intensity factor (DSIF) and strain energy release rate (SERR). The dynamic

fracture parameter of simple geometric model, ideal material model, or special load model can be determined by the analytical method. However, this method is not applicable to complex structure or boundary conditions, and its experimental measurements are very expensive and time-consuming. Nevertheless, this type of problems can be well resolved by numerical calculations.

At present, the finite element method (FEM) is widely used for fracture analysis in FGMs. For instance, a pair of FEM-based elastodynamic contour integrals was developed to calculate the elastodynamic asymptotic mixed-mode stress field for plane elastic materials containing a stationary notch tip [16]. Graded finite elements can be used in fracture analysis in FGMs where the elastic moduli are smooth functions of spatial coordinates, which are integrated into the element stiffness matrix. The stress intensity factors for mode I and mixed-mode two-dimensional problems can be comparatively evaluated through three FGMs-tailored approaches: path-independent J-integral, modified crack closure integral, and displacement correlation [17]. The feasibility of FEM in cracked or uncracked FGM plates was studied. The J contour integral of ABAQUS was used to calculate stress intensity factors for an edge cracked FGM plate [18]. Matthews used the finite element analysis (FEA) for large displacement J-integral test to analyze mode I interlaminar fracture in composite materials [19]. The dynamic crack tip fields were determined, and the crack propagation of anisotropic materials was also characterized [20]. These previous works are important; however, they only focus on the dynamic cracks of isotropic and orthotropic materials, but not on the direction of crack propagation.

The methods used to resolve the fracture parameters include J-integral, M-integral, extrapolation, and virtual crack closure technique (VCCT). Among all fracture parameters, SERR is used increasingly in conjunction with linear elastic fracture mechanics (LEFM) and can be computed by VCCT together with FEA. VCCT requires a preexisting crack with a sharp neat tip within a material for crack initiation as well as conditions of small-scale yield to hold. With material nonlinearity at the crack tip (small process zone) ignored, LEFM-based approaches were proven effective in predicting crack initiation and subsequent growth [21, 22].

VCCT was proposed for 2D crack configurations [23] and extended to 3D-VCCT later [24]. Recently, the VCCT formulation for kinking cracks was proposed [25]. Krueger summarized historical developments and discussed different applications [26]. Combining 2D-VCCT and FEA, Sun and Qian compared the SERRs of interfacial cracks between two isotropic materials [27]. As reported, the SERRs for the delamination between the face sheet and the core material of sandwich structures were calculated [28, 29]. Glaessgen et al. calculated SERRs to evaluate the suppressing effect of stitching on debonding [30]. VCCT was also applied to electronic packaging [31–33]. Leski used VCCT to study the interface crack propagation [34]. Ramu used a differential transform method (DTM) to study free transverse vibration of isotropic rectangular plates resting on a Winkler foundation [35]. Modified crack closure integral technique was extended to the element-free Galerkin method [36].

A cohesive theory assumes the presence of a process zone in front of the crack tip whose fracture properties consist of upper and lower surfaces controlled by the cohesive traction-displacement discontinuity relationship and allows non-self-similar crack propagation [37]. An automated fracture procedure implemented in the large-scale, nonlinear, and explicit, finite element code DYNA3D can be used to simulate dynamic crack propagation in arbitrary directions [38]. Manolis et al. used boundary element method (BEM) to analyze the dynamic fracture of a smoothly inhomogeneous and defective plane [39]. Solving crack growth problems, the recent approach on smoothed finite element methods is really a good candidate [40, 41]. The DSIF around the antiplane crack in an infinite strip FGM under impact loading was investigated [42]. FG cracked plates under different loads and boundary conditions were numerically simulated using NURBS-based XIGA [43]. XIGA has been applied to stationary and propagating cracks in 2D [44], plastic collapse load analysis of cracked plane structures [45], and cracked plate/shell structures [46].

At present, the emerging computing method is strongly pertinent, nonversatile, and difficult to promote. Analysis of dynamic crack problems based on secondary development of ANSYS, ABAQUS, and so on is mainly focused on homogeneous materials, but it should be further expanded into FGMs.

In this study, based on the commercial FEA software ABAQUS and graded element method, we developed a dummy node fracture element, wrote the user subroutines UMAT and UEL, and solved the energy release rate component of cracked FGM plates.

2. FGMs

FGMs are often formed by two or more materials whose volume fractions change continuously along certain dimensions of the structure (Figure 1) [22]. The effective moduli of two constituents are homogenized by the rule of mixture or the Mori-Tanaka models which are used to evaluate the effective elastic properties of the grade composite. The effective property is expressed by a power law of volume fraction exponent as follows:

$$M(z) = M_m V_c + M_c V_m; \quad V_m = 1 - V_c \quad (1)$$

$$V_c = \left(0.5 + \frac{z}{h}\right)^n \quad \left(-\frac{h}{2} \leq z \leq \frac{h}{2}, 0 \leq n \leq \infty\right), \quad (2)$$

where subscripts m and c refer to the metal and ceramic components, respectively; z is the thickness coordinate and varies from $-h/2$ to $h/2$; n is the power law index; M_m and M_c denote the material properties of ceramic and metal, respectively, including Young's modulus, Poisson's ratio, and density. Equation (1) denotes the volume fraction variation versus nondimensional thickness (z/h) with different n .

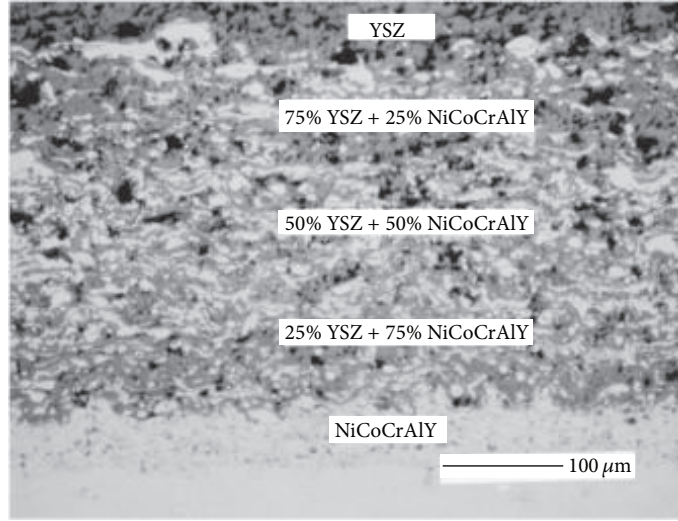
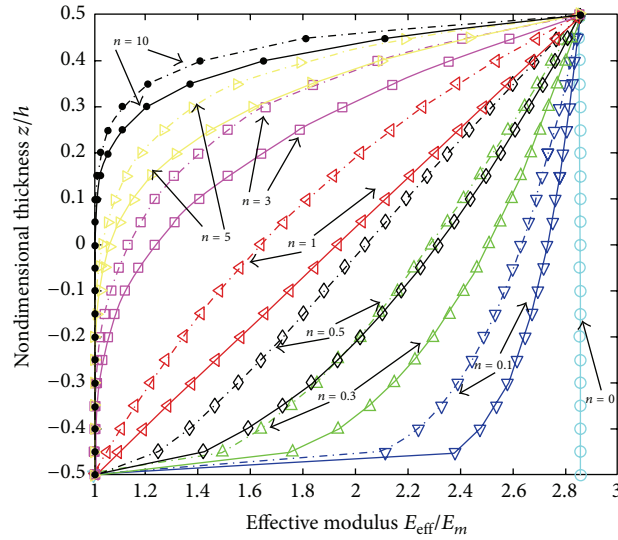


FIGURE 1: NiCoCrAlY functionally graded material [14].


 FIGURE 2: The effective modulus of Al/ZrO₂ FGM plate computed by the rule of mixture (in solid line) and the Mori-Tanaka model (in dash dot line) [15].

However, the rule of mixture does not reflect the interactions among the two materials [47, 48]. Meanwhile, the Mori-Tanaka model [49] is assumed to calculate their interactions through the effective bulk and shear modulus given by

$$\begin{aligned} \frac{K_e - K_m}{K_c - K_m} &= \frac{V_c}{1 + V_m ((K_c - K_m) / (K_m + 4/3\mu_m))}; \\ \frac{\mu_e - \mu_m}{\mu_c - \mu_m} &= \frac{V_c}{1 + V_m ((\mu_c - \mu_m) / (\mu_m + f_1))}, \\ f_1 &= \frac{\mu_m (9K_m + 8\mu_m)}{6(K_m + 2\mu_m)}. \end{aligned} \quad (3)$$

The effective Young modulus E_e and Poisson's ratio ν_e are, respectively, now written as

$$\begin{aligned} E_e &= \frac{9K_e\mu_e}{3K_e + \mu_e}, \\ \nu_e &= \frac{3K_e - 2\mu_e}{2(3K_e + \mu_e)}. \end{aligned} \quad (4)$$

Figure 2 illustrates comparison of the effective Young modulus of Al/ZrO₂ FGM plate calculated by the rule of mixture and the Mori-Tanaka scheme via the power index n . Note that with homogeneous material the two models produce the same values. For inhomogeneous material, the effective property through the thickness of the former is

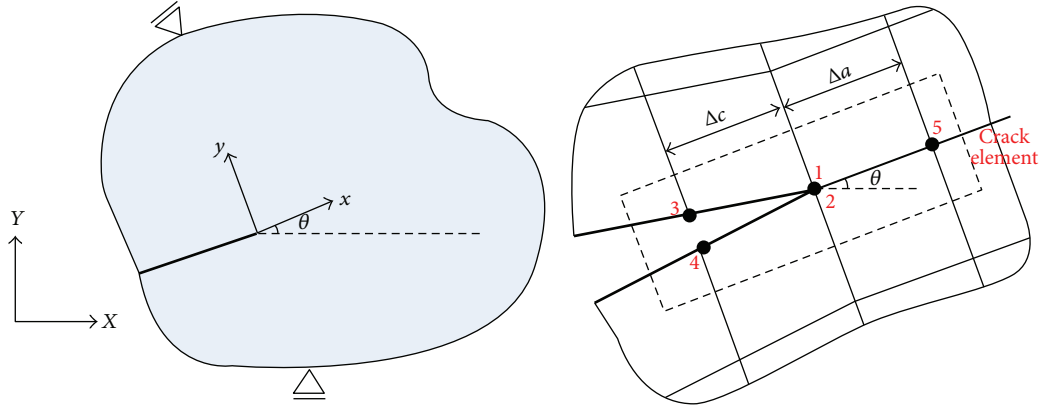


FIGURE 3: Fracture dummy node element.

higher than that of latter. Moreover, increasing in power index n leads to decrement of the material property due to the rise of metallic volume fraction. In this paper the power law distribution of constituent materials along the plate thickness is assumed, and the effective homogeneous properties are calculated by the rule of mixture [15].

Graded elements were implemented by directly sampling the properties at the Gauss points of each element [50, 51]. The graded finite element stiffness matrix relations can be written as follows [52]:

$$\mathbf{K}^e \mathbf{U}^e = \mathbf{F}^e, \quad (5)$$

where \mathbf{U}^e is a nodal displacement vector, \mathbf{F}^e is a load vector, and

$$\mathbf{K}^e = \int_{\Omega} (\mathbf{B}^e)^T \mathbf{D}^e(\mathbf{x}) \mathbf{B}^e d\Omega^e, \quad (6)$$

where \mathbf{B}^e is the strain-displacement matrix which contains the gradients of the interpolating functions; $\mathbf{D}^e(\mathbf{x})$ is a constitutive matrix variable; Ω^e is the domain of element e . In the present work, the elasticity matrix $\mathbf{D}^e(\mathbf{x}) = \mathbf{D}^e(x, y)$ was assumed to be a function of spatial coordinates.

The integral in (6) was evaluated by Gauss quadrature, and $\mathbf{D}^e(\mathbf{x})$ was specified at each Gaussian integration point. Thus the integral for two-dimensional problems becomes

$$\mathbf{K}^e = \sum_{i=1}^n \sum_{j=1}^n (\mathbf{B}^e)^T \mathbf{D}^e(\mathbf{x}) \mathbf{B}^e |J_{ij}| w_i w_j, \quad (7)$$

where the subscripts i and j refer to the Gaussian integration points, $|J_{ij}|$ is the determinant of the Jacobian matrix, and w_i is the Gaussian weight.

$\mathbf{D}^e(\mathbf{x})$ can be determined by interpolation, wherein the elastic modulus E and Poisson's ratio ν can be expressed as

$$E = \sum_{i=1}^m N_i E_i, \quad (8)$$

$$\nu = \sum_{i=1}^m N_i \nu_i,$$

where N_i is the shape function of FEM.

This part was written by UMAT in ABAQUS®. The file .inp should include the following statements:

```
*MATERIAL, NAME=FGM
```

```
*Depvar
```

```
1,
```

```
*User Material, constants=2
```

```
200000., 0.3
```

where 200000 and 0.3 are the initial values of E and ν , respectively.

3. VCCT Interface Element

Figure 3 shows the definition and node numbering of a typical VCCT interface element for 2D fracture problems. The details for the VCCT interfacial element can be found in [36–38]. Specifically, each element has five nodes. Such an element is placed in a way that nodes 1 and 2 are located at the crack tip, while nodes 3 and 4 are behind and node 5 is ahead of the crack tip. The element contains two sets of nodes: a top set (nodes 1, 3, and 5) and a bottom set (nodes 2 and 4). A very stiff spring is placed between nodes 1 and 2 to compute the crack tip nodal forces as follows:

$$F_x = K_x (u_1 - u_2), \quad (9)$$

$$F_y = K_y (v_1 - v_2),$$

where (u_1, v_1) and (u_2, v_2) are the displacement components of nodes 1 and 2, respectively, under the global coordinate system (X, Y) ; K_x and K_y are the X - and Y -direction spring stiffness, respectively. Initially, they are assigned with large numbers [37], but once the crack is predicted to grow, they are set to zero.

Dummy nodes 3, 4, and 5 do not contribute to the stiffness matrix and are introduced only to extract the information of displacement opening behind the crack tip and the crack

jump length ahead of the crack tip. For nodes 3 and 4 behind the crack tip, the displacement openings are

$$\begin{aligned}\Delta u &= u_3 - u_4, \\ \Delta v &= v_3 - v_4,\end{aligned}\quad (10)$$

where (u_3, v_3) and (u_4, v_4) are the displacement components of nodes 3 and 4, respectively, under the global coordinate system (X, Y) . Therefore, the crack jump length, which is the distance between nodes 1 and 5, is calculated as follows:

$$\Delta a = \sqrt{(x_5 - x_1)^2 + (y_5 - y_1)^2}, \quad (11)$$

where (x_1, y_1) and (x_5, y_5) are the global coordinates of nodes 1 and 5, respectively. If they are updated at each step, the crack orientation is also updated. This is of particular interest when large deformation cannot be neglected [45].

In order to separate the fracture modes (modes I and II), we computed the SERRs (G_I and G_{II}) with respect to the local coordinate system (x, y) attached to the crack tip as shown in Figure 1. The included angle between X and x is determined as follows:

$$\begin{aligned}\cos \theta &= \frac{x_5 - x_1}{\Delta a}, \\ \sin \theta &= \frac{y_5 - y_1}{\Delta a}.\end{aligned}\quad (12)$$

Then the nodal forces and the displacement openings in (9) and (10) are projected into the local coordinate system (x, y) as follows:

$$\begin{aligned}\bar{F}_x &= F_x \cos \theta + F_y \sin \theta, \\ \bar{F}_y &= -F_x \sin \theta + F_y \cos \theta, \\ \Delta \bar{u} &= \Delta u \cos \theta + \Delta v \sin \theta, \\ \Delta \bar{v} &= -\Delta u \sin \theta + \Delta v \cos \theta.\end{aligned}\quad (13)$$

Based on 2D-VCCT, the SERRs can be approximated as follows:

$$\begin{aligned}G_I &= \frac{\bar{F}_y \Delta \bar{v}}{2B\Delta a}, \\ G_{II} &= \frac{\bar{F}_x \Delta \bar{u}}{2B\Delta a},\end{aligned}\quad (14)$$

where B is the body thickness.

For the fixed crack problem under dynamic loading, the relationship between DSIF K_I^{dyn} (K_{II}^{dyn}) and SERR G_I^{dyn} (G_{II}^{dyn}) is expressed as follows:

$$\begin{aligned}K_I^{\text{dyn}}(t) &= \text{sign}(\bar{F}_y) \sqrt{\bar{E}G_I^{\text{dyn}}(t)}, \\ K_{II}^{\text{dyn}}(t) &= \text{sign}(\bar{F}_x) \sqrt{\bar{E}G_{II}^{\text{dyn}}(t)},\end{aligned}\quad (15)$$

where plane stress $\bar{E} = E^{\text{tip}}$; plane strain $\bar{E} = E^{\text{tip}}/(1 - (\nu^{\text{tip}})^2)$; E^{tip} and ν^{tip} are the modulus of elasticity and Poisson's ratio in the crack tip, respectively.

This part was written by UEL in ABAQUS. The .inp file should include the following statements:

```
*USER ELEMENT, NODES=5, TYPE=U600, PROP-
ERTIES=3, COORDINATES=2, VARIABLES=9
1,2
*ELEMENT, TYPE=U600, ELSET=CRACKTIP
60001, 13, 9013, 12, 9014, 14
*UEL PROPERTY, ELSET=CRACKTIP
200.0E6, 200.0E6, <B>
```

In the above statements, 60001 is the element number; 13, 9013, 12, 9014, and 14 are the node numbers, 200.0E6, 200.0E6, and are the x -direction spring stiffness, y -direction spring stiffness, and thickness of the plate, respectively.

For dynamic running cracks with constant velocity C , their DSIFs are related to the corresponding SERRs as follows:

$$K_I^{\text{dyn}}(C) = \sqrt{\frac{2\mu^{\text{tip}}}{A_I(C)} G_I^{\text{dyn}}(C)}, \quad (16)$$

$$K_{II}^{\text{dyn}}(C) = \sqrt{\frac{2\mu^{\text{tip}}}{A_{II}(C)} G_{II}^{\text{dyn}}(C)},$$

where μ is shear modulus. The crack speed functions are

$$\begin{aligned}A_I(C) &= \frac{\beta_1 (1 - \beta_2^2)}{D(C)}, \\ A_{II}(C) &= \frac{\beta_2 (1 - \beta_2^2)}{D(C)},\end{aligned}\quad (17)$$

where

$$\begin{aligned}\beta_1^2 &= 1 - \frac{C^2}{C_d^2}, \\ \beta_2^2 &= 1 - \frac{C^2}{C_s^2},\end{aligned}\quad (18)$$

$$D(C) = 4\beta_1\beta_2 - (1 + \beta_2^2)^2,$$

where

$$C_d = \sqrt{\frac{(\kappa^{\text{tip}} + 1)\mu^{\text{tip}}}{(\kappa^{\text{tip}} - 1)\rho^{\text{tip}}}}, \quad (19)$$

$$C_s = \sqrt{\frac{\mu^{\text{tip}}}{\rho^{\text{tip}}}},$$

where C_d is the dilatational speed; C_s is the shear wave speed; $\kappa^{\text{tip}} = 3 - 4\nu^{\text{tip}}$ for plane strain which is the case in examples 2 and 3; ρ^{tip} is material density at the crack tip.

The above procedure for the VCCT interface element regarding dynamic crack propagation was implemented into ABAQUS with its user subroutine UMAT and UEL. DSIFs are directly outputted through ABAQUS state variable "SDV" and thus can be determined simultaneously during FEA on ABAQUS without any postprocessing.

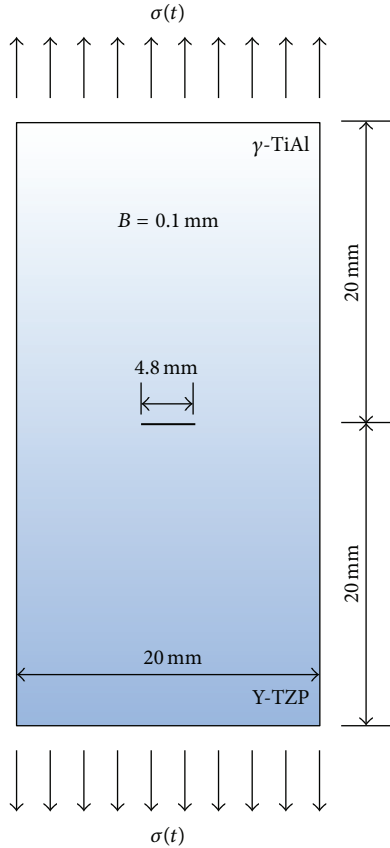


FIGURE 4: Center-crack functionally graded plate under impact loading.

This part was written by UEL in ABAQUS. The .inp file should include the following statements:

```
*USER ELEMENT, NODES=5, TYPE=U600, PROPERTIES=11, COORDINATES=2, VARIABLES=9
1,2
*ELEMENT, TYPE=U600, ELSET=CRACKTIP
60001, 13, 9013, 12, 9014, 14
*UEL PROPERTY, ELSET=CRACKTIP
74.588E12, 74.588E12, <B>, 0.0, <C>, 0.0, 2, 0.0, 32.0,
12.8, 44.8
```

In the above statements, 0.0, <C>, and 0.0, 2 are the amount of crack propagation, speed of crack propagation, initial crack length, and number of propagation steps; 0.0 and 32.0 are the x - and y -direction coordinates of the initial crack, respectively; 12.8 and 44.8 are the x - and y -direction coordinates of the final crack, respectively.

4. Numerical Results

4.1. Example 1. The rectangular panel with a central crack is the first example of a convergence study in this field. As shown in Figure 4, two FGMs Y-TZP and γ -TiAl were used. The components were subjected to (1)-(2), where the shape factor

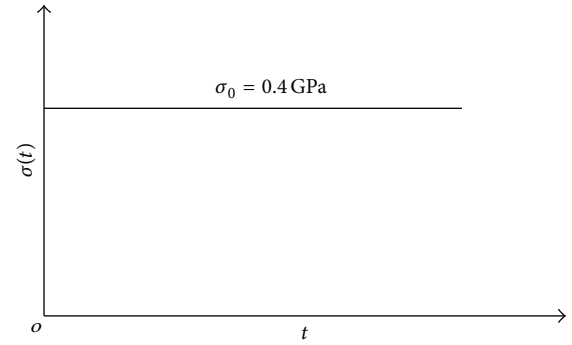


FIGURE 5: Heaviside step function type impulsive loading.

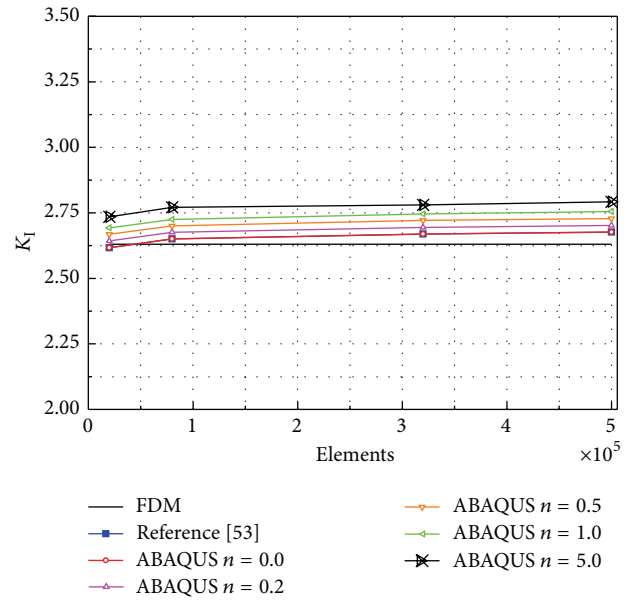


FIGURE 6: The convergence of the normalized DSIFs K_I at $t = 7 \mu\text{s}$.

$n = 0, 0.2, 0.5, 1.0,$ and 5.0 and the elastic moduli of Y-TZP and γ -TiAl are $M_m = 200 \text{ GPa}$ and $M_c = 186 \text{ GPa}$, respectively; Poisson's ratios ν of two materials are both 0.3 and the mass density $\rho = 5 \times 10^3 \text{ kg/m}^3$. The load form is plotted in Figure 5, the amplitude $\sigma_0 = 0.4 \text{ GPa}$, undamped.

In order to study the convergence of the present method, a discrete model of four grids (I: 100×200 elements, II: 200×400 elements, III: 400×800 elements, and IV: 500×1000 elements) is simulated to the normalized DSIFs K_I . The body geometry was modeled with two-dimensional ABAQUS standard plane strain elements such as "CPE4." Neither special singular elements nor the collapsed element technique was used at the crack tip.

The SERR solved by VCCT is converted to DSIFs, which are normalized by

$$K_I = \frac{K_I^{\text{dyn}}(t)}{\sigma_0 \sqrt{\pi a}}. \quad (20)$$

The dimensionless DSIFs K_I of FGM plate of four different grid models solved by our method at $t = 7 \mu\text{s}$ are plotted in Figure 6, when the shape factor $n = 0.0, 0.2, 0.5, 1.0,$ and

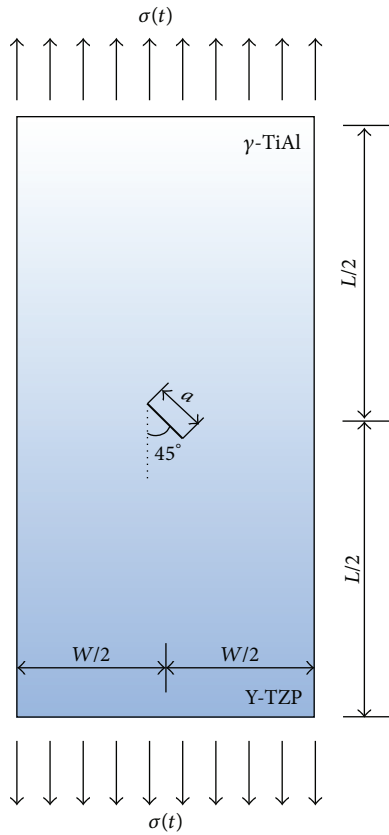


FIGURE 7: Inclined-crack functionally graded plate under impact loading.

5.0. At $n = 0$, material gradient does not change at all, and the FGM is only Y-TZP. Then the result was compared with FDM and [53]. Clearly, at $n = 0$, the result of our method is basically the same as in [53], and well consistent with the calculation of FDM. The result proves the accuracy of our method.

4.2. Example 2. The second example is a 60 mm long and 30 mm wide rectangular plate containing a 14.14 mm long central crack inclined at an angle $\alpha = 45^\circ$ (Figure 7). Two types of FGMs Y-TZP and γ -TiAl were used. The components were subjected to (1)-(2), where the shape factor $n = 0, 0.2, 0.5, 1.0, \text{ and } 5.0$, the elastic moduli of Y-TZP and γ -TiAl are $M_m = 200 \text{ GPa}$ and $M_c = 186 \text{ GPa}$, respectively; Poisson's ratios ν of two materials are both 0.3, and the mass density $\rho = 5 \times 10^3 \text{ kg/m}^3$. The load form is plotted in Figure 5, the amplitude $\sigma_0 = 0.4 \text{ GPa}$, undamped. The normalized DSIFs $K_I(t)$ and $K_{II}(t)$ of the right crack tip are plotted in Figures 8 and 9, respectively. The solutions obtained by the two methods are similar to those of Xie and Biggers Jr. [53] who used the VCCT and finite differencing method (FDM). Figure 10 shows the mesh before deformation and at several time points.

The dimensionless DSIFs K_I and K_{II} of FGM plate solved by our method are plotted in Figures 8 and 9, respectively,

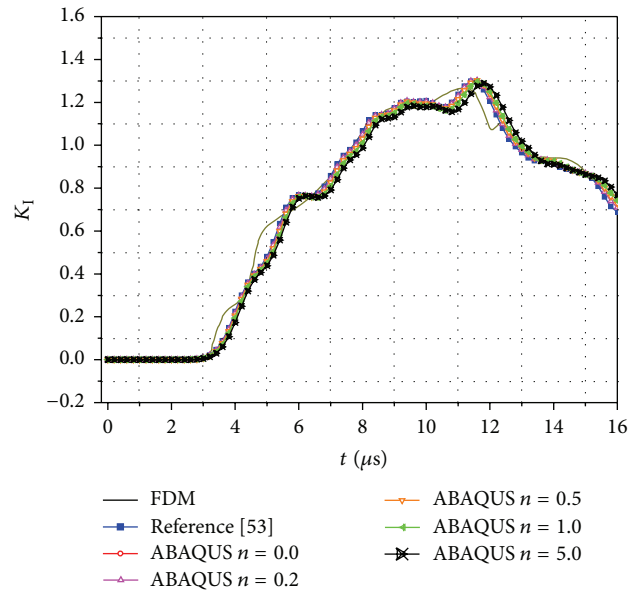


FIGURE 8: Dynamic stress intensity factor K_I of inclined-crack functionally graded plate with different shape factors.

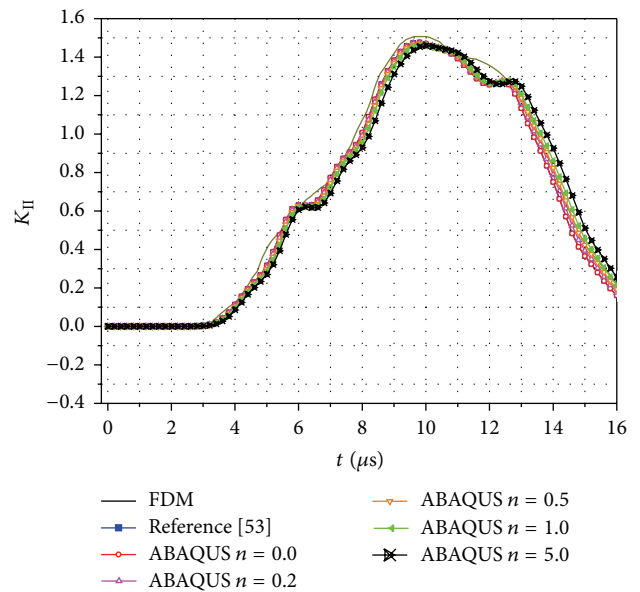


FIGURE 9: Dynamic stress intensity factor K_{II} of inclined-crack functionally graded plate with different shape factors.

when the shape factor $n = 0.0, 0.2, 0.5, 1.0, \text{ and } 5.0$. At $n = 0$, material gradient does not change at all, and the FGM is only Y-TZP. Then the result was compared with FDM and [53]. Clearly, at $n = 0$, the result of our method is basically the same as in [53], and well consistent with the calculation of FDM. The result further proves the accuracy of our method. Besides high precision and simplicity, the new method puts forward relevant information to calculate DSIF with the help of ABAQUS, and it endows the program with strong commonality and large extension space. The

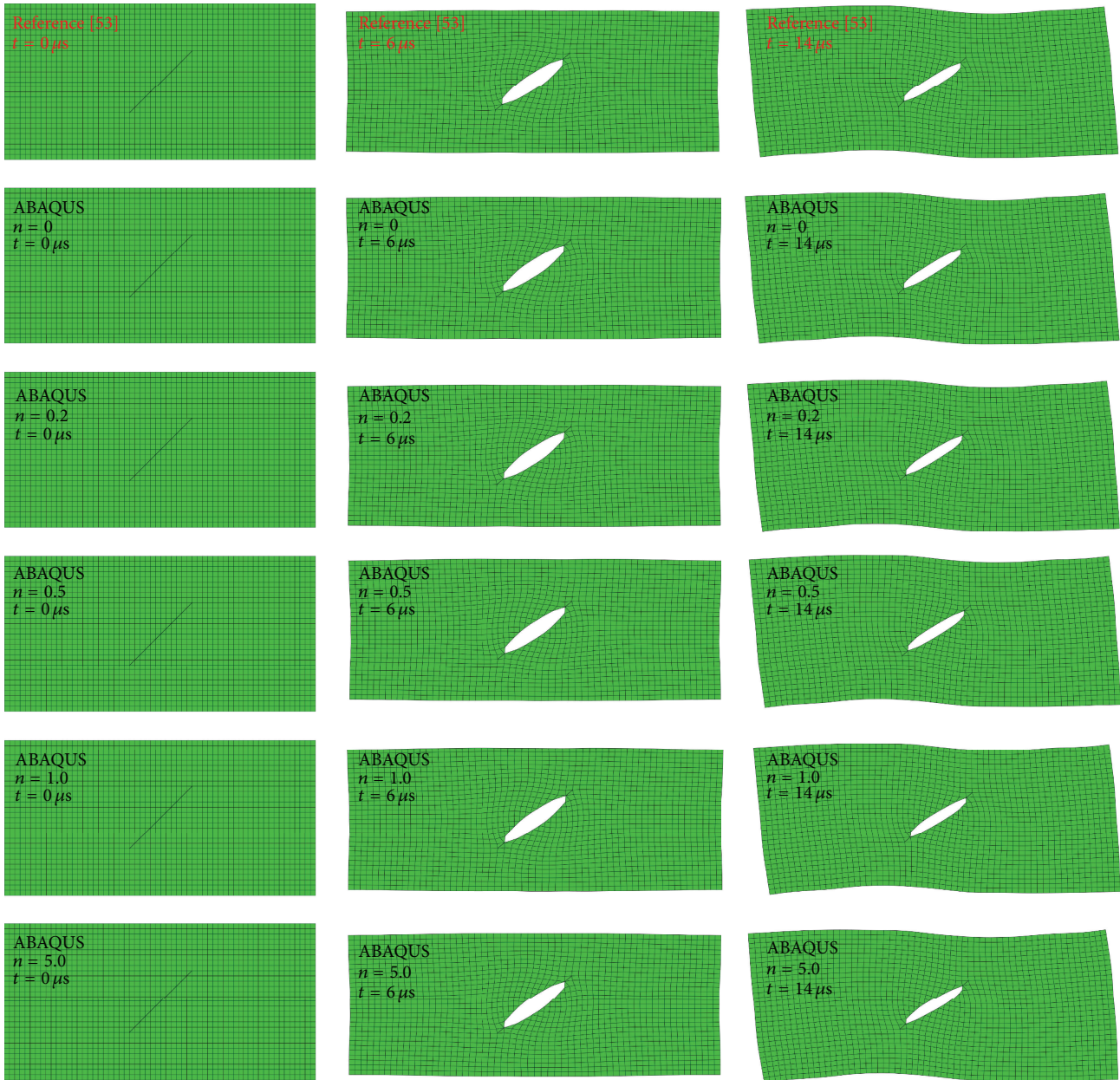


FIGURE 10: Different time steps of deformation figures of inclined-crack functionally graded plate.

deformation patterns of inclined-crack functionally graded plate in different methods and time steps are plotted in Figure 10. Visibly, the new method is correct and effective.

4.3. Example 3. The third example is a rectangular panel with a central crack as shown in Figure 11. Two FGMs Y-TZP and γ -TiAl were used. The components were subjected to (1)-(2), where the shape factor $n = 0, 0.2, 0.5, 1.0,$ and 5.0 and the elastic moduli of Y-TZP and γ -TiAl are $M_m = 200$ GPa and $M_c = 186$ GPa, respectively. The initial crack starts to propagate in a self-similar manner along the dashed line shown in Figure 11. The plate was subjected to a time-independent tensile stress at the edges. The constant crack

velocity was $C = 1000$ m/s. The normalized DSIF solution computed here is shown in Figure 12. The results developed here at $n = 0$ (Figure 12) are found to be nearly identical to the numerical solutions by Xie et al. [54]. The load form is plotted in Figure 5, at the amplitude $\sigma_0 = 0.1$ GPa, undamped. The normalized $K_I(t)$ is plotted in Figure 12 and compared with Xie et al. [54]. The solutions obtained by the two methods are similar. Figure 13 shows the mesh before deformation and at several time sets.

The body geometry was modeled with two-dimensional ABAQUS standard plane strain elements such as "CPE4." Neither special singular elements nor the collapsed element technique was used at the crack tip. The VCCT interface

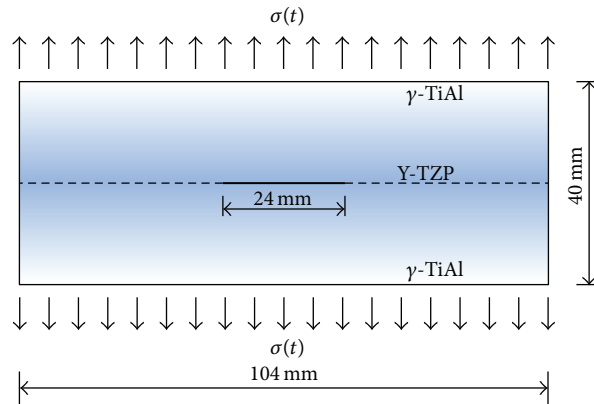


FIGURE 11: Central-crack functionally graded plate under impact loading.

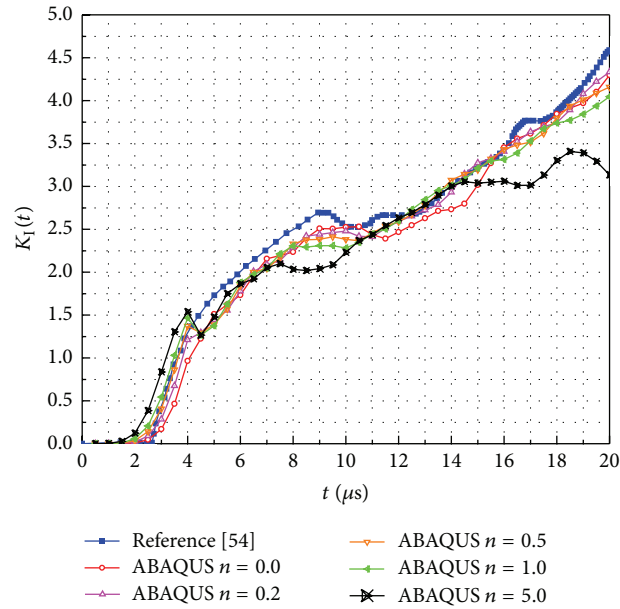


FIGURE 12: Dynamic stress intensity factor K_I of central-crack functionally graded plate with different shape factors.

elements were placed along the crack path (dashed line in Figure 11) and used as easy as the ABAQUS standard elements. An implicit dynamic analysis procedure was employed, without encountering convergence difficulty. No damping was included in the model. Variations of normalized DSIFs during the crack propagations at $C = 1000$ m/s are shown in Figure 12. Clearly, the normalized K_I remains almost constant throughout the crack propagation, while the normalized K_I gradually decreases. Moreover, the DSIFs drop immediately after the crack propagation begins. Figure 13 shows the deformation during the dynamic crack propagation.

4.4. Example 4. An FGM plate with a slanted edge crack shown in Figure 14 was used as an example of mixed-mode dynamic crack propagation to illustrate the new method

of VCCT interface element. The initial crack ($a_0 \cos \theta_0 = 0.4W$, $W = 32$ mm) starts to propagate in a self-similar manner along the dashed line shown in Figure 14. The plate was subjected to a time-independent tensile stress at the edges. The crack velocity was constant at $C = 0.2 C_s$. The components were subjected to (1)-(2), where the shape factor $n = 0, 0.2, 0.5, 1.0$, and 5.0 and the elastic moduli of Y-TZP and γ -TiAl are $M_m = 200$ GPa and $M_c = 186$ GPa, respectively; Poisson's ratios ν of two materials are both 0.3 , and the mass density is $\rho = 5 \times 10^3$ kg/m³. The body geometry was modeled with 2D ABAQUS standard plane strain elements such as "CPE4" and "CPE3." Neither special singular elements nor the collapsed element technique was used at the crack tip. The VCCT interface elements were placed along the crack path (dashed line in Figure 14) and used as easily as the ABAQUS standard elements. An implicit dynamic analysis procedure



FIGURE 13: Deformed body for dynamic crack propagation at different crack length ($C = 1000$ m/s).

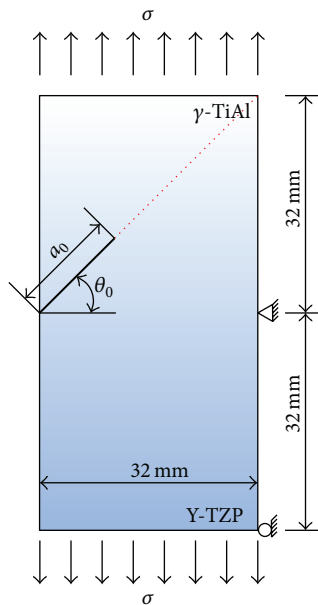


FIGURE 14: Geometry and boundary conditions for dynamic crack propagation under time-independent loading.

was employed, without encountering convergence difficulty. No damping was included in the model.

Variations of normalized DSIFs during the crack propagation at $C = 0.2 C_s$ are shown in Figures 15 and 16. Clearly,

the normalized K_{II} remains almost constant throughout the crack propagation, while the normalized K_I gradually decreases. Moreover, the DSIFs drop immediately upon the crack propagation. Figure 17 shows the deformation during

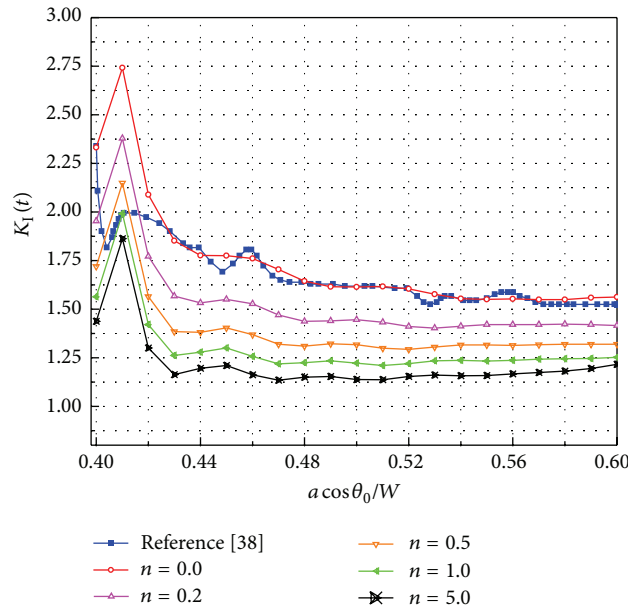


FIGURE 15: Normalized stress intensity factors $K_I(t)$ for propagating crack ($C = 0.2 Cs$).

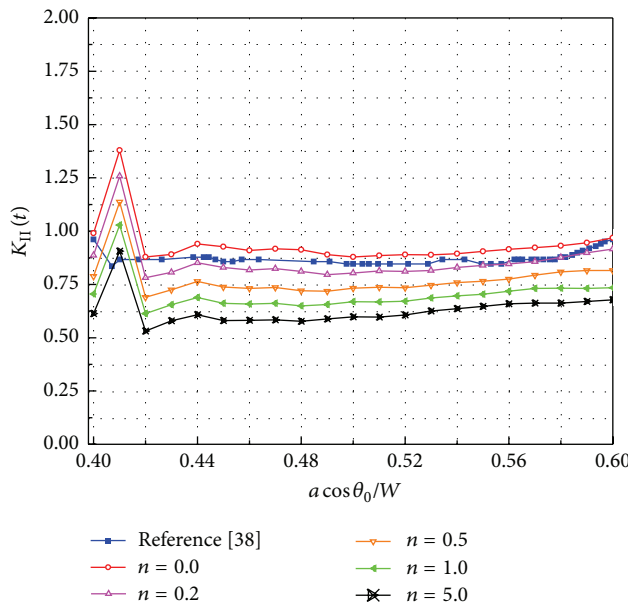


FIGURE 16: Normalized stress intensity factors $K_{II}(t)$ for propagating crack ($C = 0.2 Cs$).

the dynamic crack propagation. The results obtained by the new method agree well with those by Qian and Xie [38] using moving singular elements.

5. Conclusions

A 2D-VCCT interface element based on graded finite element method was presented for dynamic fracture analysis. The element was implemented into commercial FEA software ABAQUS via the user element subroutine UMAT and UEL. This new method was evaluated with three examples. The results agree well with the available numerical and

experimental results in previous studies. With this interface element, fracture mechanics can be directly applied to crack growth problem on commercial FEA software. The element has several significant advantages, such as no need of extra postprocessing to extract fracture parameters, and no special burden on definition of body mesh. It can be applied in conjunction with conventional finite elements. Finally, the interface element proven reliable in a variety of cases can be employed potentially in other cases of dynamic fracture. In summary, the new 2D-VCCT interface element is simple, efficient, universal, and robust. This element method is a potential tool for structure-level analysis of dynamic crack

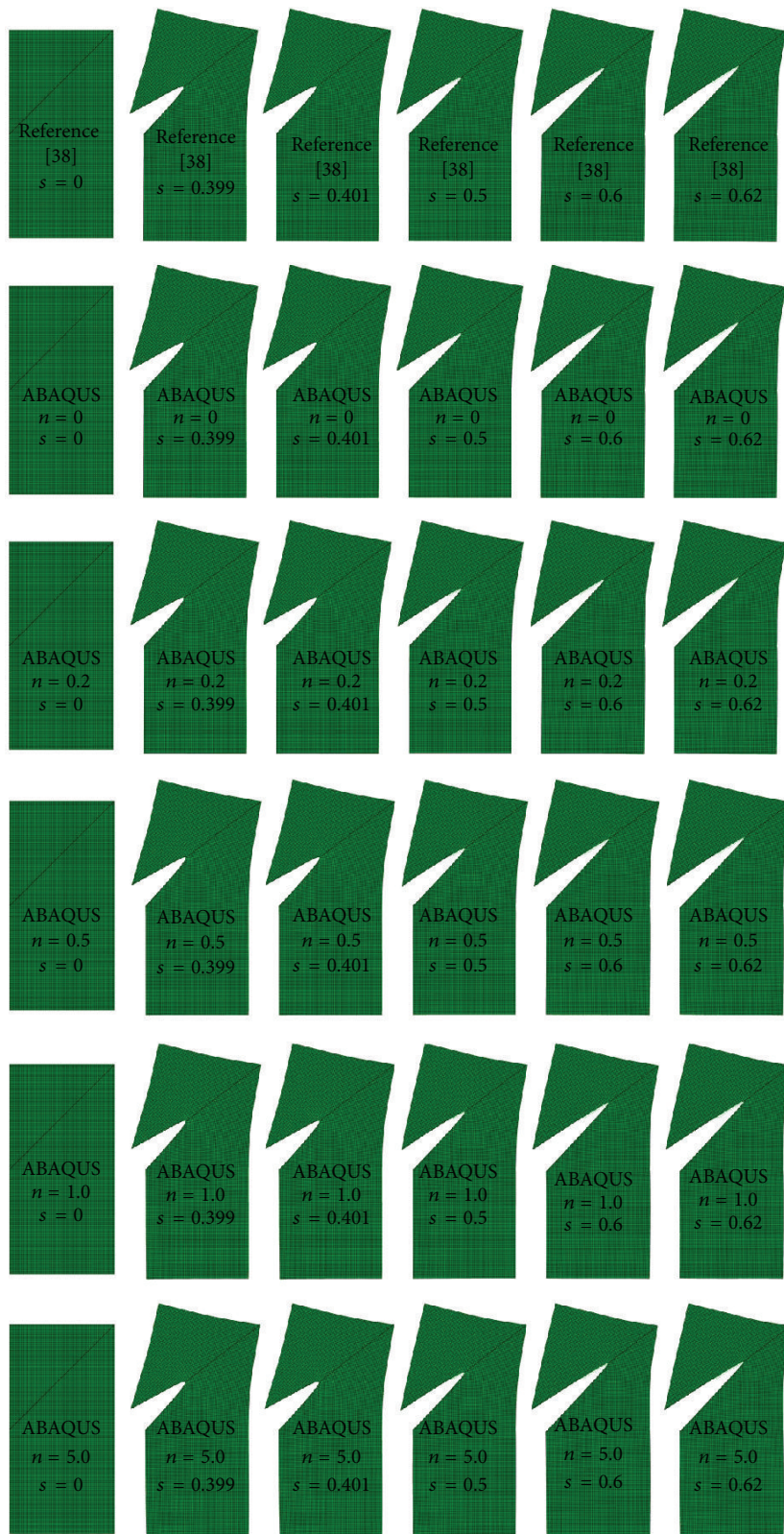


FIGURE 17: Deformed body for dynamic crack propagation at different crack length ($C = 0.2 C_s$).

propagation problems by resorting to the commercial FEA codes with user subroutines.

Competing Interests

The authors declare that there are no competing interests regarding the publication of this paper.

Acknowledgments

This work was financially supported by the National Natural Science Foundation of China (Grant no. 51305157), the National Key Scientific Instrument and Equipment Development Projects, China (Grant no. 2012YQ030075), and Jilin Provincial Department of Science and Technology Fund Project (Grant nos. 20160520064JH, 20130305006GX).

References

- [1] A. Ahmed and L. J. Sluys, "A computational model for the simulation of dynamic fracture in laminated composite plates," *Journal of Composite Materials*, vol. 49, no. 14, pp. 1717–1738, 2015.
- [2] H. Li, "Effective boundary conditions of the heat equation on a body coated by functionally graded material," *Discrete and Continuous Dynamical Systems, Series A*, vol. 36, no. 3, pp. 1415–1430, 2016.
- [3] S. Krahulec, J. Sladek, V. Sladek, and Y.-C. Hon, "Meshless analyses for time-fractional heat diffusion in functionally graded materials," *Engineering Analysis with Boundary Elements*, vol. 62, pp. 57–64, 2016.
- [4] S. Dag, B. Yildirim, and D. Sarikaya, "Mixed-mode fracture analysis of orthotropic functionally graded materials under mechanical and thermal loads," *International Journal of Solids and Structures*, vol. 44, no. 24, pp. 7816–7840, 2007.
- [5] V. Birman and L. W. Byrd, "Modeling and analysis of functionally graded materials and structures," *Applied Mechanics Reviews*, vol. 60, no. 1-6, pp. 195–216, 2007.
- [6] Y. Liu and D. W. Shu, "Free vibration analysis of exponential functionally graded beams with a single delamination," *Composites Part B: Engineering*, vol. 59, pp. 166–172, 2014.
- [7] Z. Belabed, M. S. A. Houari, A. Tounsi, S. R. Mahmoud, and O. Anwar Bég, "An efficient and simple higher order shear and normal deformation theory for functionally graded material (FGM) plates," *Composites Part B: Engineering*, vol. 60, pp. 274–283, 2014.
- [8] K.-S. Na and J.-H. Kim, "Three-dimensional thermal buckling analysis of functionally graded materials," *Composites Part B: Engineering*, vol. 35, no. 5, pp. 429–437, 2004.
- [9] W. Zhao, Z. Hu, X. Zhang, H. Xie, and L. Yu, "The dynamic stress intensity factor around the anti-plane crack in an infinite strip functionally graded material under impact loading," *Theoretical and Applied Fracture Mechanics*, vol. 74, no. 1, pp. 1–6, 2014.
- [10] U. H. Bankar and V. Parameswaran, "Fracture of edge cracked layered plates subjected to in-plane bending," *Experimental Mechanics*, vol. 53, no. 2, pp. 287–298, 2013.
- [11] I. V. Ivanov, T. Sadowski, and D. Pietras, "Crack propagation in functionally graded strip under thermal shock," *The European Physical Journal: Special Topics*, vol. 222, no. 7, pp. 1587–1595, 2013.
- [12] M. K. Singha, T. Prakash, and M. Ganapathi, "Finite element analysis of functionally graded plates under transverse load," *Finite Elements in Analysis and Design*, vol. 47, no. 4, pp. 453–460, 2011.
- [13] C. H. Thai, S. Kulasegaram, L. V. Tran, and H. Nguyen-Xuan, "Generalized shear deformation theory for functionally graded isotropic and sandwich plates based on isogeometric approach," *Computers and Structures*, vol. 141, pp. 94–112, 2014.
- [14] K. A. Khor and Y. W. Gu, "Effects of residual stress on the performance of plasma sprayed functionally graded $ZrO_2/NiCoCrAlY$ coatings," *Materials Science and Engineering: A*, vol. 277, no. 1-2, pp. 64–76, 2000.
- [15] C. H. Thai, V. N. V. Do, and H. Nguyen-Xuan, "An improved Moving Kriging-based meshfree method for static, dynamic and buckling analyses of functionally graded isotropic and sandwich plates," *Engineering Analysis with Boundary Elements*, vol. 64, pp. 122–136, 2016.
- [16] J. H. Chang and D. J. Wu, "Finite element calculation of elastodynamic stress field around a notch tip via contour integrals," *International Journal of Solids and Structures*, vol. 40, no. 5, pp. 1189–1202, 2003.
- [17] J.-H. Kim and G. H. Paulino, "Finite element evaluation of mixed mode stress intensity factors in functionally graded materials," *International Journal for Numerical Methods in Engineering*, vol. 53, no. 8, pp. 1903–1935, 2002.
- [18] G. Anlas, M. H. Santare, and J. Lambros, "Numerical calculation of stress intensity factors in functionally graded materials," *International Journal of Fracture*, vol. 104, no. 2, pp. 131–143, 2000.
- [19] T. Matthews, M. Ali, and A. J. Paris, "Finite element analysis for large displacement J-integral test method for Mode I interlaminar fracture in composite materials," *Finite Elements in Analysis and Design*, vol. 83, pp. 43–48, 2014.
- [20] M. Saribay and H. F. Nied, "Dynamic stress intensity factors for suddenly loaded structures using enriched finite elements," *Theoretical and Applied Fracture Mechanics*, vol. 70, pp. 59–67, 2014.
- [21] E. Galenne, S. Andrieux, and L. Ratier, "A modal approach to linear fracture mechanics for dynamic loading at low frequency," *Journal of Sound and Vibration*, vol. 299, no. 1-2, pp. 283–297, 2007.
- [22] S. S. Vel and R. C. Batra, "Exact solution for thermoelastic deformations of functionally graded thick rectangular plates," *AIAA Journal*, vol. 40, no. 7, pp. 1421–1433, 2002.
- [23] E. F. Rybicki and M. F. Kanninen, "A finite element calculation of stress intensity factors by a modified crack closure integral," *Engineering Fracture Mechanics*, vol. 9, no. 4, pp. 931–938, 1977.
- [24] K. N. Shivakumar, P. W. Tan, and J. C. Newman Jr., "A virtual crack-closure technique for calculating stress intensity factors for cracked three dimensional bodies," *International Journal of Fracture*, vol. 36, no. 3, pp. R43–R50, 1988.
- [25] D. Xie, A. M. Waas, K. W. Shahwan, J. A. Schroeder, and R. G. Boeman, "Computation of energy release rates for kinking cracks based on virtual crack closure technique," *Computer Modeling in Engineering & Sciences*, vol. 6, no. 6, pp. 515–524, 2004.
- [26] R. Krueger, "Virtual crack closure technique: history, approach, and applications," *Applied Mechanics Reviews*, vol. 57, no. 1–6, pp. 109–143, 2004.
- [27] C. T. Sun and W. Qian, "The use of finite extension strain energy release rates in fracture of interfacial cracks," *International*

- Journal of Solids and Structures*, vol. 34, no. 20, pp. 2595–2609, 1997.
- [28] W. J. Cantwell, R. Scudamore, J. Ratcliffe, and P. Davies, “Interfacial fracture in sandwich laminates,” *Composites Science and Technology*, vol. 59, no. 14, pp. 2079–2085, 1999.
- [29] S. Goswami and W. Becker, “The effect of facesheet/core delamination in sandwich structures under transverse loading,” *Composite Structures*, vol. 54, no. 4, pp. 515–521, 2001.
- [30] E. H. Glaessgen, I. S. Raju, and C. C. Poe Jr., “An efficient analysis for the debonding of stitched skin-stiffened structures,” *Journal of Composites Technology and Research*, vol. 25, no. 1, pp. 69–81, 2003.
- [31] X. Dai, M. V. Brillhart, and P. S. Ho, “Adhesion measurement for electronic packaging applications using double cantilever beam method,” *IEEE Transactions on Components and Packaging Technologies*, vol. 23, no. 1, pp. 101–116, 2000.
- [32] R. J. Harries and S. K. Sitaraman, “Numerical modeling of interfacial delamination propagation in a novel peripheral array package,” *IEEE Transactions on Components and Packaging Technologies*, vol. 24, no. 2, pp. 256–263, 2001.
- [33] S. A. Fawaz, “Application of the virtual crack closure technique to calculate stress intensity factors for through cracks with an elliptical crack front,” *Engineering Fracture Mechanics*, vol. 59, no. 3, pp. 327–342, 1998.
- [34] A. Leski, “Implementation of the virtual crack closure technique in engineering FE calculations,” *Finite Elements in Analysis and Design*, vol. 43, no. 3, pp. 261–268, 2007.
- [35] I. Ramu and S. Mohanty, “Modal analysis of functionally graded material plates using finite element method,” *Procedia Materials Science*, vol. 6, pp. 460–467, 2014.
- [36] N. Muthu, B. G. Falzon, S. K. Maiti, and S. Khoddam, “Modified crack closure integral technique for extraction of SIFs in meshfree methods,” *Finite Elements in Analysis and Design*, vol. 78, pp. 25–39, 2014.
- [37] D. Xie and S. B. Biggers Jr., “Progressive crack growth analysis using interface element based on the virtual crack closure technique,” *Finite Elements in Analysis and Design*, vol. 42, no. 11, pp. 977–984, 2006.
- [38] Q. Qian and D. Xie, “Analysis of mixed-mode dynamic crack propagation by interface element based on virtual crack closure technique,” *Engineering Fracture Mechanics*, vol. 74, no. 5, pp. 807–814, 2007.
- [39] G. D. Manolis, P. S. Dineva, and T. V. Rangelov, “Dynamic fracture analysis of a smoothly inhomogeneous plane containing defects by BEM,” *Engineering Analysis with Boundary Elements*, vol. 36, no. 5, pp. 727–737, 2012.
- [40] N. Vu-Bac, H. Nguyen-Xuan, L. Chen et al., “A noded-based smoothed XFEM for fracture mechanics,” *Computer Modeling in Engineering and Sciences*, vol. 73, no. 4, pp. 331–356, 2011.
- [41] H. Nguyen-Xuan, G. R. Liu, S. Bordas, S. Natarajan, and T. Rabczuk, “An adaptive singular ES-FEM for mechanics problems with singular field of arbitrary order,” *Computer Methods in Applied Mechanics and Engineering*, vol. 253, pp. 252–273, 2013.
- [42] J. Chen, Z. X. Liu, and Z. Z. Zou, “Electromechanical impact of a crack in a functionally graded piezoelectric medium,” *Theoretical and Applied Fracture Mechanics*, vol. 39, no. 1, pp. 47–60, 2003.
- [43] G. Bhardwaj, I. V. Singh, B. K. Mishra, and T. Q. Bui, “Numerical simulation of functionally graded cracked plates using NURBS based XIGA under different loads and boundary conditions,” *Composite Structures*, vol. 126, pp. 347–359, 2015.
- [44] S. S. Ghorashi, N. Valizadeh, and S. Mohammadi, “Extended isogeometric analysis for simulation of stationary and propagating cracks,” *International Journal for Numerical Methods in Engineering*, vol. 89, no. 9, pp. 1069–1101, 2012.
- [45] H. Nguyen-Xuan, L. V. Tran, C. H. Thai, and C. V. Le, “Plastic collapse analysis of cracked structures using extended isogeometric elements and second-order cone programming,” *Theoretical and Applied Fracture Mechanics*, vol. 72, no. 1, pp. 13–27, 2014.
- [46] N. Nguyen-Thanh, N. Valizadeh, M. N. Nguyen et al., “An extended isogeometric thin shell analysis based on Kirchhoff-Love theory,” *Computer Methods in Applied Mechanics and Engineering*, vol. 284, pp. 265–291, 2015.
- [47] S. S. Vel and R. C. Batra, “Three-dimensional exact solution for the vibration of functionally graded rectangular plates,” *Journal of Sound and Vibration*, vol. 272, no. 3–5, pp. 703–730, 2004.
- [48] L. F. Qian, R. C. Batra, and L. M. Chen, “Static and dynamic deformations of thick functionally graded elastic plates by using higher-order shear and normal deformable plate theory and meshless local Petrov-Galerkin method,” *Composites Part B: Engineering*, vol. 35, no. 6–8, pp. 685–697, 2004.
- [49] T. Mori and K. Tanaka, “Average stress in matrix and average elastic energy of materials with misfitting inclusions,” *Acta Metallurgica*, vol. 21, no. 5, pp. 571–574, 1973.
- [50] M. H. Santare and J. Lambros, “Use of graded finite elements to model the behavior of nonhomogeneous materials,” *Journal of Applied Mechanics*, vol. 67, no. 4, pp. 819–822, 2000.
- [51] J. E. Dolbow and M. Gosz, “On the computation of mixed-mode stress intensity factors in functionally graded materials,” *International Journal of Solids and Structures*, vol. 39, no. 9, pp. 2557–2574, 2002.
- [52] T. J. Hughes, *The Finite Element Method: Linear Static and Dynamic Finite Element Analysis*, Courier Corporation, 2012.
- [53] D. Xie and S. B. Biggers Jr., “Calculation of transient strain energy release rates under impact loading based on the virtual crack closure technique,” *International Journal of Impact Engineering*, vol. 34, no. 6, pp. 1047–1060, 2007.
- [54] D. Xie, L. Qian, and C. A. Li, *Numerical Calculation Method of Fracture Mechanics and the Engineering Application*, Science Press, Beijing, China, 2009.